THE UNIVERSITY OF MANITOBA

TEMPERATURE DEPENDENCE OF THE COLLISIONAL INTERFERENCE IN THE PURE ROTATIONAL BAND OF HD

BY

ZHENGFANG LU

A Thesis Submitted to
The Faculty of Graduate Studies of
the University of Manitoba
in Partial Fulfillment of the Requirements of
the Degree of

DOCTOR OF PHILOSOPHY

DEPARTMENT OF PHYSICS
WINNIPEG, MANITOBA

ISBN 0-315-77946-2

TEMPERATURE DEPENDENCE OF THE COLLISIONAL INTERFERENCE IN THE PURE ROTATIONAL BAND OF HD

BY

ZHENGFANG LU

A thesis submitted to the Faculty of Graduate Studies of the University of Manitoba in partial fulfillment of the requirements of the degree of

DOCTOR OF PHILSOPHY

TO

MY PARENTS

Abstract

The temperature dependence of the collisional interference in the pure rotational band of gaseous HD and its mixtures was experimentally investigated at 77 K, 195 K and 296 K. Values of the allowed dipole moment matrix elements, the absolute frequencies, the spectral line shape parameters (broadening and frequency shift coefficients), and the interference parameters, for the first four rotational lines, were deduced from the spectra. Theoretical calculations of the interference parameter a, and the line width were performed based, respectively, on the intracollisional theory developed by Herman, Tipping and Poll[1] and a semiclassical theory developed by Robert and Bonamy[2]. The induced dipole moments for $HD - Ne$ and $HD - N_2$ were estimated, with reference to the intracollisional theory. A comprehensive discussion of experimental results with theoretical calculations is given. Better agreement between experimental results and the predictions by the above theories are found for R(2) and R(3) and for HD perturbed by large molecules. The behaviour of temperature dependence of collisional interference in the pure rotational band for HD and its mixtures is found to be more complicated than the prediction of the intracollisional theory. In particular a change in sign of the interference parameter a, is not explainable by the above theory.

[1]R. M. Herman, R. H. Tipping and J. D. Poll, Phys. Rev., A**20**, 2006 (1979).
[2]D. Robert and J. Bonamy, J. Phys., **40**, 923 (1979).

Acknowledgements

I am indebted to my supervisor Prof. G. C. Tabisz for his encouragement and skillful guidance throughout the whole period of this study. I appreciate the friendship between us, and appreciate everything he did on my behalf.

I want to thank Dr. L. Ulivi for sharing his knowledge in the 1987 experiment, and Dr. J. Bonamy for her generous help in linewidth calculations.

I wish to extend my thanks to Dr. H. Kunkel, Mr. G. Roy, Ms. S. Bergen, and many others who kindly offered their help when I needed it. It has impressed me that Winnipeg is cold in its climate but warm in its people.

At this moment I feel grateful to my wife Xiaoyu and my daughter Hua for their love, understanding and support in every aspect.

The Graduate Fellowship from the University of Manitoba is specially acknowledged.

Contents

List of Figures

List of Tables

Chapter 1

INTRODUCTION

During the past 20 years, considerable effort has been put forth to study the pressure-broadened infrared absorption spectrum of HD. There are several reasons for the fundamental importance of this study. First, the hydrogen molecular isotope HD has a very small dipole moment on the order of 10^{-3} D (Debye=10^{-18} esu =0.39343 ea_0 =3.33564 $\times$ 10^{-30} Cm) [1]. This dipole moment is about 10^{-4} smaller than the usual dipole moment of a polar molecule and is about 10^{-1} of the average magnitude of the typical collision-induced dipole moment [2]. The small magnitude of the dipole moment makes HD an almost unique case for the study of *intracollisional interference*. This phenomenon arises from constructive or destructive interference between the optical transitions involving the allowed and collision-induced dipole moment during a collision [1]. Second, the role of collision-induced transitions are intrinsically interesting to spectral line broadening studies, which can, in principle, give valuable information regarding the anisotropic molecular forces and various intermolecular interactions [3][4][5]. Third, because of the simplicity of the molecule, it is amenable to theoretical treatment. The theoretical

interpretations and generalizations could lead to a better understanding of more complicated molecular systems [6]. And fourth, it has important applications in astronomy [7][8]. The abundance of deuterium and the ratio D/H are very important astrophysical parameters with respect to to the evolution of the primitive solar nebula and the formation of the planets [9][10][11]. However, its estimation from the D_2 spectrum is extremely difficult because the abundance of D_2 in the solar system is only about 10^{-5} that of H_2 and D_2 does not have an allowed dipole moment. The D/H ratio could be obtained from the measurements of the HD spectra of an astronomical source if the corresponding laboratory and theoretical data on the frequencies and intensities are known [12][13][14]. Consequently, much interest in the infrared spectrum of HD has been motivated by the need to measure the absolute frequencies and the allowed dipole moment element of its spectral lines.

1.1 Historical Scope

The possibility of the existence of pure rotational and vibrational- rotational transitions in the HD molecule was first discussed by G. C. Wick in 1935. He recognized that the HD molecule should have a weak allowed dipole moment and made the first theoretical estimate of its strength, 10^{-4} D for the fundamental band [15]. G. Herzberg first observed a number of lines in the $2-0$ and $3-0$ bands, and subsequently in the $3-0$ and $4-0$ bands, of the HD spectrum in 1949 and 1950 [11][16], thereby verifying Wick's prediction.

In 1952 T. Y. Wu published a paper in which he extended the perturbation

theory treatment of Wick to the overtones and estimated the ratio of the $4-0$ to the $3-0$ band intensities to be approximately 0.27 which proved to be consistent with the more refined data obtained by Durie and Herzberg in 1960 [17][18]. At about the time of Herzberg's refined experiments, S. M. Blinder made the first quantitative calculation of the pure rotational matrix element of the dipole moment of HD using perturbation theory [19], obtaining a value of 8.89×10^{-4} D. This calculation was improved by Blinder himself one year later by applying a variational method. Finally he arrived at an estimated value of 5.67×10^{-4} D for the pure rotational matrix element of the allowed dipole moment of HD, about 70% of the currently accepted value [20].

It is rather interesting to look back at this research field in 1960s. Five years after Blinder's calculation, Kolos and Wolniewiez [21] calculated the rotational matrix element of the allowed dipole moment of HD using a variational calculation and obtained an estimated value of 1.54×10^{-3} D, about three times as large as Blinder's value. Two years later, the pure rotational spectra of HD in the density range of 50-100 amagat was first experimentally investigated by M. Trefler and H. P. Gush [22]. Not only did they find the J dependence of the rotational dipole moment in the pure rotational band of HD (the magnitude of the dipole moment increasing with increasing J), but they also found, surprisingly, that the average value of the rotational matrix element of the allowed dipole moment over R(0) to R(3) was $(5.85 \pm 0.17) \times 10^{-4}$ D, in excellent agreement with Blinder's calculation. At about the same time, Karl investigated the question of the *J-dependence* from the theoretical point of view by extending Blinder's calculation and reached

two conclusions: the *J-dependence* was very small and the *J-dependence* had the opposite sign to the experimental results [23]. Thus, although the experimental result of Trefler and Gush agreed well with Blinder's calculation, it qualitatively disagreed with the calculation concerning the *J-dependence* of the transition moments.

This dramatic agreement and disagreement, however, stimulated new interest in the investigation of the HD spectra and resulted in the fruitful period of the 1970s to 1980s.

From 1972 to 1974, A. R. W. McKellar investigated the spectrum of gaseous HD at a temperature of 77 K with the densities from 1 to 60 amagat, and first reported the quantitative intensities for several lines in the fundamental and overtone bands [24][25][26][27]. Furthermore, he found an unexpected feature in the spectra; the spectral lines were symmetric at low densities while broad and quite pronounced asymmetry developed at high densities. The dipole moment elements for the fundamental and overtone bands reported by McKellar agreed well with another measurement by Bejar and Gush [28] as well as with the calculation by Poll and Karl [29]. During the period of 1975 to 1977, R. D. G. Prasad and S. P. Reddy observed the collision-induced infrared absorption in the fundamental band of pure HD and HD with inert gas mixtures [30][31][32]. They found the enhancement of the integrated intensity due to interference not only in the pure HD spectrum, but also in the spectra of HD with inert gases. After 1975, the investigation of the higher overtone bands of HD, such as the $5-0$ and $6-0$ bands, became possible. Those bands were observed by McKellar and Oka in

1976 [33], then by F. W. Dalby and J. Vigue in 1979 [34], and by W. H. Smith and J. Gelfand in 1980 [35].

In the theoretical work at that time, on the other hand, Wolniewicz and Kowalski reported new calculations for the pure rotational dipole moment matrix elements in 1973 [36]. The estimated value was reduced to 9.2×10^{-4} D, 60% of their previous calculation and 160% of Blinder's calculation. Two years later, Wolniewicz published two papers [37][38] in which he showed the possibility of determining the transition moments by performing an accurate perturbation-variational calculation in two steps, treating the Σ_u and Π_u contributions to the wavefunctions and the transition moments separately. Along with an improved numerical procedure, he re-calculated the HD dipole moment matrix elements for the first four rotational lines in the pure rotational, fundamental and first three overtone bands. His results agreed well with the experimental results of McKellar for all the fundamental and overtone bands, but significantly disagreed with Trefler and Gush's results for the pure rotational band. The new estimated value for the pure rotational band was about 8.38×10^{-4} D, 143% of the experimental value. This *ab initio* value was in excellent agreement with the calculations by Ford and Browne [39] in 1977 (8.3×10^{-4} D), by D. Bishop and L. Cheung [40] in 1978 (8.65×10^{-4} D), and a later different approach made by W. R. Thorson, J. H. Choi and S. K. Knudson [41][42] in 1983 (8.44×10^{-4} D).

The other important accomplishment at this time was the observation and the first interpretation of *intracollisional interference* in HD spectrum by Poll, Tipping, Prasad and Reddy in 1976 [43]. This new interference phenomenon be-

tween the allowed and induced dipole moments was found to be either constructive or destructive. They first calculated the contribution of the intracollisional interference to the absorption coefficient in HD−Kr system. This pioneer work marked the begining of the establishment of the intracollisional interference theory for the HD spectra. Two years later, Tipping, Poll and McKellar calculated the effect of intracollisional interference on the integrated intensity of lines in the pure rotational and fundamental bands within the approximation that the translational and rotational states of a collision pair do not mix [44]. They found that the intracollisional interference in pure HD was destructive and that the discrepancy between theoretical and experimental pure rotational dipole moment matrix elements for HD could be interpreted in terms of such an interference. With the important papers published by R. M. Herman [45] and by Herman, Tipping and Poll [46] in 1979, the theory, within the classical path impact formalism and reflecting the interplay between the allowed dipole and induced dipole in binary collisions, was basically formed.

With the development of the theory, considerable confirmation of the intracollisional interference in HD followed. The first detailed experimental investigation of interference effects for the pure rotational spectra of HD, and of HD with inert gases was performed by Nelson and Tabisz in 1982 [47][48]. They found that the asymmetry in those lines was small while the dependence of the integrated intensity on perturber density was significant. Rich and McKellar observed the fundamental spectra of HD and HD−X (X=He, Ne, Ar) at 77 K in 1983 [49] and then McKellar, Johns, Majewski and Rich observed pure rotational spectra

of HD and HD−Ne at 77 K in 1984 [50]; Essenwenger and Gush investigated the pure rotational spectral lines R(3)−R(6) at room temperature in 1984 [51]. They generally agreed with others on the dipole moment matrix element but disagreed on the interference parameters.

In 1985, Tabisz and Nelson published a paper in which the contributions to the intracollisional interference from the rotational-level mixing were considered and formulated [52]. As a supplement to the theory developed by Herman, Tipping and Poll, it significantly improved the agreement between the calculated and experimental results on the interference parameter for R(0) [52][53]. This effect was further confirmed by extensive studies of the pure rotational spectra of HD and HD−X (X=H_2, He, Ne, Ar, Kr, Xe, N_2) at room temperature by Drakopoulos and Tabisz in 1987 [54][55]. About a year earlier, in 1986, McKellar investigated the pure rotational spectrum of HD at room temperature [56]. Again, these two experiments agreed quite well on the dipole moment matrix element but agreed less on some line shape parameters, and the interference parameters. Morever, the discrepancy between the theoretical and experimental values of the dipole moment matrix element, and, especially, of the interference parameters was obvious.

In the mean time, the spectrum of solid HD had been first observed by Crane and Gush in 1966 [57] and then by Trefler, Cappel and Gush in 1969 [58]. In 1987, Tipping and Poll gave a detailed theoretical analysis of the pure rotational R(0) transition in solid HD [59]. The calculation was in the framework of the above intracollision theory using *ab initio* values. The result showed a

dramatic disagreement between the theoretical value of the integrated intensity of R(0) and the experimental value obtained by Trefler *et al.* (1.6 cm^{-2} versus 0.37 cm^{-2}). More dramatically, one year later, two independent experiments were carried out by McKellar and Clouter [60] and by S. Y. Lee, S. Lee, J. Gains, Tipping and Poll [61]. The experimental results for the R(0) intensity were $(1.71\pm0.15)cm^{-2}$ and $(1.68\pm0.05)cm^{-2}$ respectively, in excellent agreement with each other, and with the theoretically predicted value of Tipping and Poll. This suggested that, at least for the relatively simpler system of solid HD, the basic mechanism for intracollisional interference could be well described by the theory [53]. Nevertheless the questions concerning gaseous HD remained.

This survey concludes at 1987 when the present study started. There were several excellent reviews on this topic by Tipping and Poll [6] in 1985, by Poll[62] in 1986 and by Tabisz [1] in 1990. Interested readers should consult these references.

1.2 The Problems

It is clear, as described in the previous section, that although there has been considerable progress achieved both in the experimental and theoretical investigation in HD spectrum, this research field is still far from exhausted.

For the pure rotational spectrum of HD, experimental data only at room temperature, very few at 77 K, are available. Furthermore, even for the existing experimental data, the discrepancies remain significantly large between different experiments [63].

The intracollisional interference theory developed by Herman, Tipping and Poll can predict an accurate interference strength of pure rotational line of solid HD, a relatively simple system in which the molecules are *fixed* in the lattices. But the theory does not do so well for the systems of gaseous HD, in which the molecule has more freedom of motion and the intermolecular interaction is much more complicated than that of solid HD.

Therefore, the interference mechanism for gaseous HD is not as clear. What is needed, is a systematic investigation of the pure rotational spectral lines at different temperatures, to provide more information reflecting the intermolecular interaction in HD, or between HD and other molecules.

This study experimentally investigated the pure rotational absorption spectra of pure HD, and HD with foreign gases at $77K$, $195K$ and $296K$. Theoretical calculations were performed according to the existing theory to compare with the experimental results. It is thus an attempt to fulfil the need.

The organization of the thesis is as follows. In chapter 2, a review of the relevant theory is given. The concepts of the intracollision interference theory and its development are introduced and discussed. Details of the experiment and data analysis are presented, respectively, in chapter 3 and chapter 4. In chapter 5, the interference parameters are calculated based on the theory developed by Herman, Tipping and Poll, and by Tabisz and Nelson as well; the line broadening is calculated following a semiclassical theory developed by Robert and Bonamy. Chapter 6 centres on a comparison and discussion of experimental results and theoretical calculations. The thesis ends with a brief summary in chapter 7.

Chapter 2

THEORETICAL BACKGROUND

As was discussed in chapter one, the development of the research in HD spectrum centres on the allowed dipole moment, the collision-induced dipole moment and the interference between them. In this chapter, we will first describe the quantum approaches to the dipole moments of HD in a conceptual way, and then will focus on the discussion of the intracollisional interference based on the existing theory. The chapter will conclude with a very brief introduction of a new development of the theory [64].

2.1 The Allowed Dipole Moment of HD

Since the first calculation of the allowed dipole moment matrix element of HD by Wick in 1935, the numerical techniques and the approximations have been improved in various ways. Among those calculations, there are, basically, two different quantum mechanical approches. One is the *indirect approach*, i.e., a nonadiabatic coupling approach, and another is the *direct approach*, i.e., a

canonical transformation approach [41][42].

2.1.1 Nonadiabatic Coupling Approach

This is the most common approach used in the calculations of the allowed dipole moment of HD. The Born-Oppenheimer approximation is applied, at an early stage in solving the Schrödinger equation, to obtain adiabatic wavefunctions, and then the nonadiabatic correction in the kinetic energy part of Hamiltonian is made; the result is the existence of non-vanishing transition moments.

The Born-Oppenheimer approximation is good for the case of HD due to the smallness of the electron mass with respect to the mass of nuclei. Within the limits of the approximation, the centre of mass motion between electrons and nuclei is separated, and the Schrödinger equation is written as [65][66]

$$H\Psi(\vec{X};\vec{R}) = E\Psi(\vec{X};\vec{R}) \tag{2.1}$$

where $\vec{X} = (1,2)$ represent the electronic coordinates and $\vec{R}$ denotes the inter-nuclei coordinates. The Hamiltonian,

$$H = H_0 + H', \tag{2.2}$$

where H_0 is the *clamped nuclei* Hamiltonian,

$$H_0 = -\frac{\hbar^2}{2m}(\nabla_1^2 + \nabla_2^2) + V. \tag{2.3}$$

Here m is the electron mass, and V is the total potential. The second part of the

Hamiltonian, H', is the perturbation describing the kinetic energy of the relative motion of the c. m. (centre of mass) of the nuclei to the c. m. of the whole system [65], and the coupling between the electronic and the nuclear motions [66],

$$H' = H'_1 + H'_2 + H'_3 \tag{2.4}$$

with

$$H'_1 = -\frac{\hbar^2}{8\mu_+}(\nabla_1 + \nabla_2)^2, \tag{2.5}$$

$$H'_2 = -\frac{\hbar^2}{2\mu_+}\nabla_R^2, \tag{2.6}$$

$$H'_3 = -\frac{\hbar^2}{2\mu_-}\nabla_R \cdot (\nabla_1 + \nabla_2). \tag{2.7}$$

Here μ_+ is the reduced mass of nuclei and μ_- is the mass asymmetry,

$$\mu_+ = \frac{M_A + M_B}{M_A M_B}, \tag{2.8}$$

$$\mu_- = \frac{M_A - M_B}{M_A M_B}. \tag{2.9}$$

The corresponding eigenvalue equation of H_0 is well known and is given by

$$H_0\phi_{n\Lambda}(\vec{X};\vec{R}) = E_n(R)\phi_{n\Lambda}(\vec{X};\vec{R}) \tag{2.10}$$

In the absence of external fields, E_n depend only on the magnitude of $\vec{R}$, while $\phi_{n\Lambda}$ describe the motion of the electrons in the field of two nuclei which are not

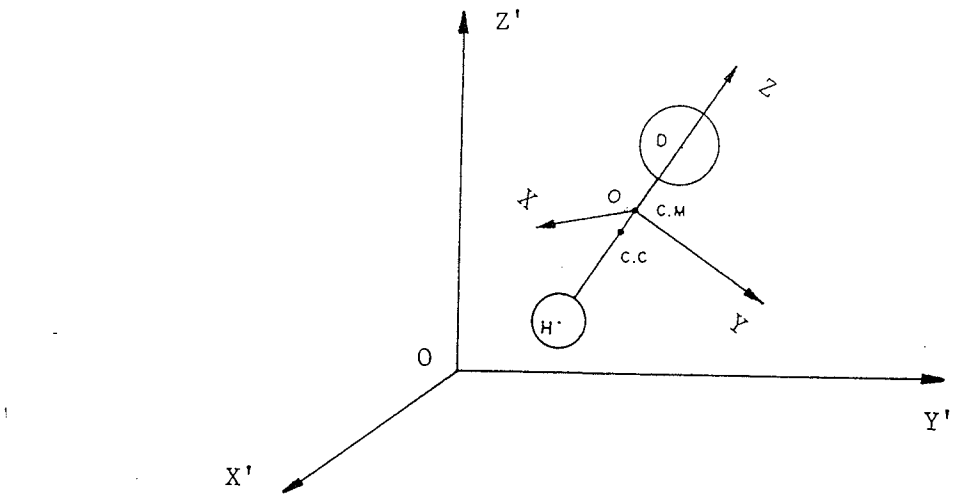

Figure 2.1: The fixed space coordinate and the c.m. coordinate of molecule HD.

spherically symmetric, and so depend on both $\vec{X}$ and $\vec{R}$ [65].

To separate the rotational motion, we follow Kolos and Wolniewicz [66][67]. In the c.m. coordinates, there are common orthonormal eigenfunctions for the square of the angular momentum $\vec{K}$ of the system, for the component of $\vec{K}$ in the direction of a fixed axis Z', and for the component of the electronic angular momentum $\vec{L}$ in the direction of Z, i.e. along the internuclear axis $\vec{R}$. If $\Omega_{JM\Lambda}$ denotes this eigenfunction, then the total wavefunction in Equation 2.1 may be written in the form

$$\Psi = \sum_{\Lambda=-J}^{J} \varphi_{J\Lambda}\Omega_{JM\Lambda}, \tag{2.11}$$

where the functions $\varphi_{J\Lambda}$ depend only on the relative position of particles. Since L_Z does not commute with H', the Hamiltonian in Equation 2.1 is not diagonal in this representation. In the adiabatic approximation, those off-diagonal terms

of Hamiltonian are neglected. Therefore the approximate total wave function, adiabatic wavefunction, can be written in the form [6]

$$\Psi^{AD} \cong [(2J+1)/4\pi]^{1/2} \Omega_{JM\Lambda} \phi_{n\Lambda} \chi_{n\Lambda vJ}. \tag{2.12}$$

These adiabatic wavefunctions will be used as a basis set for the calculations of nonadiabatic corrections. For convienence, we follow Tipping and Poll [6], defining

$$|n\Lambda vJM\rangle \equiv \Psi^{AD} \tag{2.13}$$

In a constant electric field $\vec{E}$, The Hamiltonian has an extra term and becomes

$$H = H_0 + H' - \vec{\mu} \cdot \vec{E}, \tag{2.14}$$

where $\vec{\mu}$ is the allowed electric dipole moment operator of the molecule and defined by [19]

$$\vec{\mu} = - \lim_{\vec{E} \to 0} \frac{\partial H}{\partial \vec{E}} \tag{2.15}$$

It is well known that applying the perturbation theory, we can write the energy of the molecular system to the second order based on the adiabatic wavefunction. By applying Equation 2.15 to the energy of the molecular system, we finally have

$$\langle i|\vec{\mu}|f\rangle = \sum_{n'\Lambda'v'J'M'}{}' \frac{\langle n_i\Lambda_i v_i J_i M_i|H'|n'\Lambda'v'J'M'\rangle \langle n'\Lambda'v'J'M'|\vec{\mu}|n_f\Lambda_f v_f J_f M_f\rangle}{E_{n'\Lambda'v'J'M'} - E_i}$$

$$+ \sum_{n'\Lambda'v'J'M'}{}' \frac{\langle n_i\Lambda_i v_i J_i M_i|\vec{\mu}|n'\Lambda'v'J'M'\rangle\langle n'\Lambda'v'J'M'|H'|n_f\Lambda_f v_f J_f M_f\rangle}{E_{n'\Lambda'v'J'M'} - E_f} . \tag{2.16}$$

For the pure rotational band or roto-vibrational band of HD, the initial and final state are all in the ground electronic state, i.e., n and Λ are zero [6],

$$\begin{aligned}
&\langle i|\vec{\mu}|f\rangle \\
&= \sum_{v'J'M'}{}' \frac{\langle 00v_i J_i M_i|H'|n'\Lambda'v'J'M'\rangle\langle n'\Lambda'v'J'M'|\vec{\mu}|00v_f J_f M_f\rangle}{E_{n'\Lambda'v'J'M'} - E_i} \\
&+ \sum_{v'J'M'}{}' \frac{\langle 00v_i J_i M_i|\vec{\mu}|n'\Lambda'v'J'M'\rangle\langle n'\Lambda'v'J'M'|H'|00v_f J_f M_f\rangle}{E_{n'\Lambda'v'J'M'} - E_f} .
\end{aligned} \tag{2.17}$$

The nonzero electric dipole moment requires the nonzero matrix elements in the two summations of Equation 2.17. The ground electronic state of HD is $X^1\Sigma_g^+$, with even inversion symmetry. Thus, for the nonzero $\vec{\mu}_{if}$, it requires that the intermediate states must be ungerade, i.e., with odd inversion symmetry. It follows that all terms in H' with even inversion symmetry will vanish in Equation 2.17 leaving the asymmetry term H_3'. It is this nonadiabatic perturbation term which is responsible to the occurance of electric dipole moment of HD. It remains to construct suitable adiabatic wavefunction as a basis set and to find an efficient numerical procedure.

This approach, starting with the Born-Oppenheimer approximation and ending with the break-down of the Born-Oppenheimer approximation, *indirectly* obtains the dipole moment. On the contrary, as we shall see below, Thorson, Choi

and Kundson *directly* obtained the nonzero dipole matrix element for HD by the *canonical transformations* associated with the Born-Oppenheimer approximation without considering the nonadiabatic perturbation [41][42].

2.1.2 Canonical Transformation Approach

The principle of this approach is to *find a coordinate* system such that the electrical asymmetry and the resulting dipole moment arise as purely electronic properties within a suitable Born-Oppenheimer approximation and the nonadiabatic perturbations play no role, i.e., in such coordinate system the electrical asymmetry appears directly in the electronic Hamiltonian through the potential and the nonadiabatic couplings depending only on the mass asymmetry parameter vanish exactly. To do that, a series of canonical transformations are performed. Instead of the detailed formalism, we follow Thorson *et al* [41][42] and simply list the transformations step by step.

First, let us consider an HD molecule in a space fixed coordinate system, where electrons are described by $\vec{r_i^0}$ (i=1, 2), and nuclei are described by $\vec{R}_j^0$ (j=A, B). The masses of electron and nuclei are denoted by m_0 and M_A, M_B ($M_A > M_B$) respectively.

1. *Relative* coordinates.

The coordinate system and related quantities are defined as follows,

$$\vec{r_i} = \vec{r_i^0} - \vec{R}_c^0, \quad (i = 1, 2), \tag{2.18}$$

$$\vec{R} = \vec{R}_B^0 - \vec{R}_A^0, \tag{2.19}$$

$$\vec{R}_c^0 = \frac{M_A\vec{R}_A^0 + M_B\vec{R}_B^0}{M_A + M_B}, \tag{2.20}$$

$$\mu = \frac{M_A M_B}{M_A + M_B}, \tag{2.21}$$

$$m_1 = \frac{m_0(M_A + M_B)}{M_A + M_B + m_0}, \tag{2.22}$$

$$\lambda = \frac{M_A - M_B}{M_A + M_B}, \tag{2.23}$$

and the *geometric centre electron coordinates*

$$\vec{\rho}_i = \vec{r}_i - \frac{1}{2}\lambda\vec{R}, \quad (i = 1, 2). \tag{2.24}$$

Let $\vec{P}_i$ (i=1, 2) and $\vec{P}_R$ represent canonical momenta conjugate to $\vec{r}_i$ and $\vec{R}$. Then the kinetic energy of relative motion and the electrostatic potential energy are given by

$$T = \frac{\vec{P}_R^2}{2\mu} + \frac{\vec{P}_1^2 + \vec{P}_2^2}{2m_1} + \frac{\vec{P}_1 \cdot \vec{P}_2}{M_A + M_B} \tag{2.25}$$

and

$$V = V(\vec{r}_1, \vec{r}_2; \vec{R}). \tag{2.26}$$

2. *Symmetric and antisymmetric electron* coordinates.

These coordinates are defined by

$$\vec{s} = (\vec{r}_1 + \vec{r}_2)/\sqrt{2}, \tag{2.27}$$

$$\vec{t} = (\vec{r}_1 - \vec{r}_1)/\sqrt{2}, \tag{2.28}$$

$$m_2 = \frac{m_0(M_A + M_B)}{M_A + M_B + 2m_0}. \tag{2.29}$$

Transforming to this coordinate system, the kinetic and potential energy become

$$T = \frac{\vec{P}_R^2}{2\mu} + \frac{\vec{P}_s^2}{2m_2} + \frac{\vec{P}_t^2}{2m_0} \tag{2.30}$$

and

$$V = V(\vec{s}, \vec{t}; \vec{R}), \tag{2.31}$$

where $\vec{P}_s$ and $\vec{P}_t$ are the canonical momenta conjugate to $\vec{s}$ and $\vec{t}$ respectively.

3. *Mass-scaled* coordinates.

In these coordinates,

$$\underline{\vec{s}} = \sqrt{m_2}\vec{s}, \tag{2.32}$$

$$\underline{\vec{R}} = \sqrt{\mu}\vec{R}, \tag{2.33}$$

and so their conjugate momenta become

$$\underline{\vec{P}_s} = \vec{P}_s/\sqrt{m_2}, \tag{2.34}$$

$$\underline{\vec{P}_R} = \vec{P}_R/\sqrt{\mu}. \tag{2.35}$$

Now the T and V are in the form

$$T = \frac{1}{2}(\underline{\vec{P}_R^2} + \underline{\vec{P}_s^2}) + \underline{\vec{P}_t^2}/2m_0, \tag{2.36}$$

$$V = V(\underline{\vec{s}}, \vec{t}; \underline{\vec{R}}). \tag{2.37}$$

4. *New* coordinates.

The transformation to the *New* coordinates is made by performing a *rotation* as follows,

$$\vec{\xi} = \vec{R}\cos\sigma_0 + \vec{s}\sin\sigma_0, \tag{2.38}$$

$$\vec{\eta} = -\vec{R}\sin\sigma_0 + \vec{s}\cos\sigma_0, \tag{2.39}$$

with

$$\tan\sigma_0 = \lambda(\frac{m_2}{2\mu})^{1/2}. \tag{2.40}$$

Thus, with their canonical momenta $\vec{P}_\xi$ and $\vec{P}_\eta$, the kinetic and potential energy are written

$$T = \frac{1}{2}(\vec{P}_\xi^{\,2} + \vec{P}_\eta^{\,2}) + \vec{P}_t^{\,2}/2m_0, \tag{2.41}$$

$$V = V(\vec{\xi}, \vec{\eta}, \vec{t}). \tag{2.42}$$

5. *Heavy-particle and symmetric electron* coordinates.

These are defined by

$$\vec{\xi} = (\sqrt{\mu}\cos\sigma_0)\vec{P}_\xi, \tag{2.43}$$

and

$$\vec{\eta} = (\frac{\sec\sigma_0}{\sqrt{m_2}})\vec{\eta} \tag{2.44}$$

with their conjugate momenta,

$$\vec{P}_\xi = (\sqrt{\mu}\cos\sigma_0)\underline{\vec{P}}_\xi, \tag{2.45}$$

$$\vec{P}_\eta = (\sqrt{m_2}\cos\sigma_0)\underline{\vec{P}}_\eta. \tag{2.46}$$

Making use of the definitions in the *New* coordinates and Equation 2.24, we obtain the relationships

$$\vec{\xi} = \vec{R} + \frac{\lambda m_2}{\sqrt{2}\mu}\vec{s}, \tag{2.47}$$

$$\vec{\eta} = \frac{\vec{\rho_1} + \vec{\rho_2}}{\sqrt{2}}, \tag{2.48}$$

and

$$\vec{t} = \frac{\vec{\rho_1} - \vec{\rho_2}}{\sqrt{2}}. \tag{2.49}$$

The kinetic and potential energy are now given by

$$T = \frac{\vec{P}_\xi^2}{\mu\cos^2\sigma_0} + \frac{\vec{P}_\eta^2}{2m_2\cos^2\sigma_0} + \frac{\vec{P}_t^2}{2m_0}, \tag{2.50}$$

$$V = V(\vec{\eta}, \vec{\xi}, \vec{t}). \tag{2.51}$$

6. *Electron and heavy particle* coordinates

These coordinates are based on the *geometric centre electron* coordinate and the *heavy particle* coordinate mentioned in sections 1 and 5

$$\vec{\rho_1} = (\vec{\eta} - \vec{t})/\sqrt{2}, \tag{2.52}$$

and

$$\vec{\rho_2} = (\vec{\eta} + \vec{t})/\sqrt{2}. \tag{2.53}$$

With the conjugate momenta of electrons, $\vec{\pi_1}$ and $\vec{\pi_2}$, the *exact* relative kinetic and potential energy are expressed by

$$T = \frac{\vec{P}_\xi^2}{2\mu'} + \frac{\vec{\pi}_1^2 + \vec{\pi}_2^2}{2m'} + \frac{\vec{\pi}_1 \cdot \vec{\pi}_2}{4\mu}, \tag{2.54}$$

$$V = V_\xi(\vec{\rho}_1, \vec{\rho}_2; \vec{\xi}), \tag{2.55}$$

where

$$\mu' = \mu \cos^2 \sigma_0, \tag{2.56}$$

and

$$m' = m_0(1 + m_0/4\mu)^{-1}. \tag{2.57}$$

Thus, the canonical transformations are completed in the coordinates $(\vec{\rho_1}, \vec{\rho_2}; \vec{\xi})$. We now discuss the Hamiltonian applying the Born-Oppenheimer separation in the usual way. The electronic Hamiltonian is given by

$$H = \frac{\vec{\pi}_1^2 + \vec{\pi}_2^2}{2m'} + \frac{\vec{\pi}_1 \cdot \vec{\pi}_2}{4\mu} + V_\xi(\vec{\rho}_1, \vec{\rho}_2; \vec{\xi}) \ . \tag{2.58}$$

The potential V in the $(\vec{\rho_1}, \vec{\rho_2}; \vec{R})$ coordinates has the form

$$V(\vec{\rho}_1, \vec{\rho}_2; \vec{R}) = -e^2 \sum_{i=1,2} [\frac{1}{|\vec{\rho}_i + \vec{R}|} + \frac{1}{|\vec{\rho}_i - \vec{R}|}] + \frac{e^2}{|\vec{\rho}_1 - \vec{\rho}_2|} + \frac{e^2}{R} \ . \tag{2.59}$$

Note that in this expression V is invariant under the inversion $\vec{\rho_i} \rightarrow -\vec{\rho_i}$. To transform $V(\vec{\rho_1}, \vec{\rho_2}; \vec{R})$ to $V_\xi(\vec{\rho_1}, \vec{\rho_2}; \vec{\xi})$, we use the the relationship

$$\begin{aligned} \vec{R} &= [\vec{\xi} - \frac{1}{2}(\frac{\lambda m}{\mu}(\vec{\rho_1} + \vec{\rho_2})] \cos^2 \sigma_0 \\ &= \vec{\xi_0} - \alpha_0(\vec{\rho_1} + \vec{\rho_2}), \end{aligned} \tag{2.60}$$

where

$$\vec{\xi_0} = \vec{\xi} cos^2 \sigma_0, \tag{2.61}$$

$$\alpha_0 = \frac{1}{2}(\frac{\lambda m}{\mu}) cos^2 \sigma_0. \tag{2.62}$$

The explicit form of V_ξ is now written as

$$\begin{aligned} V_\xi(\vec{\rho_1}, \vec{\rho_2}; \vec{R}) = & -e^2 \sum_{i=1,2} (\frac{1}{|\vec{\rho_i} + \frac{1}{2}\vec{\xi_0} - \frac{\alpha_0}{2}(\vec{\rho_1} + \vec{\rho_2})|} + \frac{1}{|\vec{\rho_i} - \frac{1}{2}\vec{\xi_0} + \frac{\alpha_0}{2}(\vec{\rho_1} + \vec{\rho_2})|}) \\ & + \frac{e^2}{|\vec{\rho_1} - \vec{\rho_2}|} + \frac{e^2}{|\vec{\xi_0} - \alpha_0(\vec{\rho_1} + \vec{\rho_2})|}. \end{aligned} \tag{2.63}$$

Now that because of the coupling of $\vec{\xi}$ with $\vec{\rho_i}$, $V_\xi(\vec{\rho_1}, \vec{\rho_2}; \vec{\xi})$ does not have $D_{\infty h}$ symmetry with respect to the $\vec{\xi}$ axis any more. It means that V_ξ is the sum of a symmetric part $V_{\xi s}$ and an asymmetric part $V_{\xi a}$, which further implies that in the new coordinate system the two nuclei appear *electrically* different. Conseqently a permanent electric dipole moment would *directly* arise in the usual way as for the polar molecule, and for the ground electronic state it could be computed with a purely electronic basis set. Indeed, the calculation by Thorson *et al.* was in

Table 2.1: The theoretical calculations of the matrix elements of the allowed dipole moment transitions of HD $(10^{-4} debye)$, in the direction H^+D^-.

Reference	Year	$\langle J\|\mu^A\|J+1\rangle$			
		$J=0$	$J=1$	$J=2$	$J=3$
Wolniewicz[a]	1976	8.36	8.38	8.39	8.41
Ford and Browne[b]	1977	8.31	8.30	8.29	8.26
Bishop and Cheung[c]	1978	8.65			
Thorson *et al*[d]	1985	8.463	8.455	8.440	8.420

a: Reference [38].

b: Reference [39].

c: Reference [40].

d: Reference [42].

excellent agreement with the nonadiabatic calculation by Ford and Browne. The published theoretical calculations of the two different approaches are collected in Table 2.1.2.

2.2 Collision-Induced Dipole Moment

The induced dipole moment of a collision pair, such as $HD - X$, contains an isotropic part directed along the intermolecular axis, and an anisotropic part which can have any orientation [65]. The mechanisms which generate the induced dipole are clearly related to the interaction terms in the intermolecular potential: multipolar induction, dispersion interaction and electronic exchange [1][68][69][70]. Thus, in general, for the collision pair of HD and a linear molecule, the induced dipole moment is a function of the internuclear separations $\vec{r}_1 \equiv (r_1, \vec{\omega}_1)$, $\vec{r}_2 \equiv (r_2, \vec{\omega}_2)$ and the separation between the c.m. of the two interacting molecules, $\vec{R} \equiv (R, \vec{\Omega})$. The total dipole moment of the collision pair is given by [44]

$$\vec{\mu}(\vec{r}_1, \vec{r}_2, \vec{R}) = \mu_1(\vec{r}_1) + \mu_2(\vec{r}_2) + \mu^I(\vec{r}_1, \vec{r}_2, \vec{R}), \tag{2.64}$$

where μ_1 and μ_2 are the allowed dipole moments of molecule 1 and 2, and μ^I is the induced dipole moment. The total dipole moment is defined in the limit of adiabatic approximation [44],

$$\vec{\mu}(\vec{r}_1, \vec{r}_2, \vec{R}) = \langle \Psi_e^{AD} | \vec{\mu} | \Psi_e^{AD} \rangle, \tag{2.65}$$

where Ψ_e^{AD} is the electronic part of the adiabatic eigenfunction of the collision pair. Then the induced dipole moment matrix elements are calculated with the adiabatic nuclear wave functions with the assumption that the rotational and translational motions of nuclei are separated completely [44]. The most efficient way of characterizing the induced dipole moment is to expand the angular depen-

dence in terms of a complete set of eigenfunctions of the total angular momentum [6][62], i.e.,

$$\mu_\nu(\vec{r}_1,\vec{r}_2,\vec{R}) = \frac{(4\pi)^{3/2}}{\sqrt{3}} \sum_{\lambda_1,\lambda_2,L,\Lambda} A_\Lambda(\lambda_1\lambda_2 L; r_1, r_2, R)\Psi_{1\nu}^{(\lambda_1\lambda_2 L;\Lambda)}(\vec{\omega}_1,\vec{\omega}_2,\vec{\Omega}), \quad (2.66)$$

or

$$\begin{aligned}\mu_\nu(\vec{r}_1,\vec{r}_2,\vec{R}) &= \frac{(4\pi)^{3/2}}{\sqrt{3}} \sum_{\lambda_1,\lambda_2,L,\Lambda} A_\Lambda(\lambda_1\lambda_2 L; r_1, r_2, R) \\ &\times \sum_{\mu_1\mu} C(\Lambda L 1; \mu, \nu-\mu) C(\lambda_1\lambda_2\Lambda; \mu_1, \mu-\mu_1) \\ &\times Y_{\lambda_1,\mu_1}(\vec{\omega}_1) Y_{\lambda_2,\mu-\mu_1}(\vec{\omega}_2) Y_{L,\nu-\mu}(\vec{\Omega}) \ . \end{aligned} \quad (2.67)$$

Here $\nu = 0, \pm 1$ is the index of the spherical component related to the Cartesian components according to $\mu_0 = \mu_z$, and $\mu_{\pm 1} = \mp(\mu_x \pm i\mu_y)/\sqrt{2}$, the C's are the Clebsch-Gorden coefficients [71] and the Y's are spherical harmonics. The real expansion coefficients $A_\Lambda(\lambda_1\lambda_2 L; r_1, r_2, R)$, with the same dimension of μ_ν, are thus the components of the pair dipole moment and provide an invariant classification of the induction effects in terms of parameters λ_1, λ_2, L and Λ [72]. There are a few restrictions on these parameters concerning the parity of μ_ν and the well known triangle relations of the C's [73][74]:

$$\lambda_1 + \lambda_2 + L \ \rightarrow \ odd, \quad \triangle(\Lambda, L, 1) \ and \ \triangle(\lambda_1, \lambda_2, \Lambda). \quad (2.68)$$

In addition, for homonuclear diatomic molecules like H_2, only λ even can occur.

The allowed dipole moment of molecule 1 can be expressed in the form of Equation 2.67 with the only argument r_1. By the substituting of $\Lambda = 1$, $\lambda_1 = 1$ and $\lambda_2 = L = 0$, one has [62]

$$\mu_\nu^A(r_1) = \sqrt{\frac{4\pi}{3}} A_1(100; r_1) Y_{1,\nu}(\omega_1). \tag{2.69}$$

Note that the intracollisional interference occurs only if the induced dipole component has the same symmetry as that of allowed dipole moment, i.e. $\Lambda = 1$, $\lambda_1 = 1$ and $\lambda_2 = L = 0$. Conventionally, the induced dipole component $A_\Lambda(\lambda_1\lambda_2 L; r_1, r_2, R)$ is named by referring to the dipole associated with the isotropic or anisotropic part of the polarizability of the collision partner. As well, the symmetry depends on the parameters Λ, λ_1, λ_2 and L. Thus, $A_0(001; r_1, r_2, R)$ is the *isotropic overlap* induced dipole and $A_2(201; r_1, r_2, R)$ is the *anisotropic overlap* induced dipole, etc. For details of A coefficients in the standard representation for multipolar induction, we refer the reader to Reference [6].

In the case of HD, the electronic distribution is the same as that of H_2. They have the same adiabatic wavefunction for the electronic part of the Hamiltonian. The only difference is that in HD, the c. m. (the centre of mass) of the molecule is shifted by d relative to the c. c. (the centre of the static charge of the molecule) due to the different mass of atom H and D, as shown in Figure 2.2. Thus the induced dipole components for H_2 systems are suitable for the systems of HD with a coordinate transformation, i.e.

$$\mu_\nu^{HD-X}(r_1, r_2, R) \equiv \mu_\nu^{H_2-X}(r_1, r_2, S), \tag{2.70}$$

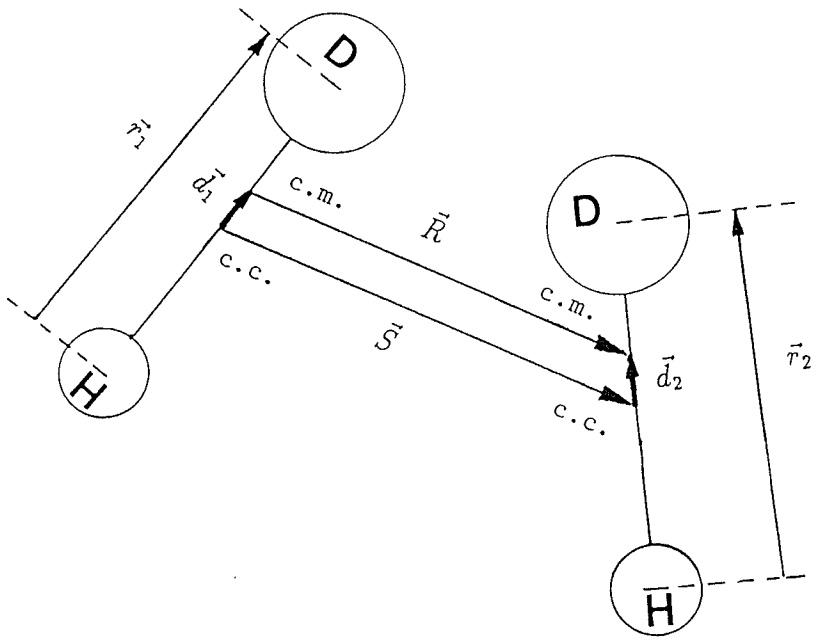

Figure 2.2: Orientation of $HD - HD$.

with

$$\vec{S} = \vec{R} + (\vec{d}_1 - \vec{d}_2). \tag{2.71}$$

Applying the standard coordinate transformation to the first order in $(\vec{d}_1 - \vec{d}_2)$, one has [75]

$$\mu_\nu^{HD-X}(r_1, r_2, R) \equiv [1 + (\vec{d}_1 - \vec{d}_2) \cdot \nabla_R]\ \mu_\nu^{H_2-X}(r_1, r_2, R). \tag{2.72}$$

Under a similar transformation, though the calculations are complicated [71], one can rewrite the second term of Equation 2.72 in the same form as in the standard representation [6]

$$\begin{aligned} A_\lambda(l\lambda_2 L + \gamma; r_1, r_2, R) &= d_1[O_\gamma^L A_\Lambda(\lambda_1\lambda_2 L; r_1, r_2, R)](-1)^{L+\lambda-1} \\ &\times[(2\lambda_1+1)(2\Lambda+1)(2L+1)(2\lambda+1)]^{\frac{1}{2}} C(1\lambda_1 l; 00) \\ &\times C(1lL+\gamma; 00) W(1l\Lambda\lambda_2; \lambda_1\lambda) W(L+\gamma L\lambda\Lambda; 11) \end{aligned} \tag{2.73}$$

and

$$\begin{aligned} A_\lambda(\lambda_1 lL + \gamma; r_1, r_2, R) &= d_2[O_\gamma^L A_\Lambda(\lambda_1\lambda_2 L; r_1, r_2, R)](-1)^{L+\Lambda-1} \\ &\times[(2\lambda_2+1)(2\Lambda+1)(2L+1)(2\lambda+1)]^{\frac{1}{2}} C(1\lambda_2 l; 00) \\ &\times C(1LL+\gamma; 00) W(1l\Lambda\lambda_1; \lambda_2\lambda) W(L+\gamma L\lambda\Lambda; 11), \end{aligned} \tag{2.74}$$

with

$$O_{\gamma}^{L} = \begin{cases} d/dR - L/R & \gamma = +1 \\ d/dR + (L+1)/R & \gamma = -1. \end{cases} \tag{2.75}$$

Obviously, for $HD - atom$ system,

$$d_2 = 0 \tag{2.76}$$

and

$$d_1 = r_e/6, \tag{2.77}$$

where r_e is the equilibrium separation of the nucleis of HD. Meyer *et al.* calculated *ab initio* induced dipole components for $H_2 - X$ systems by using self-consistent (SCF), configuration interaction (CI) and coupled electron pair approximation (CEPA). They also calculated induced dipole components for $HD - X$ systems by a coordinate transformation including high order terms [69][76][77]. Their results will be used in our calculations in chapter 5.

2.3 Intracollisional interference

2.3.1 Impact Theory

The existing theories regarding line shape, including the theory developed by Herman, Tipping and Poll for HD, are essentially within the limits of the *impact theory*. There are two important approximations, *impact* approximation and the *classical path* approximation [78][79]. The impact approximation assumes that the duration of collision is much smaller, and so is negligible, com-

pared to the time between collisions. Within this limit, only the final changes produced by the collision are taken into account, while the direct influence of the happenings during the collision on the spectra is entirely ignored [4]. It leads to two sub-assumptions; only *binary* collisions are of importance, and the binary collisions are statistically independent.

The impact approximation requires, in the spectroscopy, that for the frequencies of absorption or emission of our interests, the detuning from resonance is small compared with the inverse of a collision duration [80], i.e.,

$$\Delta\tau_d \ll 1, \tag{2.78}$$

where Δ is the detuning and τ_d is the duration of collision. In the case of HD, for the pure rotational band and up to 100 amagat of density(Table 4.9),

$$\Delta \leq 10^{10}\ Hz. \tag{2.79}$$

The duration τ_d is usually of order $10^{-12} - 10^{-14}\ sec$ [81][64]. Therefore,

$$\Delta\tau_d \sim\ 10^{-2} - 10^{-4}, \tag{2.80}$$

is suitable for the impact approximation in the range of our study.

The classical path approximation assumes that the translational motion of molecule can be treated as that for a classical particle without significant error [4]. It permits the density matrix of the collision pair to be written as a product of absorber and perturber density matrices; therefore, the correlation function

can be written as the sum over all substates of the Boltzmann ensemble average of the correlation of the absorber density matrices [46].

The impact and classical path approximations are both applied in the theory developed by Herman, Tipping and Poll [46].

2.3.2 interference between the Collision Pair

The picture of the system is the following [46]. The absorbing molecule is immersed in a bath of perturbers. Only the molecule, referred to as absorbing molecule, can absorb radiation. The others are all referred to as perturber molecules in a total number of N.

The total dipole moment operator of the system is defined by

$$\vec{\mu}(t) = e^{iHt/\hbar}\vec{\mu}e^{-iHt/\hbar} , \tag{2.81}$$

and

$$\vec{\mu}(t) = \vec{\mu}^A(t) + \sum_j \vec{\mu}_j^I(t) , \tag{2.82}$$

where $\vec{\mu}^A$ is the allowed dipole moment operator of the absorber, and $\vec{\mu}_j^I$ is the induced dipole moment operator in a binary collision between absorber and perturber. The dipole moment correlation function is defined as the ensemble average of the product of the time correlated dipole moments,

$$C(t) = < \vec{\mu}(0) \cdot \vec{\mu}(t) >_{ens} . \tag{2.83}$$

With the substitution of Equation 2.82 in Equation 2.83, the correlation function

can be written in the form

$$C(t) = C^{AA}(t) + C^{AI}(t) + C^{IA}(t) + C_1^{II}(t) + C_2^{II}(t), \tag{2.84}$$

with

$$C^{AA}(t) = < \vec{\mu}^A(0) \cdot \vec{\mu}^A(t) >_{ens}, \tag{2.85}$$

$$C^{AI}(t) = N < \vec{\mu}^A(0) \cdot \vec{\mu}^I(t) >_{ens}, \tag{2.86}$$

$$C^{IA}(t) = N < \vec{\mu}^I(0) \cdot \vec{\mu}^A(t) >_{ens}, \tag{2.87}$$

$$C_1^{II}(t) = N < \vec{\mu}^I(0) \cdot \vec{\mu}^I(t) >_{ens}, \tag{2.88}$$

$$C_2^{II}(t) = N^2 < \vec{\mu}_j^I(0) \cdot \vec{\mu}_k^I(t) >_{ens}, \tag{2.89}$$

where j and k refer to different perturbers.

The first term $C^{AA}(t)$ represents the allowed-allowed dipole contributions. The strength of this term obviously depends on the number density of the absorber.

The second and third term, $C^{AI}(t)$ and $C^{IA}(t)$, are the contributions from allowed-induced dipoles. These are the terms representing the intracollisional interference between allowed dipole moment and the collision-induced dipole moment produced by a binary collision of absorber and perturber, and hence the strength depends on both the number densities of absorber and perturber molecules. We have to keep in mind that such interference could occur only if the allowed dipole moment and induced dipole moments have the same symmetry. In the standard representation, as was described in previous sections, only the induced

dipole component with the symmetry of $A_1(100; r_1, r_2R)$ can interfere with the allowed dipole.

The fourth term, $C_1^{II}(t)$ refers to the correlation of an induced dipole moment produced by a binary collision of absorber and perturber with itself at a later time. For a single binary collision the correlation between $\vec{\mu}^I(0)$ and $\vec{\mu}^I(t)$ extends only over the duration τ_d, resulting in a very broad spectrum with a typical width $\Delta\omega \sim \tau_d^{-1}$, i.e. of order 100 cm^{-1} at normal condition [62]. Due to this reason, we will not discuss this term further in this thesis.

The last term, $C_2^{II}(t)$, describes the absorption due to the induced dipoles created by two binary collisions of the absorber with perturbers j and k. Usually this term is referred to as *intercollisional interference* presenting the narrow features as a sharp dip at the transition frequency in the spectra of H_2, which was first discussed by J. C. Lewis and J. Van Kranendonk in 1972 [82]. But in the case of HD, this interference behaves entirely differently. The induced dipole component of $A_1(100; r_1, r_2, R)$, with $L = 0$, now is a *scalar* function in the translational variable $\vec{R}$, rather than the $L = 1$ component in the case of H_2 which is a *vector*. Herman named this interference, *scalar collisional interference* [83]. The scalar collisional interference is always constructive, and such constructive interference can always happen between the dipoles induced by absorber in any two subsequent collisions with perturbers j and k. The correlation function then extends over arbitrarily long time and results in sharp spectral lines [62][83]. Since these binary collisions involve two perturber molecules, the strength of this term depends on the number density of the absorber and the density squared of the

perturber.

2.3.3 Spectral Profile

In the spectrum, the absorption coefficient per unit wavenumber at frequency ω is given by

$$\frac{\alpha(\omega)}{\omega} = \rho_A N_0 (\frac{4\pi^2}{3\hbar c})[1 - \exp(-\hbar\omega/kT)]\phi(\omega), \tag{2.90}$$

where ρ_A is the density of absorber, N_0 is Loschmidt's number, and $\phi(\omega)$ is the spectral line shape function or spectral density function defined by a *Fourier* transformation of the correlation function [54],

$$\phi(\omega) = \frac{1}{\pi} Re[\int_0^\infty e^{-i\omega t} C(t)\ dt]. \tag{2.91}$$

From the additive property of the Fourier transformation, the total contribution to the spectral density function, and therefore to the absorption coefficient, will be the sum of the contributions from the different terms in the correlation function, as was discussed in the previous section. Within the impact and classical path approximation the first term, $C^{AA}(t)$ may be expressed as [46]

$$< \vec{\mu}^A(0) \cdot \vec{\mu}^A(t) >_{ens} = \sum_{i,f} P_{ii} < \vec{\mu}^A_{if}(0) \cdot \vec{\mu}^A_{fi}(t) >_T, \tag{2.92}$$

where P_{ii} is the density matrix of absorber, i and f denote the substates associated with *initial* and *final* energy levels respectively and $< \cdots >_T$ is the Boltzmann ensemble average over the translational motion. To consider this term with the

effects associated with the time average of the dipole operator magnitude itself, which is modulated by the collision strength, the above expression may be re-written as [83]

$$< \vec{\mu}^A(0) \cdot \vec{\mu}^A(t) >_{ens} = \sum_{i,f} P_{ii} < |\vec{\mu}^A_{if}(0) \cdot \vec{\mu}^A_{fi}(t)| >_T e^{(i\omega_0^0 - \Gamma_0)t}. \tag{2.93}$$

Here ω_0^0 is the unshifted frequency centre of the resonance line, and

$$\Gamma_0 = \gamma/2 + i\delta, \tag{2.94}$$

where γ is the full width at half intensity (FWHM) and δ represents the line shift with respect to ω_0^0. For the isolated pure rotational lines, the Fourier transform of Equation 2.93 gives a pressure broadened Lorentzian contour

$$\phi^{AA}(\omega) = (J+1)P_B(J)\langle J|\mu^A|J+1\rangle^2 \frac{\gamma/2\pi}{(\gamma/2)^2 + (\omega - \omega_0)^2}, \tag{2.95}$$

where J is the rotational quantum number, $\omega_0 = \omega_0^0 - \delta$ is the shifted frequency peak and $P_B(J)$ is the Boltzmann factor normalized according to

$$\sum_J (2J+1)P_B(J) = 1. \tag{2.96}$$

This is obviously a symmetric line shape with γ as FWHM, and the shifted peak frequency ω_0.

Now let us consider the intracollisional interference terms $C^{AI}(t)$ and $C^{IA}(t)$.

In analogy with the calculation of $C^{AA}(t)$, the term $C^{AI}(t)$ may be written by

$$< \vec{\mu}^A(0) \cdot \vec{\mu}^I(t) >_{ens} = \sum_{i,f} P_{ii} < |\mu^A_{if}(0) \cdot \mu^I_{fi}(t)| >_T e^{(i\omega_0'' - \Gamma_0)t}. \tag{2.97}$$

In order to interpret the dispersion line shape observed in the fundamental band of HD [25], Herman *et al.* introduced a *dipole weighted phase factor* Δ to describe, phenomenologically [62] the phase shift produced during the dipole induction itself [46][83],

$$\begin{aligned} \mu^I_{fi} &= I\mu^A_{fi}\Delta \\ &= I\mu^A_{fi}(\Delta' + i\Delta''), \end{aligned} \tag{2.98}$$

where

$$I = \frac{\int_0^\infty \int_0^{2\pi} \int_0^\pi \mu^I_{fi}(R) g(R) R^2 \sin\theta \; dR \; d\phi \; d\theta}{\mu^A_{fi}}. \tag{2.99}$$

Here $g(R)$ is the pair correlation function. The phase factor Δ, according to Herman *et al.*, can also be expressed in terms of an average over single collisions in the so-called *double* space or *line* space [46][84]

$$\Delta = \frac{\ll if|P[R(t)]U_i(\tau_c)U_f^\dagger(\tau_c)|if \gg}{< P(R) >_T}, \tag{2.100}$$

where

$$P(R) = \mu^I_{fi}(R)/\mu^A_{fi}. \tag{2.101}$$

With the introduction of the complex phase factor Δ, Equation 2.97 becomes

$$< \vec{\mu}^A(0) \cdot \vec{\mu}^I(t) >_{ens} = \sum_{i,f} P_{ii} < |\mu^A_{if}(0) \cdot \mu^A_{fi}(t) I(\Delta' + i\Delta'')| >_T e^{(i\omega_0^0 - \Gamma_0)t}. \quad (2.102)$$

and the corresponding Fourier transform gives the spectral density function as a sum of Lorentzian contour and a dispersion part,

$$\phi^{AI}(\omega) = (J+1) P_B(J) \langle J|\mu^A|J+1\rangle^2 I[\frac{\Delta'\gamma/2\pi}{(\gamma/2)^2 + (\omega - \omega_0)^2} + \frac{\Delta''(\omega - \omega_0)/\pi}{(\gamma/2)^2 + (\omega - \omega_0)^2}]. \quad (2.103)$$

It can be seen in Equation 2.102 that the $C^{IA}(t)$ term has the same contribution to the spectral density function as that of $C^{AI}(t)$.

The intercollisional interference term, $C_2^{II}(t)$, can be treated in the same manner. With the phase factor Δ, the correlation function is then in the form

$$C_2^{II} = \sum_{i,f} P_{ii} < |\vec{\mu}^A_{if}(0) \cdot \vec{\mu}^A_{fi}(t) I^2(\Delta' + i\Delta'')^2| >_T e^{(i\omega_0^0 - \Gamma_0)t} \quad (2.104)$$

and its contribution to the spectral density function is given by

$$\begin{aligned} \phi_2^{II}(\omega) &= (J+1) P_B(J) \langle J|\mu^A|J+1\rangle^2 I^2 \\ &\quad \times [\frac{(\Delta'^2 - \Delta''^2)\gamma/2\pi}{(\gamma/2)^2 + (\omega - \omega_0)^2} + \frac{2\Delta'\Delta''(\omega - \omega_0)/\pi}{(\gamma/2)^2 + (\omega - \omega_0)^2}]. \end{aligned} \quad (2.105)$$

Therefore, for a system with $\rho_A N_0$ absorber and ρN_0 perturber molecules ($\rho_A \ll \rho$), with all of the above contributions taken into account, the total absorption

coefficient is obtained in the form

$$\begin{aligned}\frac{\alpha(\omega)}{\omega} &= \rho_A N_0(\frac{4\pi^2}{3\hbar c})(J+1)P(J)\langle J|\mu^A|J+1\rangle^2 \\ &\times\{[1+2\rho N_0\Delta' I+\rho^2 N_0^2(\Delta'^2-\Delta''^2)I^2]\frac{\gamma/2\pi}{(\gamma/2)^2+(\omega-\omega_0)^2} \\ &+(\rho N_0\Delta'' I+\rho^2 N_0^2\Delta'\Delta'' I^2)\frac{2(\omega-\omega_0)/\pi}{(\gamma/2)^2+(\omega-\omega_0)^2}\}\ ,\end{aligned} \tag{2.106}$$

with

$$P(J) = P_B(J)[1-exp(-\hbar\omega/kT)]\ .$$

Since the dispersion part is odd symmetric with respect to ω, this part will not contribute to the integrated absorption coefficient,

$$\begin{aligned}\int_{-\infty}^{\infty}\frac{\alpha(\omega)}{\omega}d\omega &= \rho_A N_0(\frac{4\pi^2}{3\hbar c})(J+1)P(J)\langle J|\mu^A|J+1\rangle^2 \\ &\times[1+2\rho N_0\Delta' I+\rho^2 N_0^2(\Delta'^2-\Delta''^2)I^2].\end{aligned} \tag{2.107}$$

2.4 Rotational-level Mixing

As was mentioned in earlier sections, the basis set for the calculation of the induced dipole moment components is the nuclear wavefunction with the assumption that the rotational and translational motions are separated completely, i.e., the mixing of the rotational and translational states is ignored. The possible significance of the rotational-level mixing is however well understood [44].

In the case of $H_2 - H_2$, the intermolecular potential is almost spherical

with a negligible anisotropic *quadrupole-quadrople* interaction term. But in the $HD-HD$ system, the intermolecule potential has an additional anisotropic term due to the shift of the c.m. with respect to the c.c, as described in Figure 2.2,

$$\begin{aligned} V_{HD}(R) &= [1+\vec{d}\cdot\nabla_R]V_{H_2}(R) \\ &= V_{H_2}(R)+V_{aniso}(R,\theta). \end{aligned} \tag{2.108}$$

Here θ is the angle between $\vec{d}$ and intermolecular distance $\vec{R}$, as shown in the figure. When this anisotropic potential term is taken into account in the Hamiltonian, the mixing of rotational states ensues [52].

Tabisz and Nelson derived the expression of the rotational-level mixing for the pure rotational band in 1985 [52]. The calculation was performed assuming that the quantum numbers of the translational states do not change in the mixing process. The mixing was calculated for a fixed intermolecular separation and then was averaged over the separation R. The total anisotropic potential was written as

$$V_A(R,\theta) = V_{Q_1Q_2} + V_{aniso}(R,\theta), \tag{2.109}$$

where $V_{Q_1Q_2}$ denotes the *quadrupole-quadrupole* term. The rotational wavefunctions then were corrected as follows,

$$\Phi_{JM} = \phi_{JM} + \sum_{J'',M''}{}' \frac{\langle J''M''|V_A|JM\rangle}{E_{J''}-E_J}\phi_{J''M''}. \tag{2.110}$$

This calculation was corrected by Ma, Tipping and Poll in 1988 who showed that

a nonzero contribution to the interference occurs only for R(0) [53]. With the same wavefunctions in the calculations leading to Equation 2.107, the *additional* contribution to the integrated absorption coefficient for $R(0)$ for $HD-HD$ and $HD-X$ systems is given by [53][85]

$$\Delta[\int \frac{\alpha(\omega)}{\omega}d\omega] = \rho_A N_0(\frac{4\pi^2}{3\hbar c})(J+1)P(J)\langle J|\mu^A|J+1\rangle \times \frac{\rho N_0}{2\sqrt{2}B_0}(\frac{\delta_{J,0}}{2J+1}) \times \int_0^\infty \int_0^{2\pi} \int_0^\pi A_2(201;R)V_A(R,\theta)g(R)R^2 \sin\theta dR d\phi d\theta, \tag{2.111}$$

Here B_0 is the rotational constant of HD. Details of the numerical calculations of the contributions to the interference parameter for $HD-HD$ and $HD-X$ systems will be presented in chapter 5.

There is another type of rotational-level mixing mechanism, the *near-resonance rotational-level* mixing, which was calculated by Ma, Tipping and Poll in 1988 [53]. This mechanism involves the rotational levels of both molecules in a colliding pair $HD-HD$. This type of rotational-level mixing is due to the relatively small energy difference between two resonance rotational levels of a colliding pair compared to the anisotropic interaction of the proper symmetry required to mix these levels [53]. Figure 2.3 schematically illustrates the mechanism of the near- resonance rotational-level mixing, where $|J_1M_1;J_2M_2;LM\rangle$ denotes the unperturbed states of *colliding pair*, LM designates the angular part of the relative translational wavefunction [53] and $|J_iM_i\rangle$ denotes the unperturbed rotational states of HD *molecule* in a colliding pair. Note that only $R(2)$ and $R(3)$

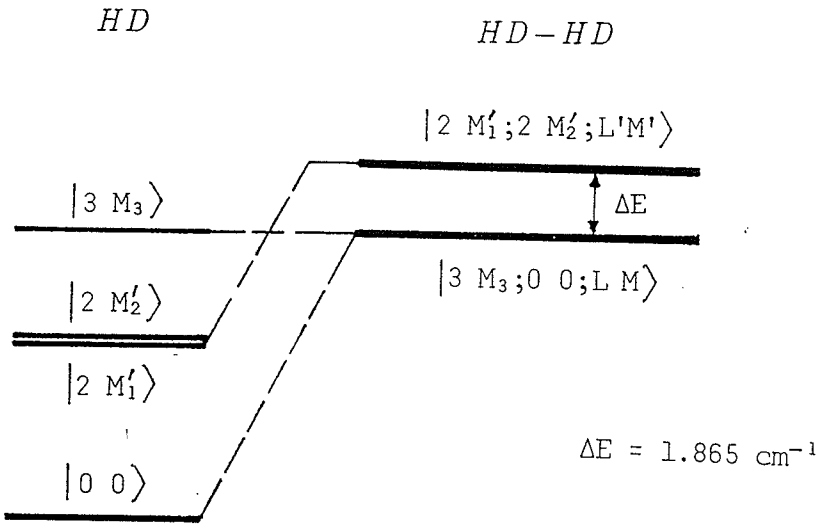

Figure 2.3: Near-resonance rotational-level mixing.

in the $HD - HD$ system are significantly affected by this mixing. The calculated results showed that the additional contribution from this mixing was so important that it even caused a sign change in the interference parameter for $R(2)$ with respect to the calculated value in which this mixing was ignored. The calculated contributions to the interference parameter of $R(2)$ and $R(3)$ for $HD - HD$ are listed in Table 5.4 along with other calculations for discussion.

2.5 New Development in the Theory

Very recently, B. Gao, G. C. Tabisz, M. Trippenbach and J. Cooper developed a new approach resulting in a new theory to describe the intracollisional interference for HD [64]. In their derivation the fundamental approximation was the impact binary collision approximation. A master equation formulation in the

Liouville space was used. The density matrix of the gas, in which the collisions take place, was constructed first, and then the evolution of the density matrix in the presence of the incident radiation was described. Finally the absorption and stimulated emission of spectrum was obtained by solving the master equation. In this approach, the allowed and collision-induced transitions were treated in a consistent manner. The expression for the absorption coefficient contains all the contributions as were discussed in this chapter including the effects due to rotational-level $J-$ and $m-$mixing. Consideration of this new theory in detail is beyond the scope of the present thesis, but it will be used as a point of discussion in chapter 6.

Chapter 3

EXPERIMENT

The experiments in this research were typical of far infrared absorption spectroscopy. The information collected concerned the slight changes in the pure rotational spectra of HD and of its mixtures under varying physical conditions. A high resolution Fourier transform spectrometer constituted the main equipment. This chapter begins with an overview of the experimental system. It is followed by detailed descriptions of the spectrometer, absorption sample cell, detector, gas handling system and the operation of the experimental system.

3.1 An Overview of the Experimental System

A schematic overview of the experimental system is illustrated in Figure 3.1. The infrared radiation from a Globar source (G) was first collimated by a parabolic mirror M1 before entering the Michelson interfereometer. This incident beam was then split about equally in intensity by a beamsplitter producing a partially reflected beam and a partially transmitted beam. The *reflected* beam was subsequently reflected from the fixed mirror, M2, while the *transmitted* beam

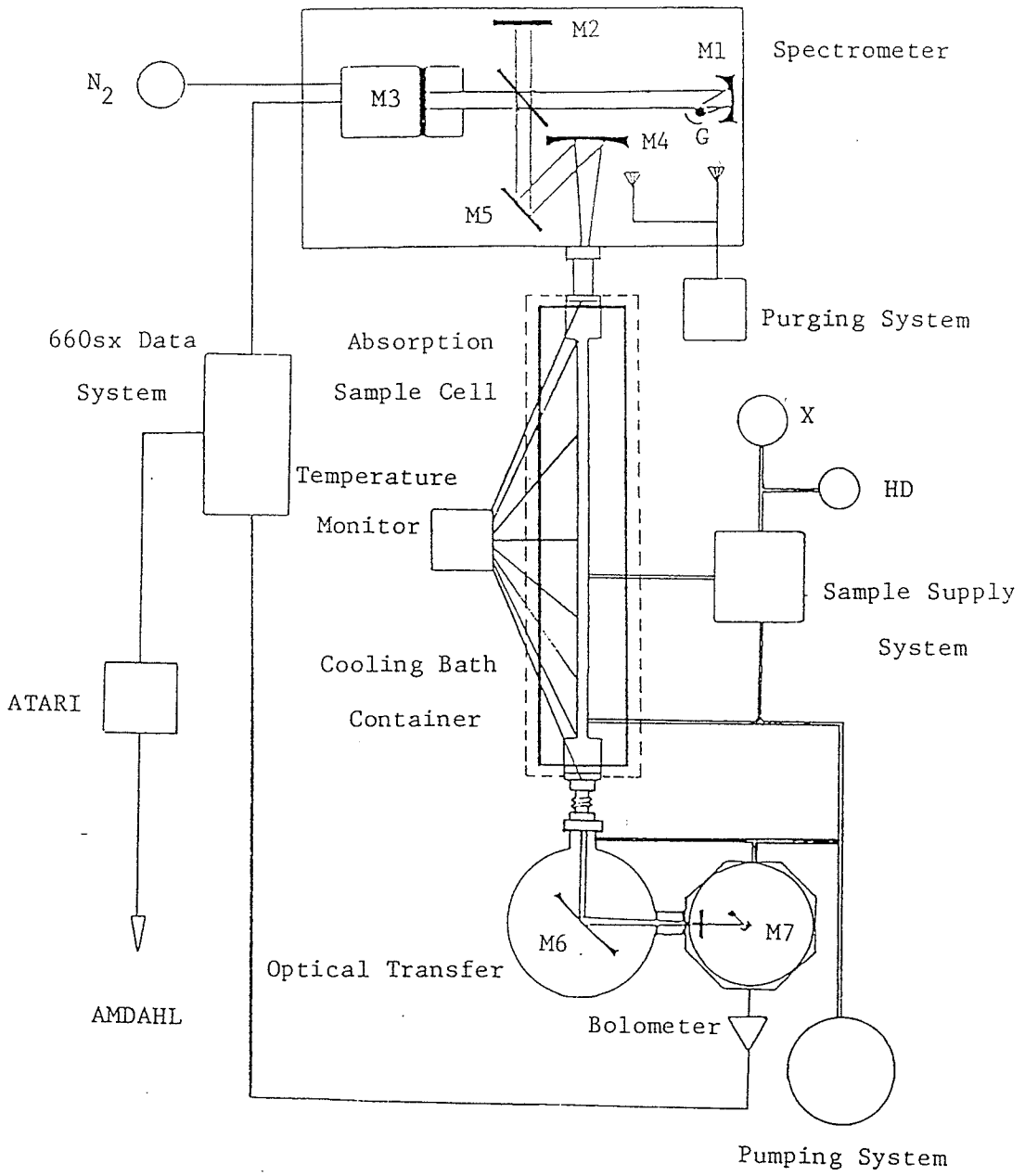

Figure 3.1: Overview of the experiment aspects

was reflected from the moving mirror, M3. The beams were recombined and then again split at the beamsplitter, with one weak beam returning to the source and the other proceeding to a flat mirror M5. This latter beam was collimated again by a spherical mirror M4, and focused on the entrance window of the absorption sample cell. The absorption sample cell was mounted inside an external container to allow its immersion in a cooling bath for operation at low temperature. The opposite end of the absorption sample cell was connected to an optical transfer system which consisted of a cylindrical vacuum chamber, containing a spherical mirror M6. M6 collected the output beam and focused it on the entrance window of the bolometer. Finally, a mirror, M7, inside the bolometer, focused the beam on to the germanium crystal.

The preamplified signal from the detector was sent to the data system and stored on the hard disk for later analysis.

An ATARI MEGA ST2 computer served as an intermediary station to accept the data from the NICOLET data system after the first step of data analysis and then to transfer these data to the main frame computer afterwards with KERMIT software support.

3.2 Spectrometer

The spectrometer used in this experiment was a commercial NICOLET series 7000 Fourier Transform Infrared Spectrometer (Nic-7199 FT-IR System). It consists of a computer controlled scanning Michelson interfereometer system (Nic-7100 Interferometer) along with a data system. The Nic-1180 data system

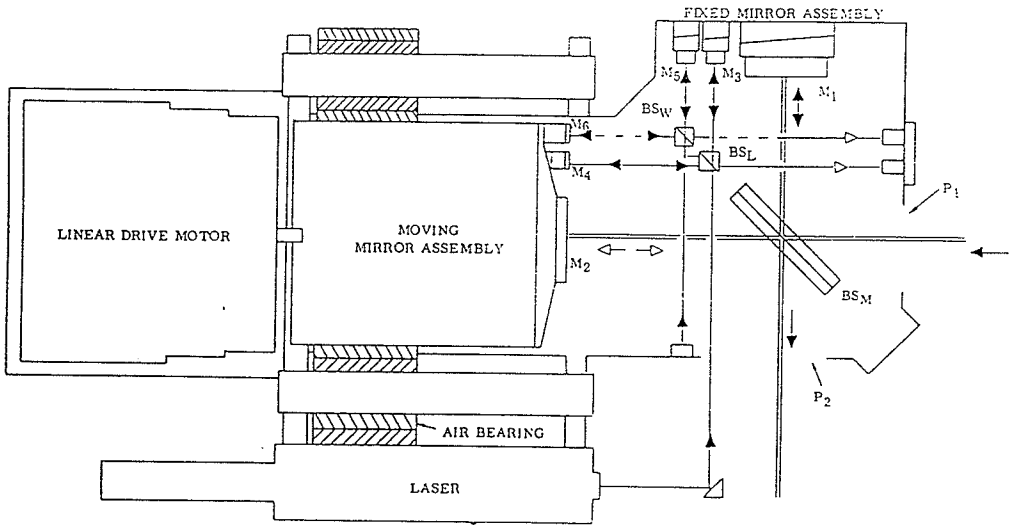

Figure 3.2: interfereometer

was used for the experiments performed prior to 1990. Subsequently in 1990, it was replaced by a new Nic-660sx computer system.

The Michelson interfereometer actually consists of three different interfereometers: a He-Ne laser reference interfereometer, a white light interferometer and an infrared interfereometer, as shown in Figure 3.2.

All moving mirrors of these three interfereometers were mounted on a common moving mirror assembly, and all fixed mirrors were mounted on a common fixed mirror assembly.

Since the Fourier transform of a delta function is a *Sine* function, the interfereogram of a single frequency beam from the He-Ne laser is a *Sine* wave with a typical interval of 0.3165 μ between its zero crossings. These zero crossings were

used to trigger the sampling logic that initiates the analog to digital conversion cycle. An absolute frequency accuracy of better than 0.01 cm^{-1} was thus claimed by the manufacturer. However in practice a fine calibration is still needed for an accurate determination of frequency for spectra as we will discuss later. In addition to specifying the sampling points, the laser interfereometer signal was used to measure the moving mirror velocity to an accuracy of 0.125%.

The white light interfereometer, on the other hand, has a broad band visible source. Therefore the interfereogram is the superposition of an infinitely large number of different *Sine* waves and consequently general constructive interference occurs only for a zero path difference between the distances of the beamsplitter to the moving and fixed mirror. The fixed mirror was factory adjusted so that the ZPD (point of zero path difference) of the white light interfereogram occured just 0.3 mm earlier than the ZPD of the main IR interfereometer. Moreover the control system was designed to ensure that on each scan, the peak of the white light signal occured just prior to the zero crossing of the laser reference signal. Thus, the unique zero crossing of white light interfereometer on each scan was chosen as a starting point of data taking by the main IR interfereometer.

The optical aperture of the main IR interfereometer allowed a full, clear 2-inch diameter incident beam. The total optical retardation length was 16 cm, yielding a theoretical highest resolution of 0.06 cm^{-1} as stated by the manufacturer. The moving mirror assembly was mounted on dual air bearings to prevent rotation and to reduce the friction to ensure mechanical stability.

The infrared light source was a water cooled globar (a silicon carbide rod).

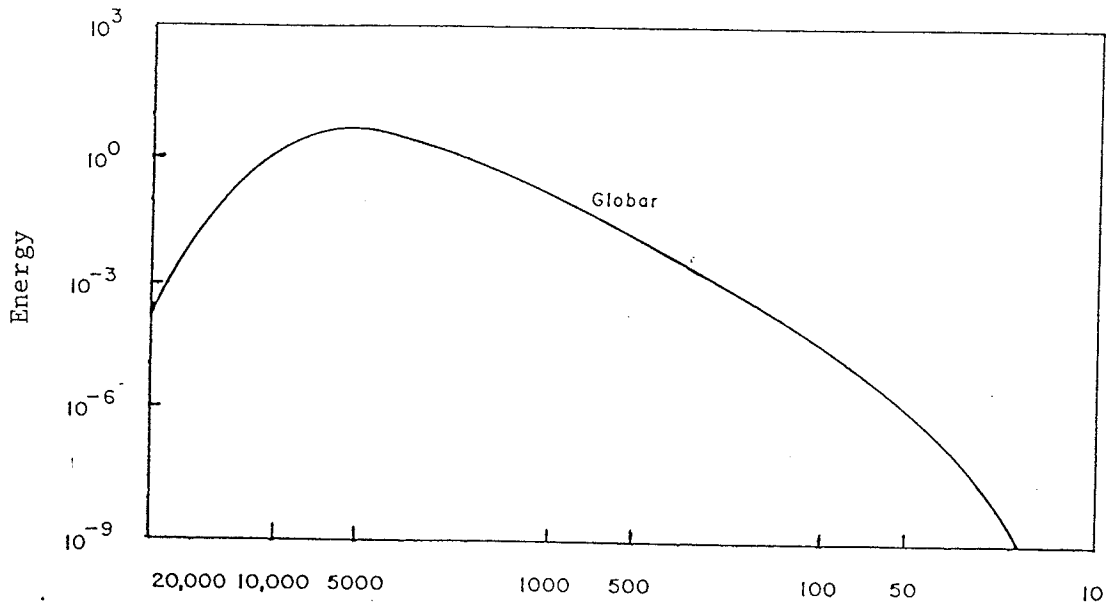

Figure 3.3: The radiation curve of the Globar

The radiation curve of the glowbar is shown in Figure 3.3 [86].

The beam splitter selected was capable of efficiently dividing the incident beam into two approximately equal intensity beams in the frequency region of interest. A 6.25 μ thick Mylar film has a good efficiency in the range of 70-390 cm^{-1} and thus could serve as a beam splitter in all the experiments. The efficiency curve is shown in Figure 3.4 [87].

Theoretically, the Fourier transform of the interfereogram is given by [88]:

$$I(\nu) = \int_{-\infty}^{+\infty} I(t) e^{i2\pi\nu t} dt, \tag{3.1}$$

where I(ν) is a Fourier transformed spectrum, I(t) is an interfereogram and t is

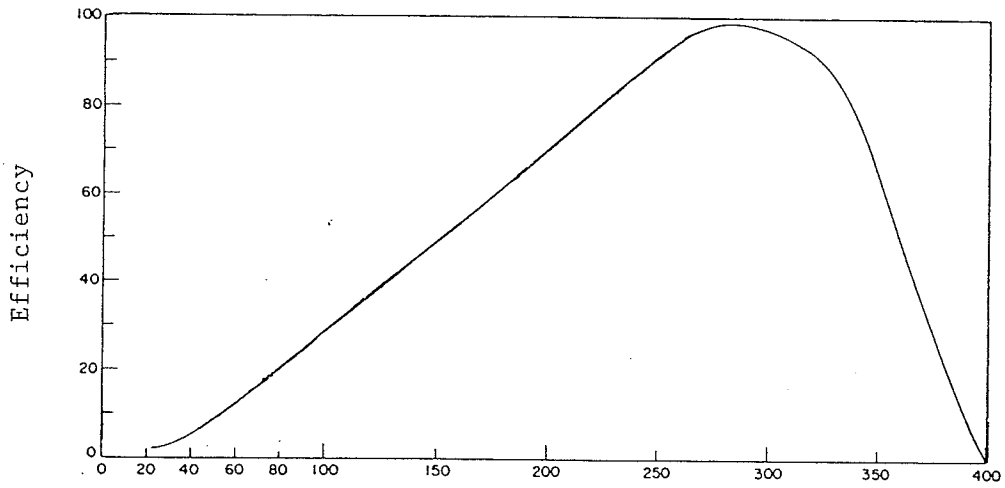

Figure 3.4: The efficiency curve of the beam splitter

time. In practice, only a limited number of data points are taken in the measurement. As a result the spectrum obtained is the Fourier transform of a convolution of the interfereogram with a box function:

$$I(\nu) = \int_{-\infty}^{+\infty} \int_{-\infty}^{+\infty} I(t) H(t' - t) e^{i2\pi\nu t'} dt dt', \tag{3.2}$$

where

$$H(t' - t) = \begin{cases} 1 & \text{if } |t' - t| \leq t_0 \\ 0 & \text{otherwise.} \end{cases} \tag{3.3}$$

This effect was minimized by a technique called apodization which improves the lineshape at the expense of lower resolution [89]. A modified trigonometric function, called the Happ-Genzel function [86], suggested by the manufacturer, was

applied for apodization in the experiment:

$$F(H-G) = 0.54 + 0.46cos\{[|N_i - N_{ZPD}|/(NDP - N_{ZPD})]\pi/2\}, \qquad (3.4)$$

where N_i is the displacement of i th point from the start of the scan, N_{ZPD} is the location of the ZPD data point and NDP is the total number of data points.

As a result of the refractive index of the optical elements, as well as the fact that ZPD point does not correspond to the first point in the spectrum, a phase error in the Fourier transform is inevitable [90][91][92]. To correct the phase error, a short double-sided interfereogram was taken from the measured interfereogram to be used to calculate a phase array. As set by the manufacturer, this spectrometer used sixty points around ZPD for phase array calculations [86].

The new Nic-660sx data system includes 1.28 Megabytes of RAM memory, a storage module device (SMD) hard-disk interface and two 640 Kbyte 3.5 inch microfloppy diskette drives [93]. The 660 high-resolution color display monitor was used with the data system for fast spectral display and data assessment. The standard Nic-660sx comes equipped with four software programmable RS-232 ports and two high speed differential RS-422 ports for fast data transfer and communication with other computers. The data system controls the spectrometer using a series of data-collection parameters and performs data manipulation with its FT-IR command language.

3.3 Absorption Sample Cell

The absorption sample cell was constructed by Nelson and Tabisz in 1983 [47] following the 1978 design of Horne and Birnbaum [94]. It consists of two parts: a 1 m long stainless steel tube with 1.3 *cm* inside diameter and 1.9 *cm* outside diameter which is a sample cell proper and a 92 *cm* long, 16 *cm* wide and 23 *cm* high stainless steel case which acts as a cooling bath container.

There are two flanges on each end of the sample cell. Five circular concentric V grooves about 0.5 mm deep were cut into each flange and six equally spaced bolts clamped the two flanges together. A 6.3 *cm* diameter high density polyethylene disk was compressed between two flanges and served as a window. When the six bolts are tightened, the polyethylene flows into the circular grooves and effectively forms a series of O-ring seals. The inside of the sample cell was polished to make the tube behave as a light pipe in order to enhance the signal. The sample cell demonstrated an excellent low leakage rate over 36 hours with both 3.2 mm and 4.8 mm thick windows at 560 psi. At 760 psi, this hold time dropped to 18 hours with the same windows.

The cooling bath container, designed by Ulivi in 1987 [5], allows over 92% of the sample cell to be completely immersed in the coolant. The temperature stability over the remaining 3.8 *cm* from each end of the windows was achieved through thermal conduction by the cell walls and the thick high pressure flanges. On the external side of input window, there was a stainless steel connecting tube between the spectrometer chamber and the sample cell. One end of this connector was welded on the outside flange, and the other end was attached to

the wall of the interfereometer chamber with a 1.5 mm thick polyethylene sheet as its vacuum window. On the output window side of the sample cell, there was a similar connector between the cell and an optical transfer system. Both of the connector regions were under vacuum during operation. This is crucially important at low temperature to prevent condensation or ice formation on the windows of the sample cell.

The cooling bath container, as well as the two connectors were covered with 2-3 inch-thick foam layer to achieve good thermal isolation. Eight thermocouple (TC) detectors were uniformly distributed along the length of the sample cell to monitor the temperature gradient. Five of them were soldered on to the wall of the cell and coated with Multi-purpose Foam to avoid direct contact with the coolant. Three of them were removable. The high thermal conductivity oxygen-free copper sensors of the thermocouples were held in direct mechanical contact with the cell wall by means of teflon clamps. No temperature gradient was found within the container both at 77 K and 195 K. In the 3.8 *cm* end region of the sample cell, a 8-16 degree difference was found during the experiments at 77 K. At 195 K, this temperature gradient was down to 7-10 degree. Thus, the assurance can be given that at the worst case, the error in the density determination of the sample gas caused by the incomplete immersion is less than 1%.

The coolant for the experiment at 77 K was liquid nitrogen. A 100 litre dewar was used as a coolant supply vessel and connected to the cooling bath container with a rubber transfer tube. A compressed nitrogen gas cylinder was connected to the supply dewar via a polyethylene tube to provide the necessary

pressure to transfer liquid nitrogen into the bath container to maintain the coolant level. At 195 K, the coolant was a mixture of ethyl alcohol and dry ice. Approximately 7.5 kg of dry ice were added each day to keep the coolant stable at the desired temperature.

3.4 Detector

The detector used in the experiment was a liquid helium cooled FTS Germanium Bolometer System manufactured by Infrared Laboratories, Inc.

This system consists of a germanium bolometer with an effective area of 9 mm^2, a model HD-3 dewar, a model LN-6 preamplifer and two far-infrared cut-off filters passing the wavenumber regions 10-375 cm^{-1} and 10-100 cm^{-1} respectively. The 10-375 cm^{-1} filter was used in all experiments in this study. It was a 0.75 inch diameter wedged Sapphire coated with 4-8 μ diamond powder and ZnO powder layer to cut off the near-infrared radiation. The outer vacuum window was wedged polyethylene, coated on the inner face with a 4-8 micron diamond layer. As illustrated in Figure 3.5 [95], the spectral response was dominated by the cut-off filter.

The model HD-3 dewar has two containers: one for liquid nitrogen and the other for liquid helium. Care has to be taken to top up the liquid nitrogen before each run. A 33 hours hold time with a liquid helium fill was achieved under continuous operation in the 1990 experiments.

The entire detector system was mounted on a lab jack fastened to the optical table which provided stability and fine adjustment capability.

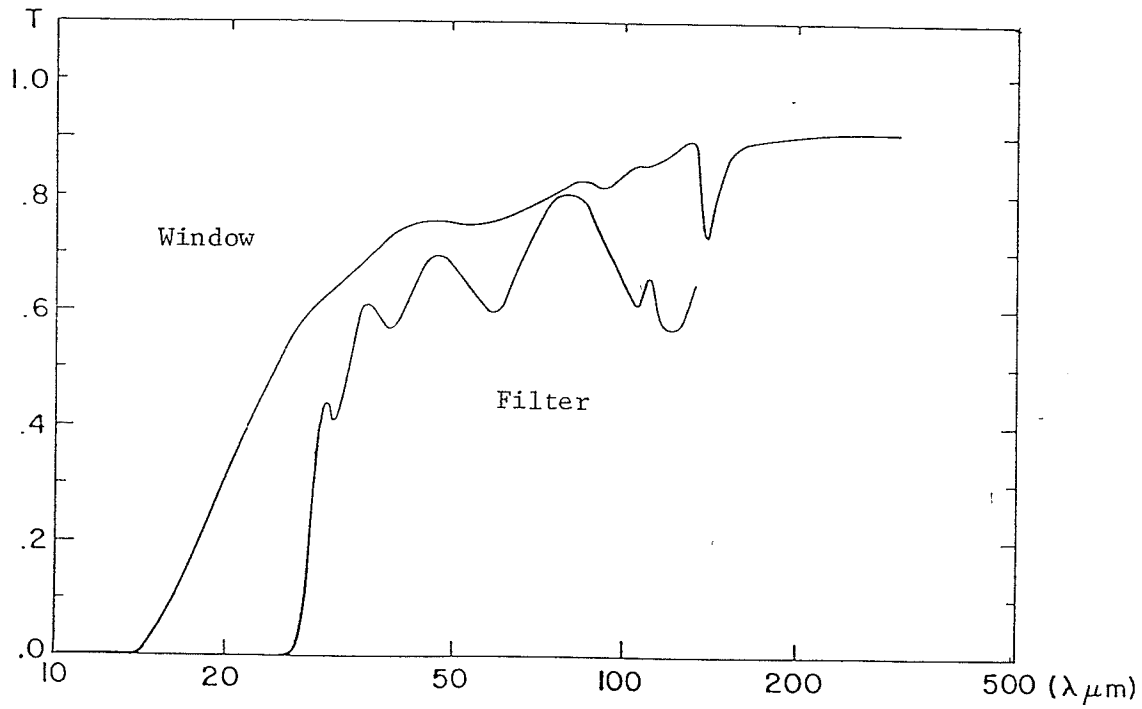

Figure 3.5: The response curves of the filter and window

3.5 Gas Handling System

The gas handling system includes a vacuum system, a nitrogen purge system and a sample supply system, as shown in Figure 3.6.

A GDA-1 rotary vacuum pump and a water cooled 80 cc fluid charge diffusion pump with a liquid nitrogen trap were the main components of the vacuum system. The entire vacuum system was made from stainless steel tube or copper tube, soldered or coupled with high vacuum elements. The vacuum condition was monitored with two CP25-EK penning gauges (PG) and five thermocouple gauges (TC). The vacuum within the sample cell was usually on the order of 10^{-4} torr when the background was taken. This vacuum was monitored by a penning

gauge connected directly to the sample cell.

The effect of water vapour, which has very strong absorption in the far-infrared, was essentially eliminated in the sample cell, optical transfer system and two connectors because of the vacuum. However, since the interfereometer chamber itself is not evacuable, the introduction of dry nitrogen into it is neccessary to reduce the concentration of water vapour and therefore to reduce the *water noise* in the spectra. Two 50 lb capacity nitrogen dewars were used to provide dry nitrogen to the chamber through a purge network and controlled by a relay switch. The gas flow was controlled by a suitable voltage supplied to a heater inside the dewar, and was monitored by a tube flowmeter (FM). Two filters were used at the entrance of the chamber to prevent dust contamination. In addition to the purge system, compressed nitrogen gas for the air bearings of the spectrometer was also introduced into the chamber to supplement the purging procedure.

The sample supply system basically consisted of a manifold with five control valves and a pressure gauge system as shown in Figure 3.6. There are two cold traps (CT) along the input route from sample cylinder to the manifold, and another one in the route from the manifold to the sample cell. Liquid nitrogen or a mixture of ethyl alcohol and dry ice were the coolants used for these cold traps in order to freeze the water vapour in the sample gas and also to pre-cool the sample gas for low temperature experiments. When the pressure of the sample gas in the experiment was below 25000 torr, the pressure was measured by an MKS Baratron 220CA absolute pressure transducer with a PDR-D-1 power supply digital readout. At higher pressures, a Heise gauge (0-1500 psi) was used.

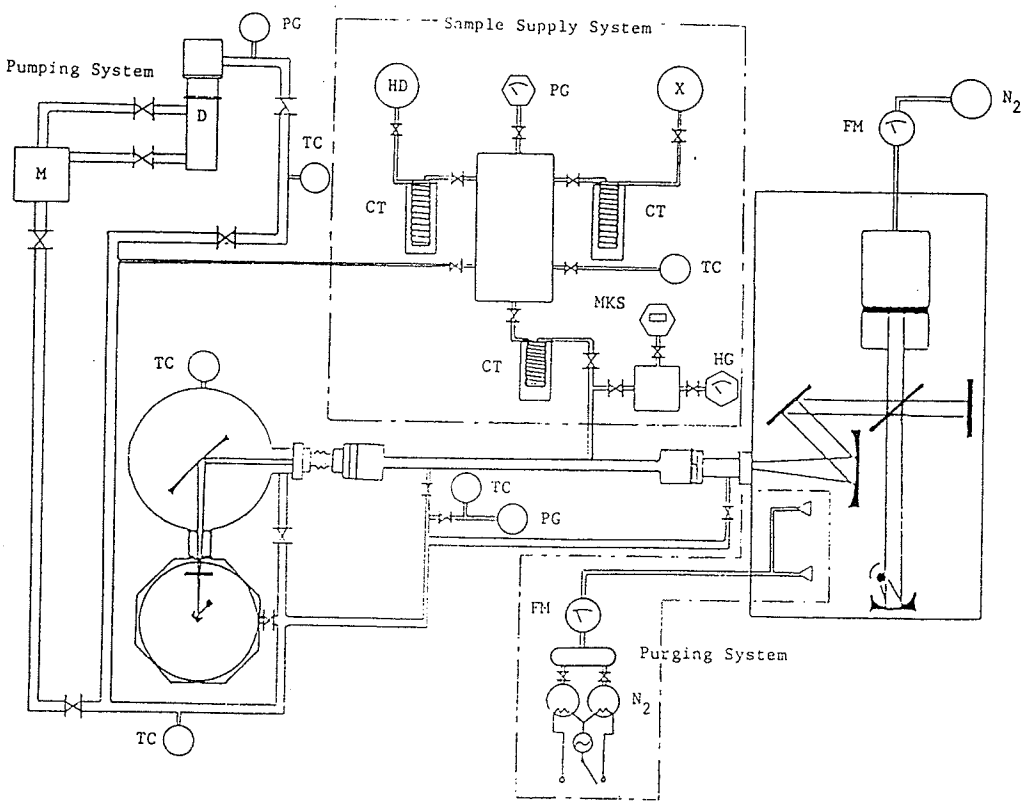

Figure 3.6: The gas handling system

The accuracy of MKS system was ± 0.01% of full scale ± 1 count, while for the Heise gauge (HG) it was 0.1% of full scale (FS). Both of these instruments were calibrated by the manufacturers.

For the sample gases used in this study, HD was obtained from MSD Isotopes with a purity of 98%, and the other gases from Matheson, all with a purity above 99.99%.

3.6 Operation

To obtain a good spectrum, the signal to noise ratio (SNR) must be as high as possible. Obviously the optical path alignment is vitally important to the experiment.

A TGS detector was used for pre-alignment of the path from the light source to the output window of the sample cell with the assistance of a 0.5 mw He-Ne laser. All polyethylene windows were removed at this first step of alignment. The peak to peak voltage (V_{pp}) of the interfereogram was monitored by an oscilloscope taking the signal from the IR port and the trigger from the output of the TKDA (taking data) port of the spectrometer control panel. Fine adjustments were made to ensure the sample cell was horizontal and the signal received at the output window was a maximum. Then the TGS detector was replaced by the optical transfer system connected with the bolometer. The signal should be monitored before the windows were installed. The optimum condition was achieved when V_{pp} of the signal was maximized by performing a fine and careful adjustment to the optical transfer system and lab jack, i.e. the bolometer position.

The optical path alignment must be completed at least 24 hours before the experiment begins, because a minimum of 24 hours is neccessary to evacuate the operating system, to purge the spectrometer chamber and for the infrared light source to reach thermal equilibrium.

For the low temperature experiments, the cooling process was begun when the vacuum in the sample cell and the connection components was better than 10^{-3} torr. Repeated tightening of the couplings to the sample flanges was continued during the cooling process which took about 2.5 hours for 77 K and 2 hours for 195 K. All connectors to the sample cell were covered with thermal insulating materials before the end of cooling process.

For each sample gas, the experiment started with a background measurement, then a small amount of pure HD (about 3 amagat for the 77 K experiment, 3−5 amagat for 195 K and 7 amagat for 296 K) was introduced and the spectrum was measured as a zero perturber density value. It was followed by a series of measurements with a series of perturbers at increasing densities and completed with another background measurement. Thus, the noise, especially the water noise contribution from variations in the environment, was recorded. This is important in the data analysis, as we will discuss in the next chapter

There are two parameters which affect the amplitude of the interfereogram: the electronic gain GAN and the scan velocity of the mirror VEL. Obviously one should use as low a GAN and as high a VEL as possible to prevent electronic noise and to shorten the measurement time. In the 1987 experiments, GAN=16 and VEL=26 (V=0.8988 cm/sec) were used at 77 K to achieve a V_{pp} value of 5

V for the background, and at 195 K, GAN=16 VEL=20 (V=0.5611 cm/sec) gave V_{pp}=8.7 V. In the 1990 experiments, GAN=16 and VEL=26 were chosen for both 195 K and 296 K. The V_{pp} was typically 13.7 V at 195 K and 10.7 V at 296 K during the experiment. To reduce the random noise, 400 scans were taken for signal averaging at each density in all cases. About 3 hours and 50 minutes were needed for each run when VEL=20, while when VEL=26 this period was reduced to 2 hours and 20 minutes.

The spectrometer was controlled by a macro program with a set of data collection parameters. These parameters were selected based on the high resolution requirements as well as on the experimental conditions. The control program used in the experiments is listed in the Appendix.

Chapter 4

DATA ANALYSIS

As was mentioned in the previous chapters, the information of interest is the variation in the pure rotational spectra of HD, namely its intensity and its line shape, in the presence of different perturber molecules under different physical conditions. The experiments completed in this study are listed in Table 4.1.

The data analysis began with a Fourier transform of the collected raw data to obtain absorption spectra. Following a baseline correction, the individual pure rotational absorption spectral lines of HD were obtained. These data were transfered to the main frame AMDAHL computer via an ATARI computer. A suitable lineshape was chosen to fit these spectra data to obtain fitted parameters related to the intensity and line shape. After a density determination, a series of calculations followed leading, finally, to the magnitude of the matrix element of the allowed dipole moment of HD and the line shape parameters for individual rotational lines. The details of the data analysis will be given in the following sections in the same order that each step occurs in the analysis. The experimental results will be presented at the end of this chapter.

Table 4.1: Experiments completed

Temperature (K)	Sample			
77	$HD-HD$	$HD-H_2$	$HD-He$	$HD-N_2$
195	$HD-HD$	$HD-H_2$	$HD-He$	$HD-Ne$
	$HD-AR$	$HD-Kr$	$HD-N_2$	
296	$HD-H_2$	$HD-Kr$	$HD-N_2$	

4.1 Absorbance Spectra

The raw data recorded by the spectrometer were the interfereograms corresponding to an unapodized theoretical resolution of 0.06 cm^{-1}. Figure 4.1.A shows a typical interfereogram for the background taken at 195 K. The corresponding transmittance spectra as illustrated in Figure 4.1.B was obtained by using the Fast Fourier Transform (FFT) [96] procedure supplied by NICOLET.

If $I_0(\omega)$ is the background intensity and $I(\omega)$ is the sample intensity, then the absorbance is given by

$$A(\omega) = -log_{10}[I(\omega)/I_0(\omega)] \tag{4.1}$$

or

$$A(\omega) = log_{10}I_0(\omega) - log_{10}I(\omega). \tag{4.2}$$

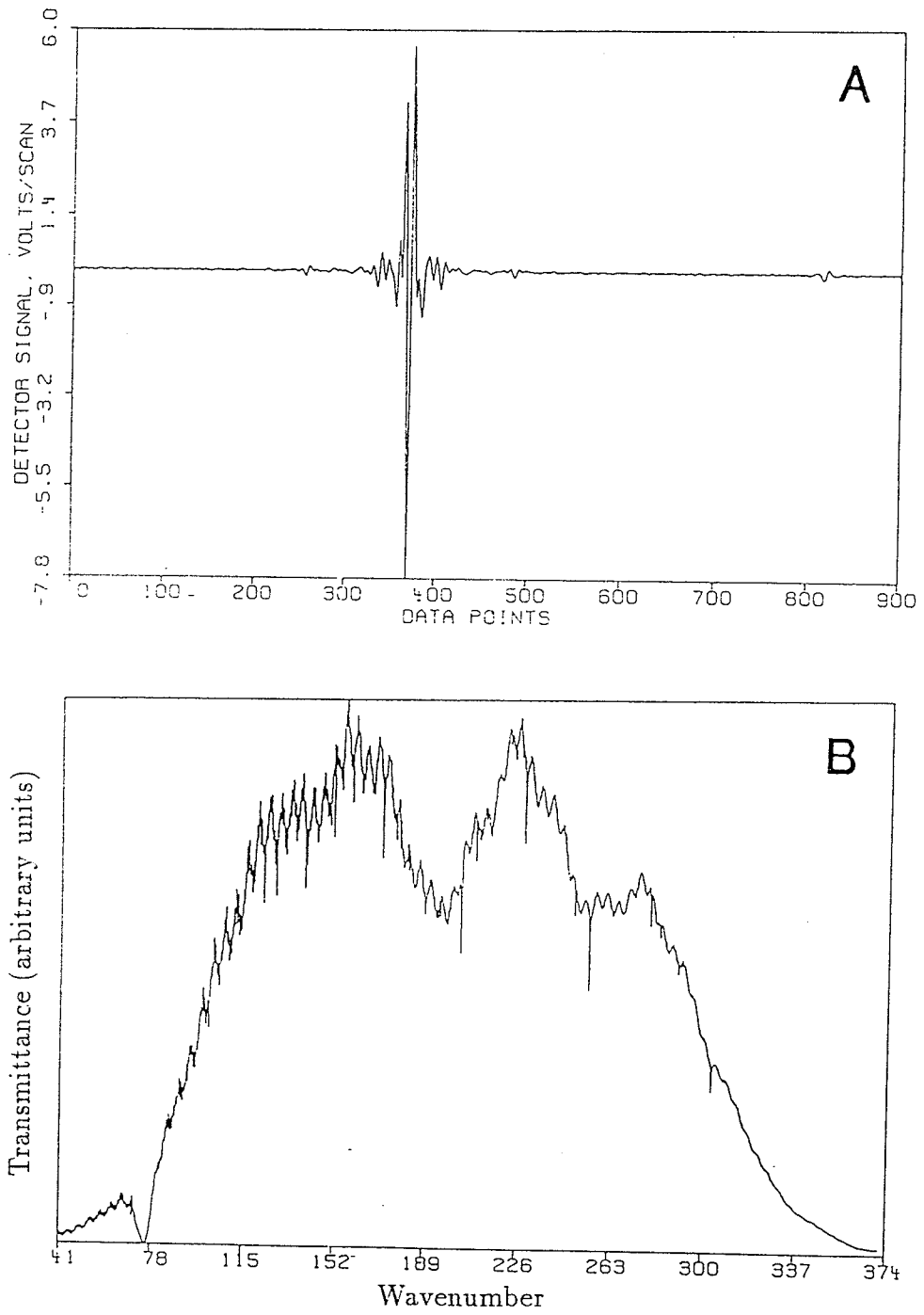

Figure 4.1: Interferogram (A) and its corresponding transmittance spectra (B)

Obviously, if

$$log_{10}I(\omega) = log_{10}I_{sample}(\omega) + log_{10}I_0(\omega), \tag{4.3}$$

then

$$A(\omega) = -log_{10}I_{sample}(\omega), \tag{4.4}$$

as expected in the ideal situation. However, as we mentioned earlier, the presence of water vapour in the optical path, especially through the variation of its concentration, always results in some water absorption lines, more or less, in $A(\omega)$ of the sample and the background. These lines effectively introduce noise into the desired spectrum. To solve this problem, more than one background at the same temperature and under the same experimental conditions was recorded. These backgrounds usually contain water lines with different intensities. Some are *clean*, i.e. contain low intensity water lines, and some are relatively *noisy*, i.e. show strong water absorption. Among the backgrounds taken at the same temperature, the *cleanest* one was taken as a *background* file, and the one with the greatest number of water lines was taken as a *reference* file. The reference file was then adjusted by an appropriate factor determined by when the intensity of the strong characteristic water lines (170 cm^{-1} and 202 cm^{-1}) in the sample absorbance exactly matched those in the reference absorbance. Finally the water noise in the sample absorbance was removed by subtraction. The underlying assumption in this procedure is that the water lines have the same width and frequency in all spectra. This is a good assumption as the water concentration is low and all broadening and frequency shifts occur through interaction of the

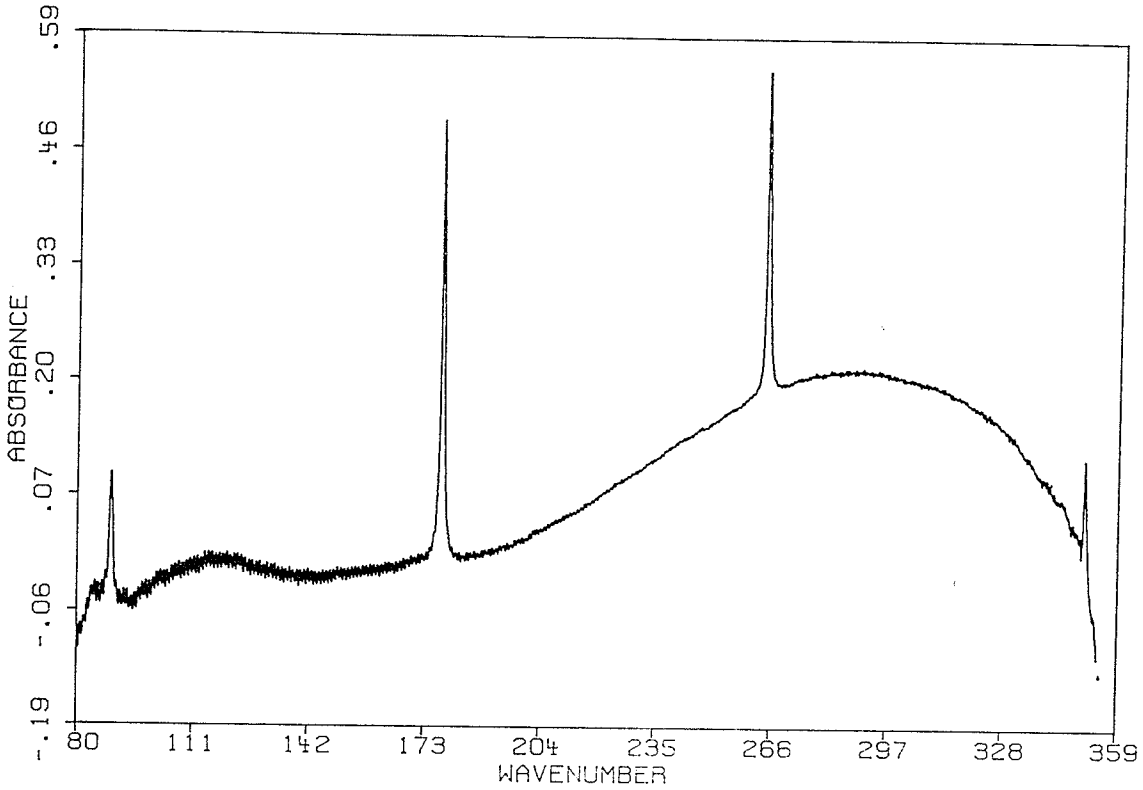

Figure 4.2: Absorbance of HD at 50 amagat 195 K

water molecules with foreign perturbers and not with each other.

For this study, only the pure rotational transitions R(0), R(1), R(2) and R(3) could be recorded. They are sharp lines located upon the broad collision-induced background, as illustrated in Figure 4.2. The continuous background around the individual rotational lines (about 5 cm^{-1} on each side) was removed by the Base Line Correction (BLC) routine supplied by NICOLET [93]. The basic idea of BLC is to fit the base line of individual R(J) lines by a quadratic function and then subtract the fitted base line numerically. This is a first order base line correction. A more precise correction is still necessary as we will discuss later.

The spectral data containing R(J) lines with their approximately 5 cm^{-1} wing part on both sides were converted to ASCII code by a pre-edited BASIC

program and then saved in individual data files. These data were first transfered to an ATARI MEGA ST2 using KERMIT software provided by NICOLET, and then to the AMDAHL main frame for further analysis.

4.2 Profile Fitting Process

As described in the previous chapters, the lineshape of the sharp rotational line R(J) is considered to be the sum of a Lorentzian profile and a dispersion part. The following equation was used as a basic equation to fit the absorbance spectra of each R(J) line at each density:

$$\frac{A(\omega)}{\omega} = \frac{D_0}{(\gamma/2)^2 + (\omega - \omega_0)^2} + \frac{2(\omega - \omega_0)E_0}{(\gamma/2)^2 + (\omega - \omega_0)^2}. \tag{4.5}$$

This is similar to the profile equation introduced by Herman, Tipping and Poll [46]:

$$\frac{A(\omega)}{\omega} = \frac{D\gamma\pi}{2}[(1 - q^{-2})\frac{\gamma/2\pi}{(\gamma/2)^2 + (\omega - \omega_0)^2} + q^{-1}\frac{2(\omega - \omega_0)/\pi}{(\gamma/2)^2 + (\omega - \omega_0)^2}]. \tag{4.6}$$

To improve the base line correction in the NICOLET system, a straight line $A\omega + BK$ was added into the fitting process. Therefore there were a total of six adjustable parameters taken in this procedure; base line correction factors A and BK, the full width at half intensity (FWHM) γ, the shifted line peak frequency ω_0, the intensity parameter D_0 and the asymmetry parameter E_0.

A SAS program employing Marquardt algorithms was used for the above fitting, and is presented in the Appendix.

Occasionally there was an oscillatory type noise, or *Sine* noise, that appeared in the spectra. This was caused by the interference from internal reflections from the parallel surfaces of the window, and the interference fringes present in the sample and background spectra did not cancel each other out [60][86]. However, a *Sine* function was found adequate to represent this type of noise. Thus, for the spectra with such noise, the base line (with the peak region removed) was first fitted by a *Sine* function plus a straight line:

$$Base = A\omega + BK + DSin[B + 2\pi(\omega - \omega_0)/C], \tag{4.7}$$

where BK, A, B, C and D are adjustable parameters. Then the noise was subtracted numerically from the spectra before the profile fitting procedure. Figure 4.3 and Figure 4.4 demontrate the effectiveness of this approach. A shows spectrum with *Sine* noise before correction, B is the fitted *Sine* wave and corrected base line, C shows the corrected spectrum with the fitted curve given by Equation 4.5

4.3 Density

The unit of density used in this study is the *amagat* defined as follows,

$$1 \ \ amagat = 2.68675 \times 10^{19} \ \ molecules/cm^3 \tag{4.8}$$

at NTP (0^0C temperature and 1 atm pressure).

The raw pressure data for HD and its mixtures were recorded by an MKS

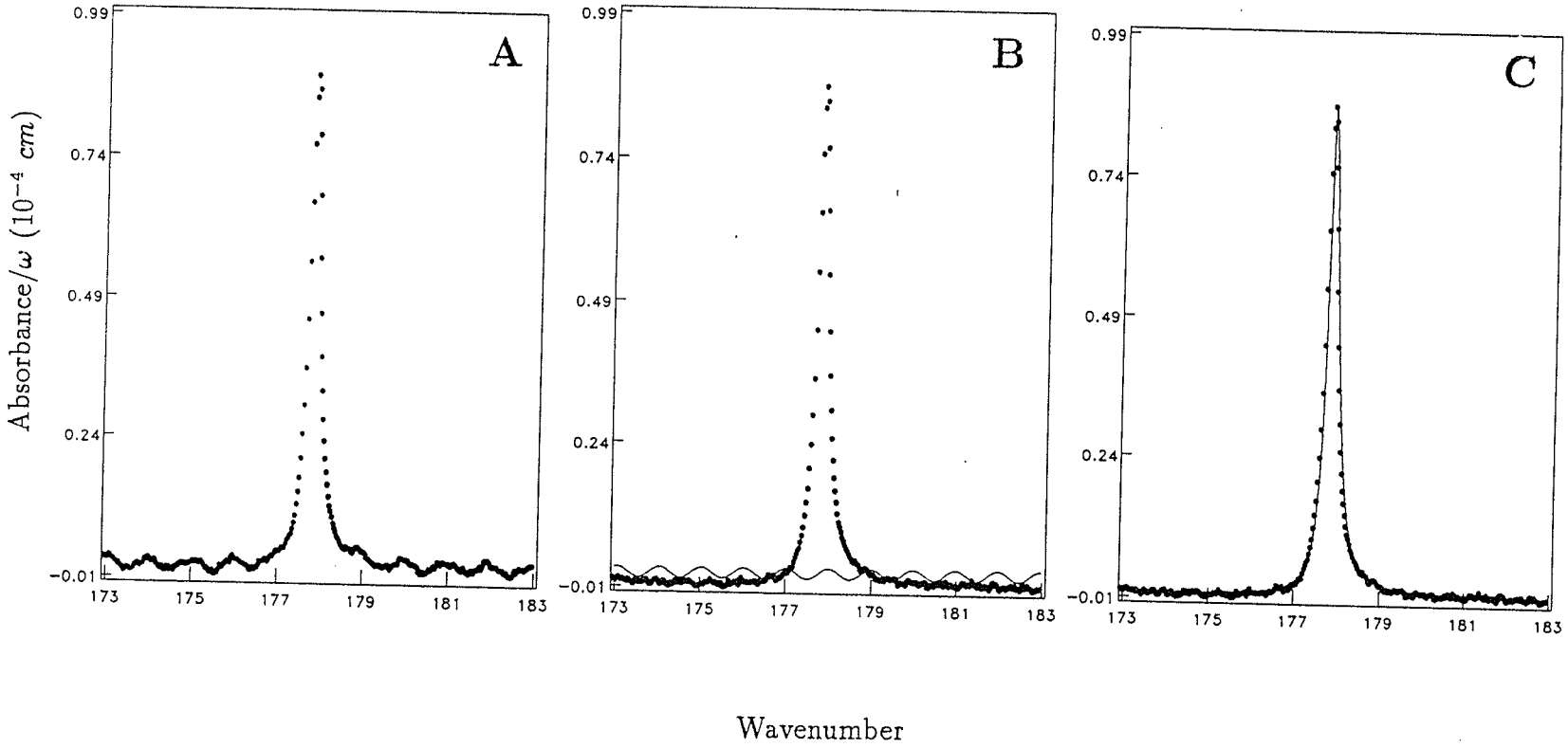

Figure 4.3: Spectrum of R(1) $HD - Ne$ at 195 K. The density of HD is 4.98 amagat and that of Ne is 12.8 amagat. A: uncorrected data; B: fitted base curve and corrected base line; C: corrected spectrum and the fitted curve (Equation 4.5).

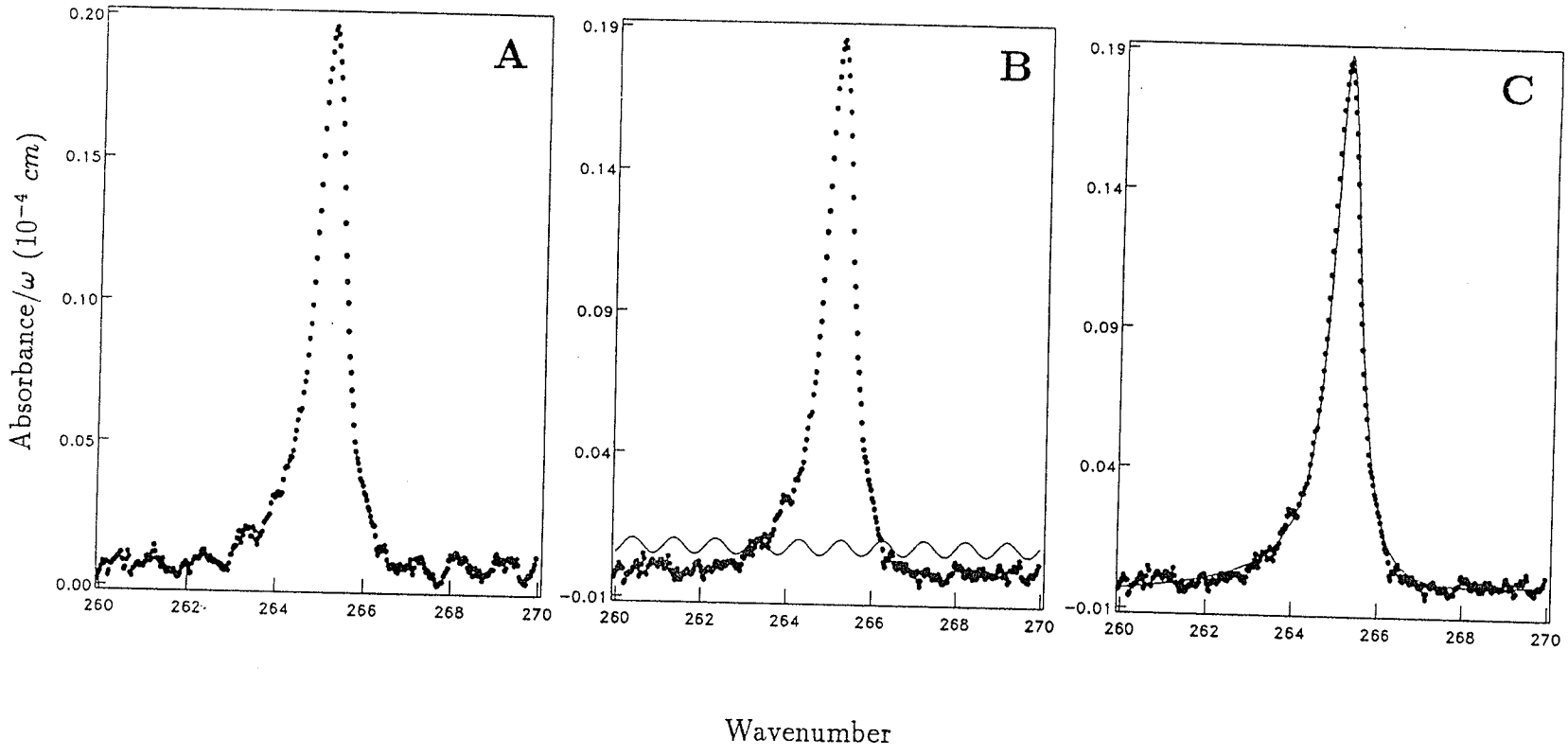

Figure 4.4: Spectrum of R(2) $HD - Ar$ at 195 K. The density of HD is 4.98 amagat and that of Ar is 37.7 amagat. A: uncorrected data; B: fitted base curve and corrected base line; C: corrected spectrum and the fitted curve (Equation 4.5).

electronic pressure transducer and a Heise pressure gauge simultaneously in the pressure range up to 25000 torr. These data were used to assess the agreement between the two gauges. Since the highest pressure used in this study was approximately 700 psi, it was safe to calibrate the readings on the Heise gauge using the MKS transducer to achieve maximun accuracy.

A virial expansion and the second virial coefficient were used to calculate the amagat density from the pressure data:

$$Density(amagat) = \frac{22414.0}{(RT/P) + B(T)} \quad , \tag{4.9}$$

where R is universal gas constant in $atmcm^3/moleK$ and B is the second interaction virial coefficient in $cm^3/mole$. For the density of mixtures of HD with foreign gases, B was evaluated by the following equation [97]:

$$B(T) = f_1^2 B_{11}(T) + 2 f_1 f_2 B_{12}(T) + f_2^2 B_{22}(T), \tag{4.10}$$

where $B_{11}(T)$ is the virial coefficient of HD, $B_{22}(T)$ is that of the foreign gas and $B_{12}(T)$ is the interaction virial coefficient of HD with the foreign gas. In the above equation f_1 and f_2 are the fractional concentrations of the two gases. $B(T)$ usually converged within a few iterations of a FORTRAN program with the initial value of f_1 and f_2 taken from the pressure data. Details of the computer program are presented in the Appendix.

The virial coefficients at different temperatures were mostly obtained from J. H. Dymond and E. B. Smith [97]. $B_{12}(T)$ of $HD - Kr$ at 296 K was obtained

from Reference [63] which was estimated following References [98] and [99]. No data was available for $B_{12}(T)$ of $HD - Kr$ at 195 K. For this case, the pressure data at 195 K were converted to the pressure at 296 K based on an ideal gas model and then the density was determined by using the $B_{12}(T)$ of $HD - Kr$ at 296 K. All virial coefficients used in this study are listed in Table 4.2.

4.4 Absorption Coefficient

The integrated absorption coefficient was obtained via an integration of Equation 4.5:

$$\begin{aligned} \int \frac{\alpha(\omega)}{\omega \rho_A N_0} d\omega &= \mathcal{F} \times \int \frac{A(\omega)}{\omega} d\omega \\ &= \mathcal{F} \times \int [\frac{D_0}{(\gamma/2)^2 + (\omega - \omega_0)^2} + \frac{2(\omega - \omega_0)E_0}{(\gamma/2)^2 + (\omega - \omega_0)^2}] d\omega \end{aligned} \tag{4.11}$$

where

$$\mathcal{F} = (\rho_A N_0 \mathcal{L} log_{10} e)^{-1}, \tag{4.12}$$

$\mathcal{L}$ is the length of the absorption cell which is 100 cm, ρ_A is the density of the absorber HD in amagat and N_0 is the Loschmidt's number. The integration of Equation 4.11 is straight forward. Since the dispersion part does not contribute to the integral, one finds

$$\int \frac{\alpha(\omega)}{\omega \rho_A N_0} d\omega = 4\mathcal{F} \frac{D_0}{\gamma} \arctan[\frac{2(\omega - \omega_0)}{\gamma}]. \tag{4.13}$$

Table 4.2: Virial coefficients ($cm^3/mole$) used in the density determination. $B_{11}(T)$ for HD is -11.05 $cm^3/mole$ at 77 K, 10.79 $cm^3/mole$ at 195 K and 14.37 $cm^3/mole$ at 296 K respectively.

Sample	Virial Coefficient					
	77 K		195 K		296 K	
	B_{12}	B_{22}	B_{12}	B_{22}	B_{12}	B_{22}
$HD-HD$	-11.05	-11.05	10.79	10.79	–	–
$HD-H_2$	-11.05	-11.05	10.79	10.79	14.37	14.37
$HD-He$	15.13	9.60	16.40	11.97	–	–
$HD-Ne$	3.16	-14.15	11.23	7.90	–	–
$HD-Ar$	–	–	-4.16	-49.13	–	–
$HD-Kr$	–	–	–	–	2.80	-52.60
$HD-N_2$	–	–	1.20	-37.48	13.04	-4.90

In the above integral the limits were set to be $\pm 3\gamma$ so that the total of six FWHM served as the integration range to avoid overestimating the intensity of the spectrum in the region of wings [63][100].

4.5 Dipole Moment and interference Parameters

According to the intracollisional theory developed by Herman, Tipping and Poll, the integrated absorption coefficient may be expressed as follows [44][46],

$$\begin{aligned} \int \frac{\alpha(\omega)}{\omega \rho_A N_0} d\omega &= \int \frac{\alpha^A(\omega)}{\omega \rho_A N_0} [1 + 2\rho N_0 \Delta' I + \rho^2 N_0^2 (\Delta'^2 - \Delta''^2) I^2] d\omega \\ &= C_0 + C_1 \rho + C_2 \rho^2. \end{aligned} \tag{4.14}$$

Comparing Equation 4.14 with Equation 2.107, one finds immediately:

$$\begin{aligned} C_0 &= (4\pi^2/3\hbar c)(J+1) P(J) \langle J|\mu^A|J+1\rangle^2 \\ &= C(J) \langle J|\mu^A|J+1\rangle^2 \end{aligned} \tag{4.15}$$

$$C_1 = 2 N_0 \Delta' I C_0 \tag{4.16}$$

$$C_2 = N_0^2 (\Delta'^2 - \Delta''^2) I^2 C_0. \tag{4.17}$$

Clearly C_0 leads to the magnitude of the matrix element of the allowed dipole moment while C_1 and C_2 lead to interference parameters.

There were two approaches employed in the fitting of Equation 4.14; a *free fitting* and a *theory fitting*. The free fitting consisted of fitting a second order

polynomial without any restriction. This was applied to the 1990 experiment data for comparison and discussion. The theory fitting used Equation 4.17 to specify the relationships between C_0, C_1 and C_2. It was applied for all the experiment data of 1987 and 1990. The *theory fitting* was made by introducing a parameter q such that:

$$q^{-1} = \frac{\rho N_0 \Delta'' I}{1 + \rho N_0 \Delta' I}, \tag{4.18}$$

where q^{-1} was calculable from the fitted parameters by comparison of Equation 4.5 with Equation 4.6 and Equation 4.14:

$$q^{-1} = \frac{E_0\gamma/D_0}{1 + \sqrt{1 + (E_0\gamma/D_0)^2}}. \tag{4.19}$$

Furthermore, Equation 4.14 may be linearized as follows,

$$\{[\int \alpha(\omega)/(\rho_A N_0 \omega) d\omega]/(1 - q^{-1})\}^{1/2} = C_0^{1/2}(1 + \rho N_0 \Delta' I) \tag{4.20}$$

$$\{[\int \alpha(\omega)/(\rho_A N_0 \omega) d\omega]/(q^2 - 1)\}^{1/2} = C_0^{1/2}(\rho N_0 \Delta'' I). \tag{4.21}$$

Thus C_0, $N_0\Delta' I$ and $N_0\Delta'' I$ were obtained from the above two linear fittings.

In the fitting of above curves, the spectra fitting parameters at zero perturber density of the $HD - X$ experiments were first determined. These values were added to the $HD - HD$ data to improve the accuracy of the intercept determination. Also the average value of the zero perturber density of $HD - X$ with the same HD density was taken as a zero density value to improve the fitting in $HD - X$ cases. All fitting was weighted with the error calculated from the

statistical error of parameters in the profile fitting. An estimated error in the density determination was also included. The magnitude of the matrix element for the allowed dipole moment transitions of HD was determined from C_0 of the $HD - HD$ curve via Equation 4.15:

$$\langle J|\mu^A(r)|J'\rangle = [C(J)^{-1}C_0]^{1/2}, \tag{4.22}$$

with

$$C(J) = (4\pi^2/3\hbar c)(J+1)P(J), \tag{4.23}$$

where J is the rotational quantum number and $P(J)$ is the Boltzmann function (c. f. Equation 2.106):

$$P(J) = \frac{e^{-\beta E_J} - e^{-\beta E_{J+1}}}{\sum_J (2J+1)e^{-\beta E_J}} \ . \tag{4.24}$$

The rotational energy in the above equation were estimated from the approximate equation [101]

$$E(J) = BJ(J+1) - DJ^2(J+1)^2 + HJ^3(J+1)^3 \ , \tag{4.25}$$

where the rotational constants $B = 44.6645 cm^{-1}$, $D = 0.02576 cm^{-1}$ and $H = 2.31 \times 10^{-4} cm^{-1}$ are the average values of three determinations [51][102][103]. The numerical values of $C(J)$ at 77 K, 195 K and 296 K are calculated and listed in Table 4.3.

Table 4.3: $C(J)$ $(debye^{-2}cm^{-1}amagat^{-1})$ calculated at different temperatures

Temperature (K)	$C(J)$ $J=0$	$J=1$	$J=2$	$J=3$
77	5.657	2.547	0.143	
195	1.586	2.488	1.181	0.239
296		1.685	1.333	0.553

The interference parameter $a = 2N_0\Delta' I$ was obtained from the ratio of C_1 and C_0. To determine $N_0\Delta'' I$, the interference parameter causing the asymmetry, we have plotted q^{-1} against density as expressed in Equation 4.18.

The results for $\langle J|\mu^A|J+1\rangle$, a and $N_0\Delta'' I$ are presented in the last section of this chapter.

4.6 Lineshape Parameters

The lineshape parameters are the broadening coefficient B_0 and the frequency shift S_0.

The density dependent line width FWHM was obtained from the profile fitting parameter γ. According to the impact theory, there is a linear relationship between γ and ρ [5][54]:

$$\gamma = B_0\rho + K_0, \tag{4.26}$$

where K_0 is the line width at zero perturber density. To obtain B_0, a straight line was fitted to the γ versus ρ and weighted with the statistical error in γ.

There is also a linear relationship between S_0 and ρ:

$$\omega_0 = S_0\rho + \omega_0^0, \tag{4.27}$$

where ω_0 is the line frequency obtained from the profile fitted and ω_0^0 is the frequency at zero perturber density. The same procedure was employed to obtain S_0.

In the case of $HD-HD$, ω_0^0 is the absolute frequency of the individual R(J) lines. As we mentioned in the previous chapter, although NICOLET calibrated the frequency of the spectrometer to the stated accuracy, a precise calibration is still needed for the determination of the line positions. This was done by a linear calibration with the water lines measured with the sample cell under vacumn assuming no collision frequency shift. Then, these water lines were fitted with a Lorentzian profile and compared with the highly accurate water line frequencies measured by J. W. C. Johns in 1985 [104].

The results of the absolute frequency of the R(J) lines of HD and the corresponding line shape parameters in the different cases are all presented in the next section.

4.7 Experimental Results

The experimental results from the data analysis described in this chapter are collectively presented in this section for the convenience of comparison. These

results will be discussed in chapter 6.

There are three parts in this section. Part one contains the magnitude of the matrix elements of the allowed dipole moment transitions and the absolute frequency of pure rotational lines of pure HD, and part two presents the interference parameters. All line shape parameters are presented in part three. Diagrams in this section were selected from 240 diagrams representing the different samples at different temperatures with different fitting procedures.

Part One

The magnitude of the matrix
elements of the allowed
dipole moment transitions
and the absolute
frequency of pure
rotational lines of pure HD.

Table 4.4: The magnitude of the matrix elements of the allowed dipole moment transitions of HD ($10^{-4} debye$). The uncertainty appears in parentheses.

Experiment	$\langle J\|\mu^A\|J+1\rangle$			
	$J=0$	$J=1$	$J=2$	$J=3$
$77K$	7.19(3)	7.68(4)	7.79(6)	
$195K$[a]	8.03(12)	8.01(4)	8.12(6)	7.84(23)
$195K$[b]	8.75(4)	8.09(3)	8.15(2)	8.62(15)
$296K$[c]	8.83(28)	7.94(2)	7.88(3)	8.43(10)
Average	7.77(4)	7.95(4)	8.05(4)	8.41(13)

a: 1987 experiment.

b: 1990 experiment.

c: 1986 experiment, *c.f.* Reference [63].

Table 4.5: The absolute frequency of pure rotational lines of HD (cm^{-1}). The uncertainty appears in parentheses.

Experiment	ω_0^0			
	R(0)	R(1)	R(2)	R(3)
1986[a]	89.19(1)	177.84(1)	265.23(1)	350.85(1)
1987[b]	89.22(1)	177.84(1)	265.24(1)	350.86(1)
1990[c]	89.21(1)	177.84(1)	265.246(5)	350.86(1)
Average	89.21(1)	177.84(1)	265.24(1)	350.86(1)

a: average value from 295 K experiments, *c.f.* Reference [63].

b: average value from 77 K and 195 K expriments in 1987. *c.f.* Reference [5].

c: from 195 K experiment in 1990.

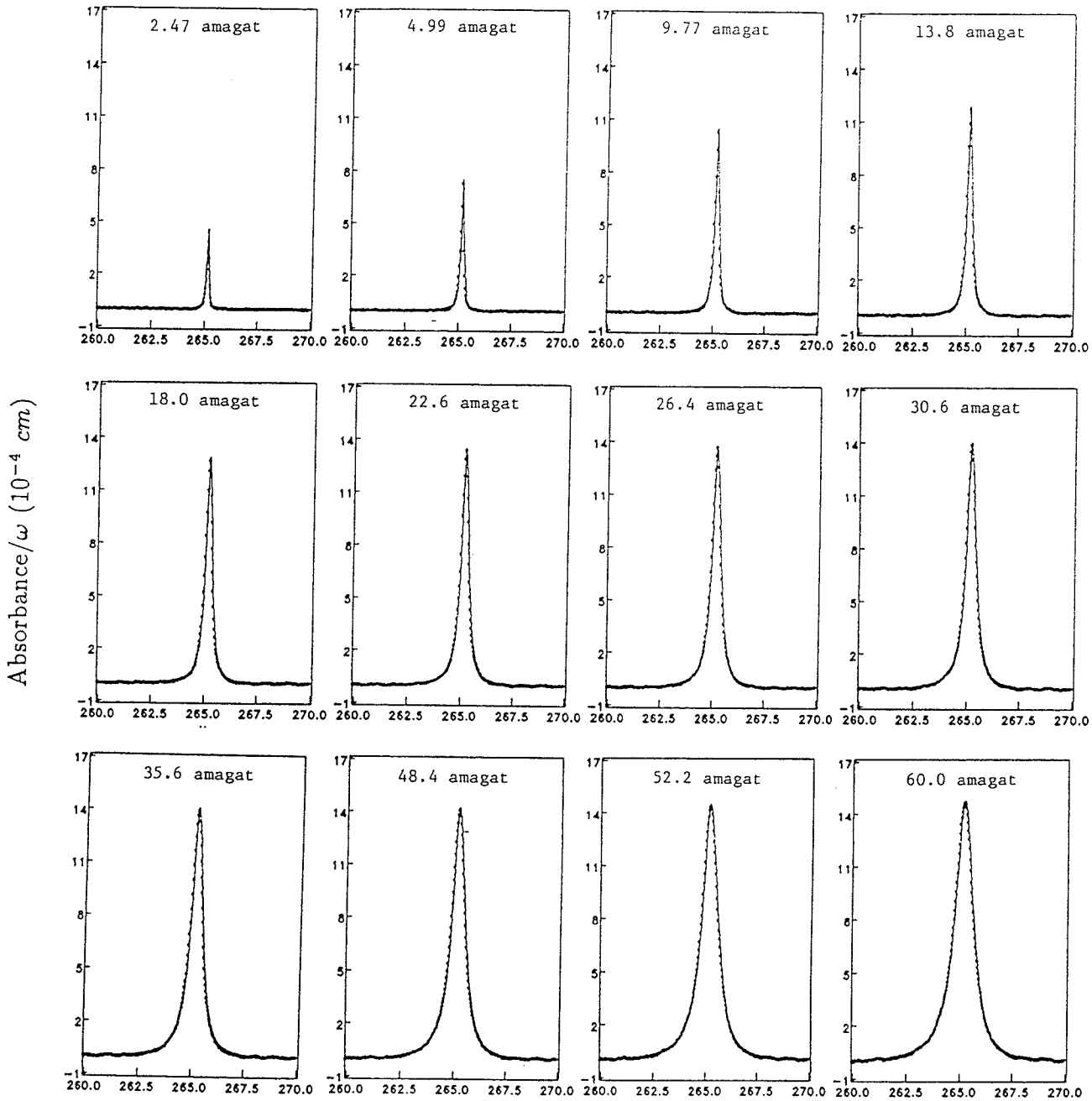

Figure 4.5: $R(2)$ line of pure HD at 195 K and the density from $2.5 - 60$ amagat

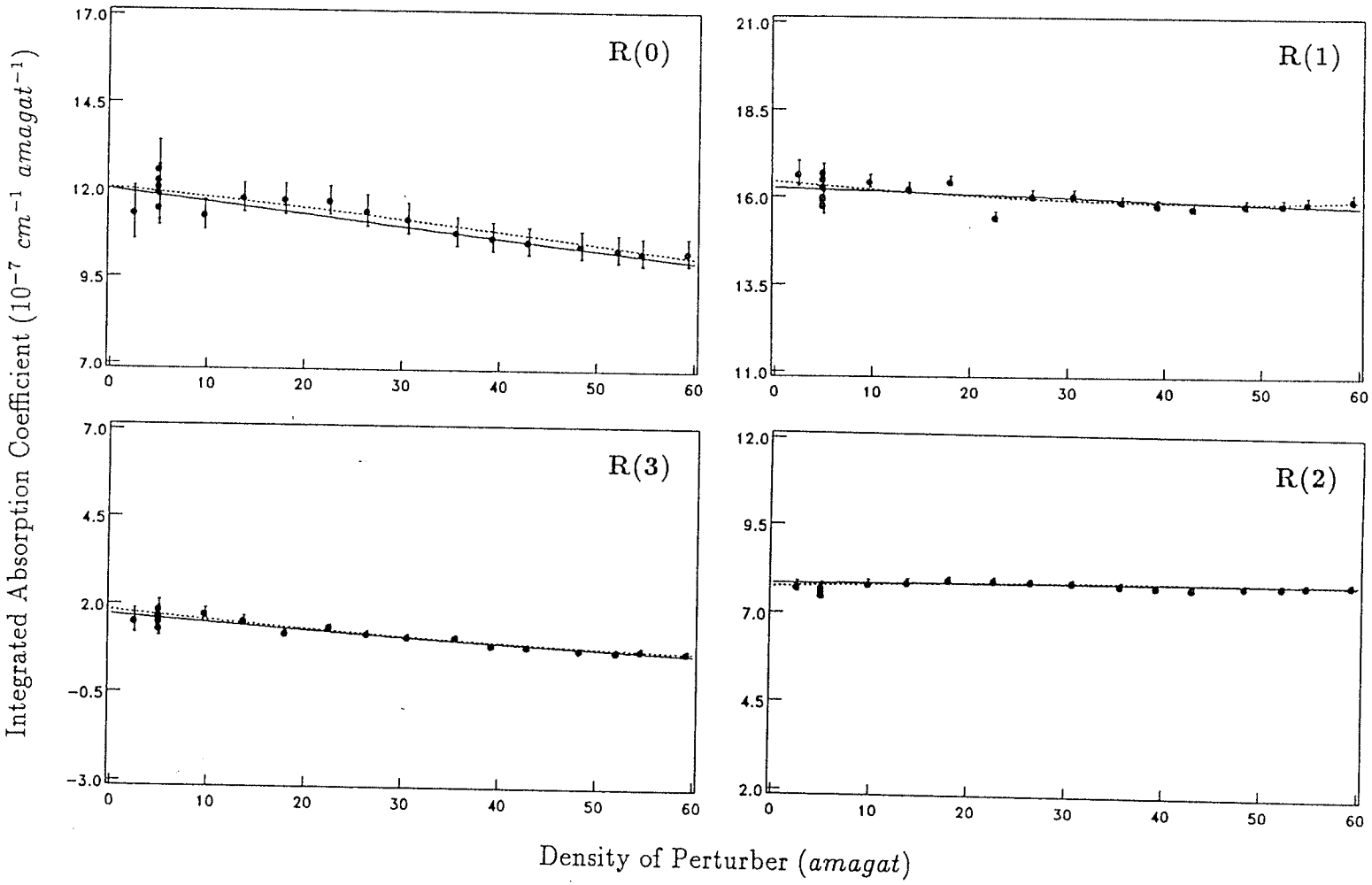

Figure 4.6: Integrated absorption coefficient for R(0), R(1), R(2) and R(3) of $HD - HD$ at 195 K as a function of density. Points are experimental. The dashed line is the free fitted curve and the solid line is the theory fitted curve.

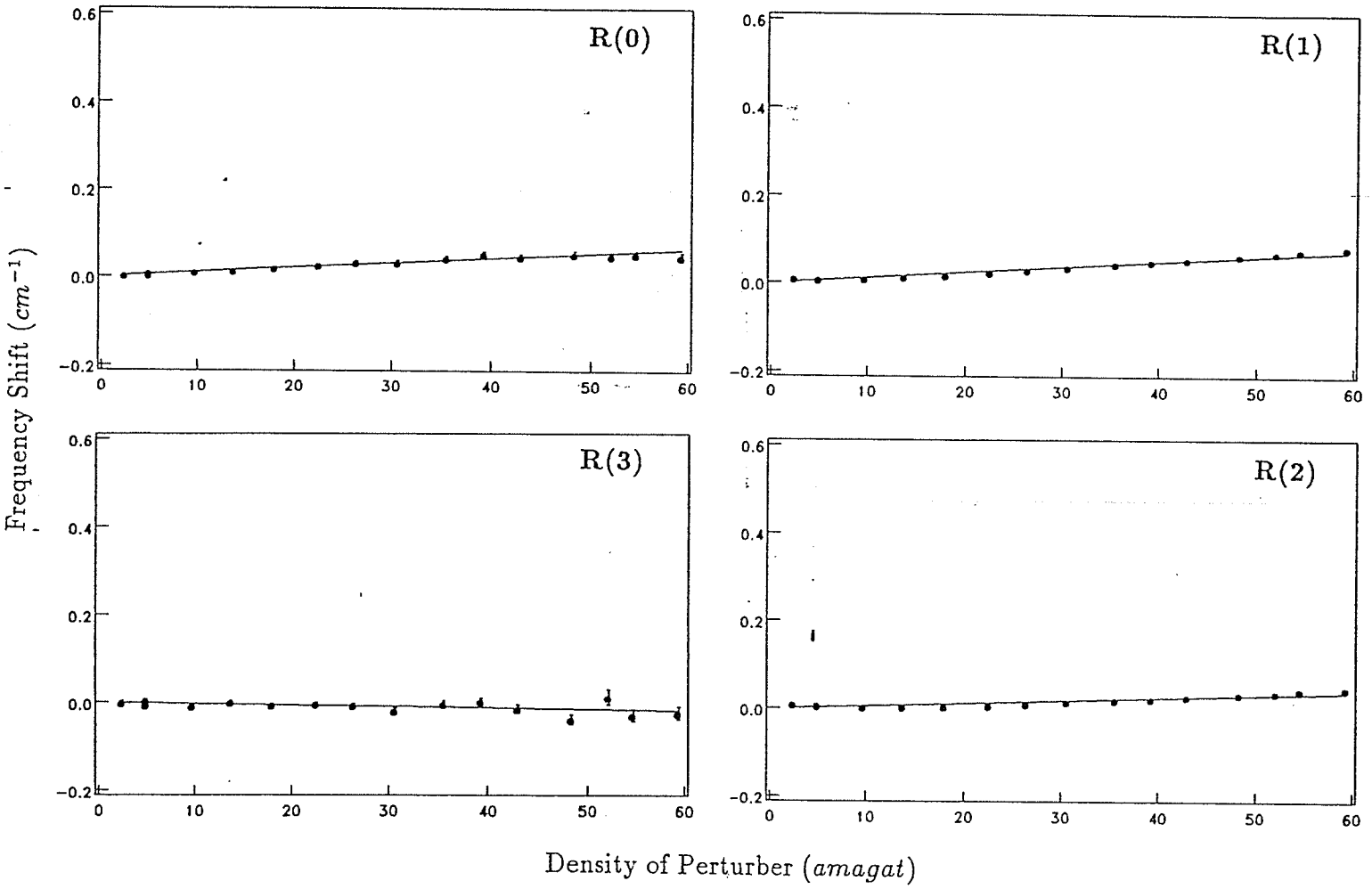

Figure 4.7: The frequency shift for R(0), R(1), R(2) and R(3) for $HD - HD$ at 195 K. Points are experimental and the solid line is the fitted curve. The shift is plotted relative to ω_0^0 of R(0) to R(3) respectively.

Part Two

The interference parameters

of

$HD - HD$ and $HD - X$.

Table 4.6: The interference parameter a (10^{-3} $amagat^{-1}$). The uncertainty appears in parentheses.

Sample	T (K)	R(0)	R(1)	R(2)	R(3)
$HD-HD$	77[b]	+3.1(4)	+2.2(2)	−3.7(8)	
	195[a]	−2.2(11)	−1.59(76)	+1.09(62)	−14.4(26)
	195[b]	−2.86(25)	−0.5(2)	+0.20(14)	−12.6(8)
	296[c]	−2.5(19)	−1.1(2)	+1.31(1)	+2.1(6)
$HD-H_2$	77[b]	+5.4(15)	+2.2(14)	+0.8(29)	
	195[a]	+2.5(52)	+0.6(12)	+0.03(14)	+3.9(10)
	195[b]	+2.0(13)	−3.6(5)	+0.14(40)	−6.2(41)
	296[a]		−11.5(31)	−9.7(24)	−11.4(53)
	296[b]		−7.1(11)	−7.62(79)	−4.4(18)

a: free fitting.

b: theory fitting.

c: 1986 experiment, *c.f.* Reference [63].

Table 4.7: The interference parameter a (10^{-3} $amagat^{-1}$). The uncertainty appears in parentheses.

Sample	T (K)	R(0)	R(1)	R(2)	R(3)
$HD-He$	77[b]	+6.0(16)	+6.2(7)	+4.4(15)	
	195[a]	−31.5(84)	−4.4(21)	−3.4(22)	+18(10)
	195[b]	−11.4(38)	−0.4(9)	+2.34(92)	+3.5(28)
	296[c]		+5.7(9)	+3.9(8)	+10.0(19)
$HD-Ne$	77[b]	+6.0(16)	+6.2(7)	+4.4(15)	
	195[a]	−0.3(37)	+1.9(13)	+6.68(68)	+9.1(107)
	195[b]	+4.7(12)	−1.0(4)	+4.34(23)	+12.2(29)
	296[c]		+2.1(4)	+6.9(4)	+5.3(12)
$HD-Ar$	195[a]	−0.3(24)	−0.9(21)	+3.5(10)	−0.4(90)
	195[b]	+1.08(97)	−3.93(72)	+9.5(67)	+2.5(31)
	296[c]		+1.8(3)	+6.1(2)	+9.4(11)
$HD-Kr$	195[a]	+5.9(32)	−1.0(26)	−5.4(46)	+21(32)
	195[b]	+3.8(11)	−18.4(21)	+11.3(25)	+13.8(93)
	296[a]		−21.0(35)	−11.6(21)	+4.2(36)
	296[b]		−19.3(14)	−8.63(69)	−7.1(12)
$HD-N_2$	195[a]	+22(15)	+7.7(95)	+8.9(40)	+12(37)
	195[b]	+15.8(47)	−10.6(21)	+4.2(13)	+12(10)
	296[a]		−16.2(26)	+13.3()	−4.1(89)
	296[b]		−22.2(14)	+8.28(82)	−4.5(25)

a: free fitting. b: theory fitting.

c: 1986 experiment, *c.f.* Reference [63].

Table 4.8: The interference parameter $N_0\Delta''I$ (10^{-4} $amagat^{-1}$). The uncertainty appears in parentheses.

Sample	T (K)	R(0)	R(1)	R(2)	R(3)
$HD-HD$	77[a]	−2.0(8)	−0.7(7)	+1.7(27)	
	195[b]	−0.05(158)	−4.61(76)	−6.01(35)	+12.4(18)
$HD-H_2$	77[a]	−13(3)	+10(2)	+3.8(14)	
	195[b]	−4.0(57)	−10.0(10)	−10.1(14)	+10.0(33)
	296[b]		−17.8(50)	+8.6(27)	+8.9(31)
$HD-He$	77[a]	+15(3)	+13(3)	+40(10)	
	195[a]	+17(12)	+10.9(23)	+8.9(33)	+33.4(96)
$HD-Ne$	77[a]	+15(3)	+11(2)	−6(30)	
	195[b]	+25.3(52)	+17.5(10)	+11.3(72)	+2.4(20)
$HD-Ar$	195[b]	−72.5(61)	+8.0(11)	−20.3(15)	+96(23)
$HD-Kr$	195[b]	+26.7(66)	+11.1(81)	+29.9(54)	+11(35)
	296[b]		+12.9(25)	+1.0(29)	+0.2(27)
$HD-N_2$	195[b]	+8.7(83)	+18.4(27)	−20.4(24)	+4.8(34)
	296[b]		+10.2(17)	−4.3(14)	+14.0(63)

a: 1987 experiment.

b: 1990 experiment.

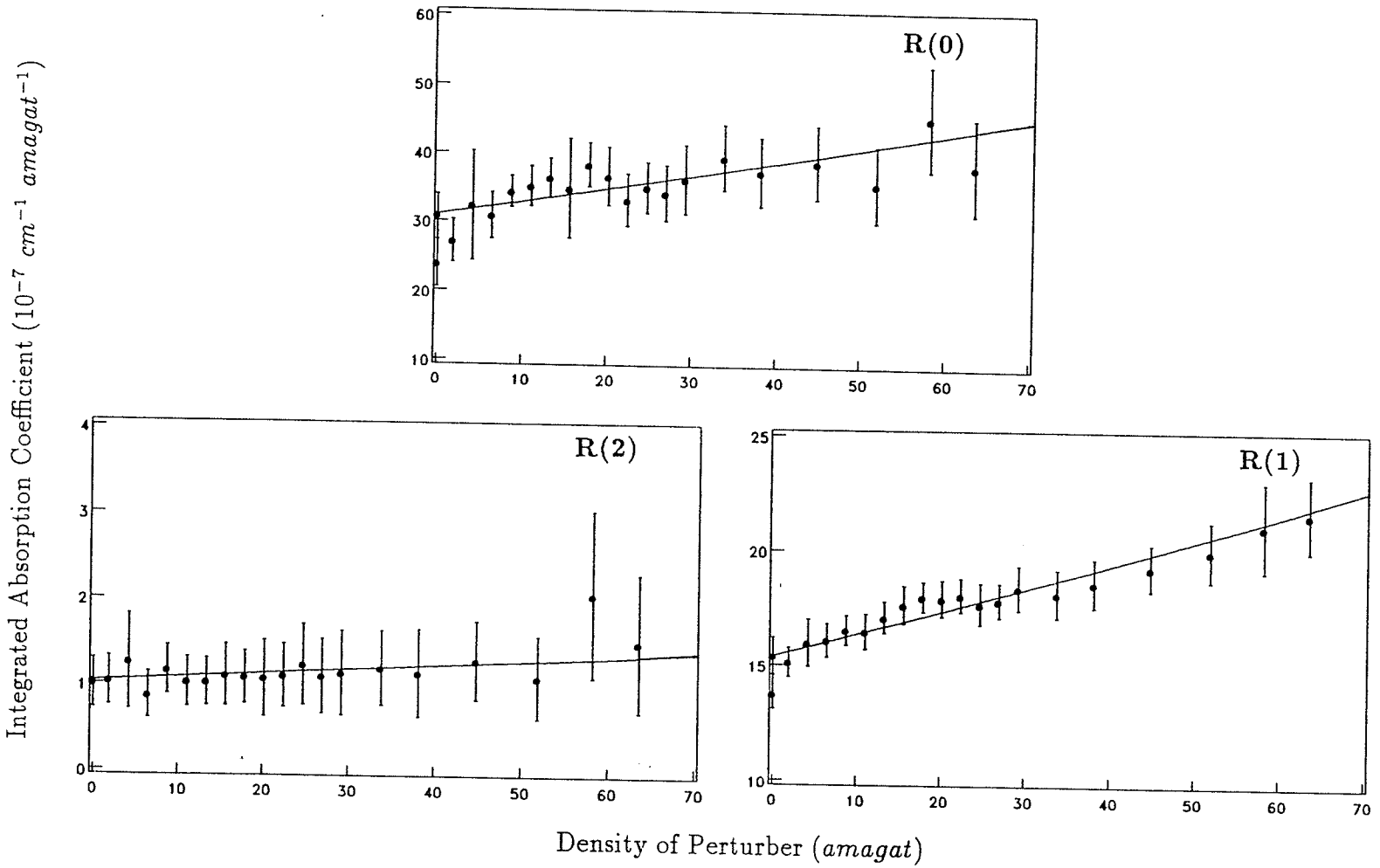

Figure 4.8: Integrated absorption coefficient for R(0), R(1) and R(2) of $HD - He$ at 77 K as a function of density. Points are experimental. The solid line is the theory fitted curve.

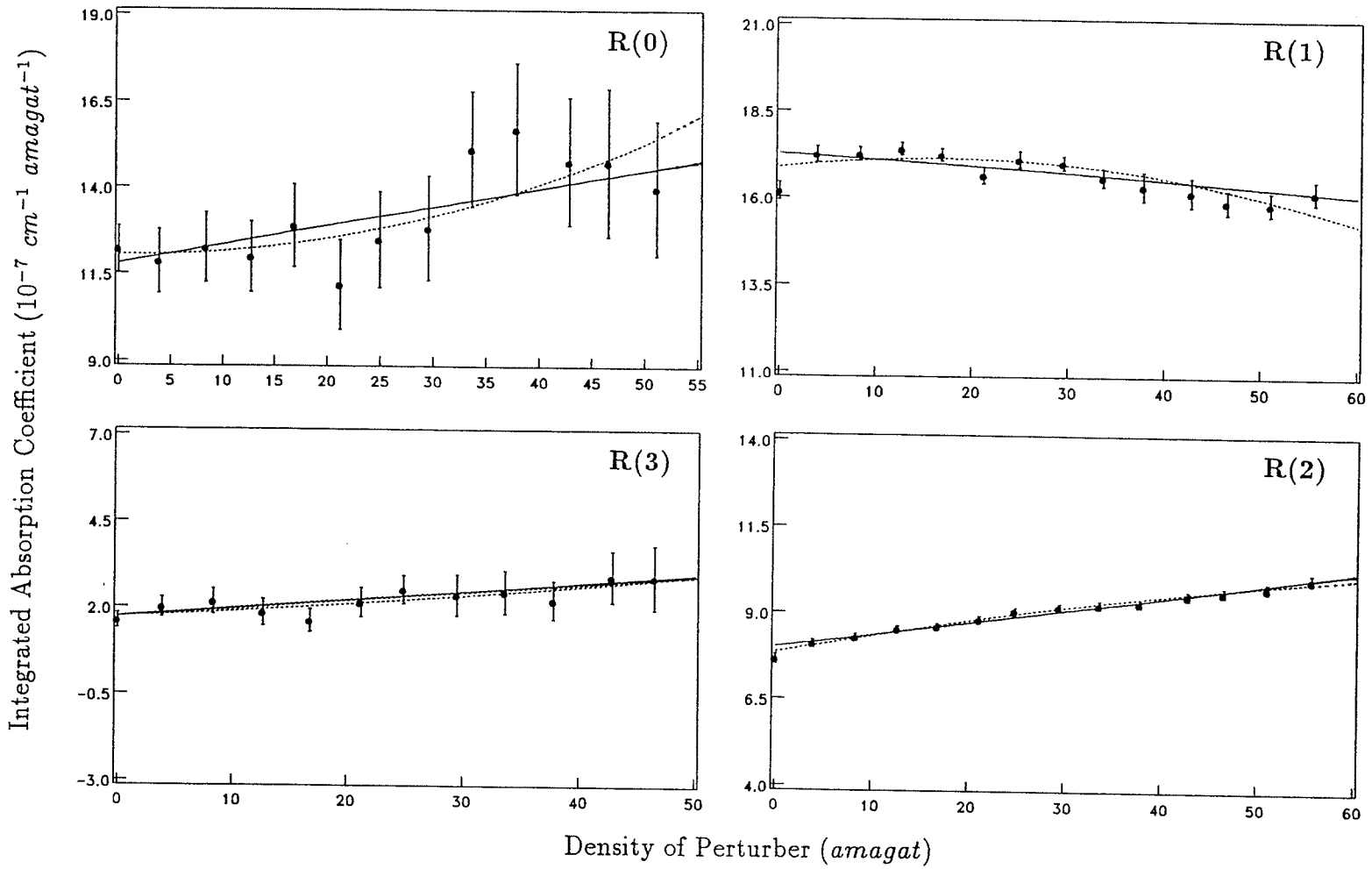

Figure 4.9: Integrated absorption coefficient for R(0), R(1), R(2) and R(3) of $HD-Ne$ at 195 K as a function of density. Points are experimental. The dashed line is the free fitted curve and the solid line is the theory fitted curve.

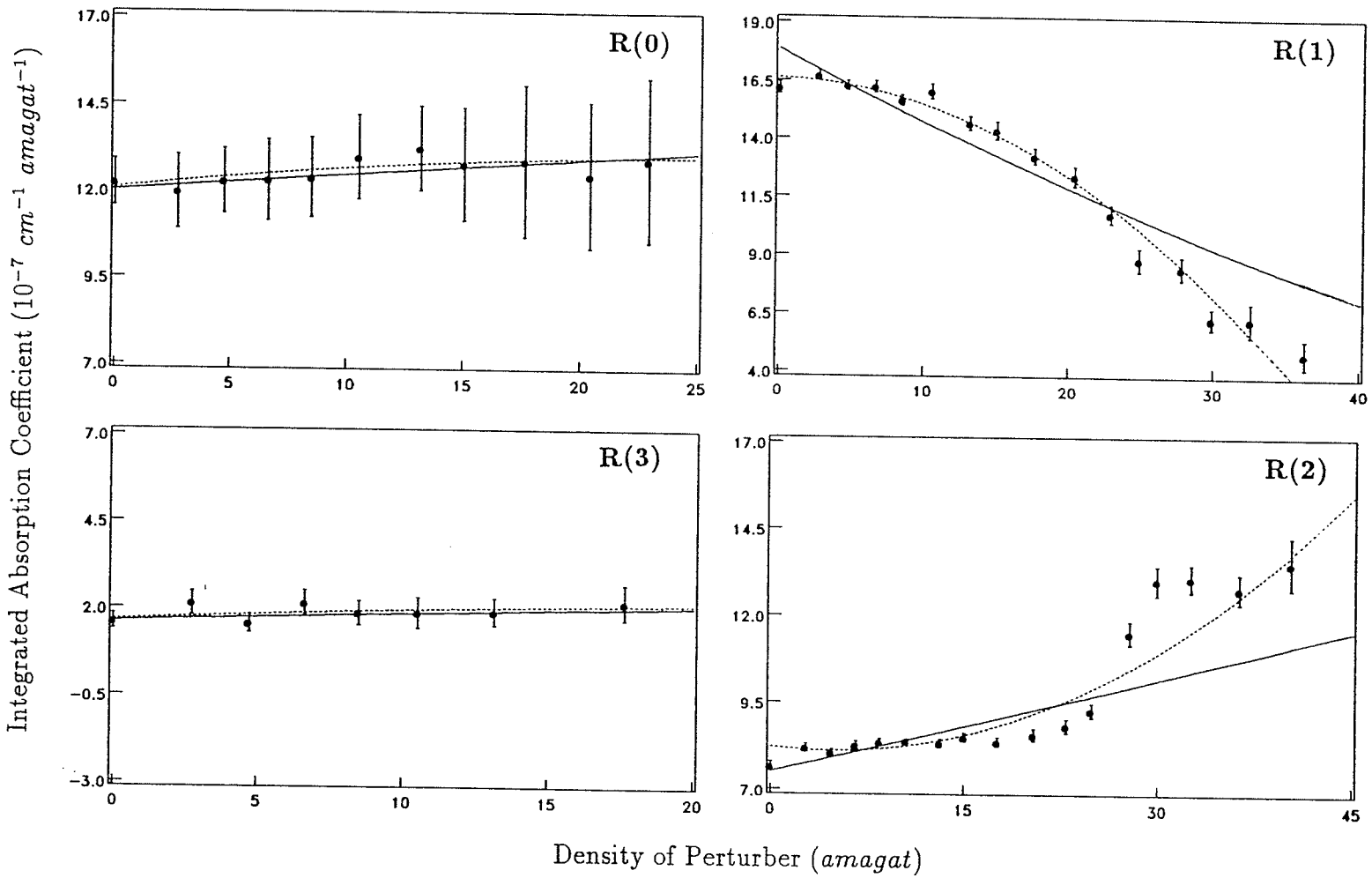

Figure 4.10: Integrated absorption coefficient for R(0), R(1), R(2) and R(3) of $HD-Kr$ at 195 K as a function of density. Points are experimental. The dashed line is the free fitted curve and the solid line is the theory fitted curve.

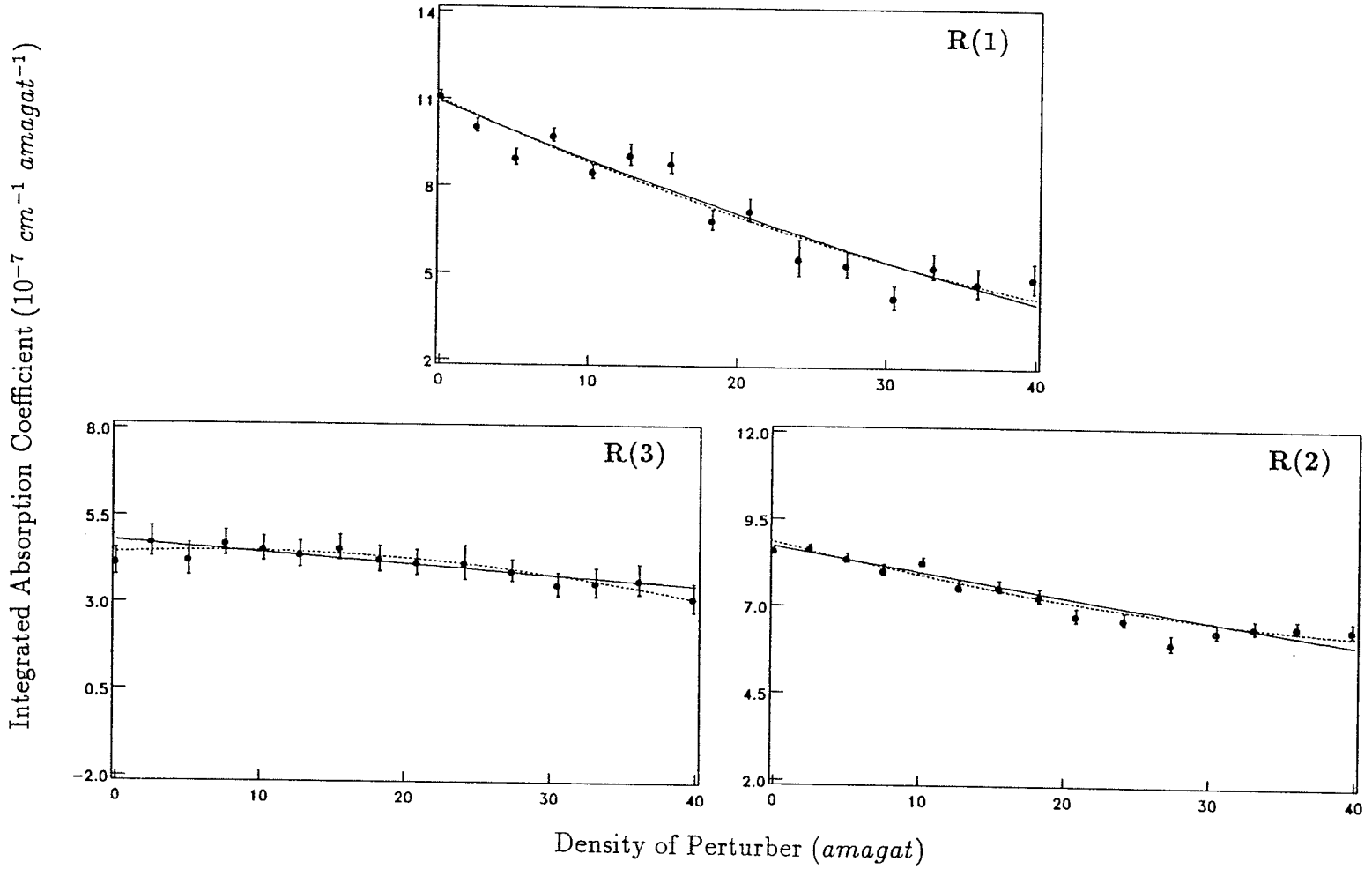

Figure 4.11: Integrated absorption coefficient for R(1), R(2) and R(3) of $HD-Kr$ at 296 K as a function of density. Points are experimental. The dashed line is the free fitted curve and the solid line is the theory fitted curve.

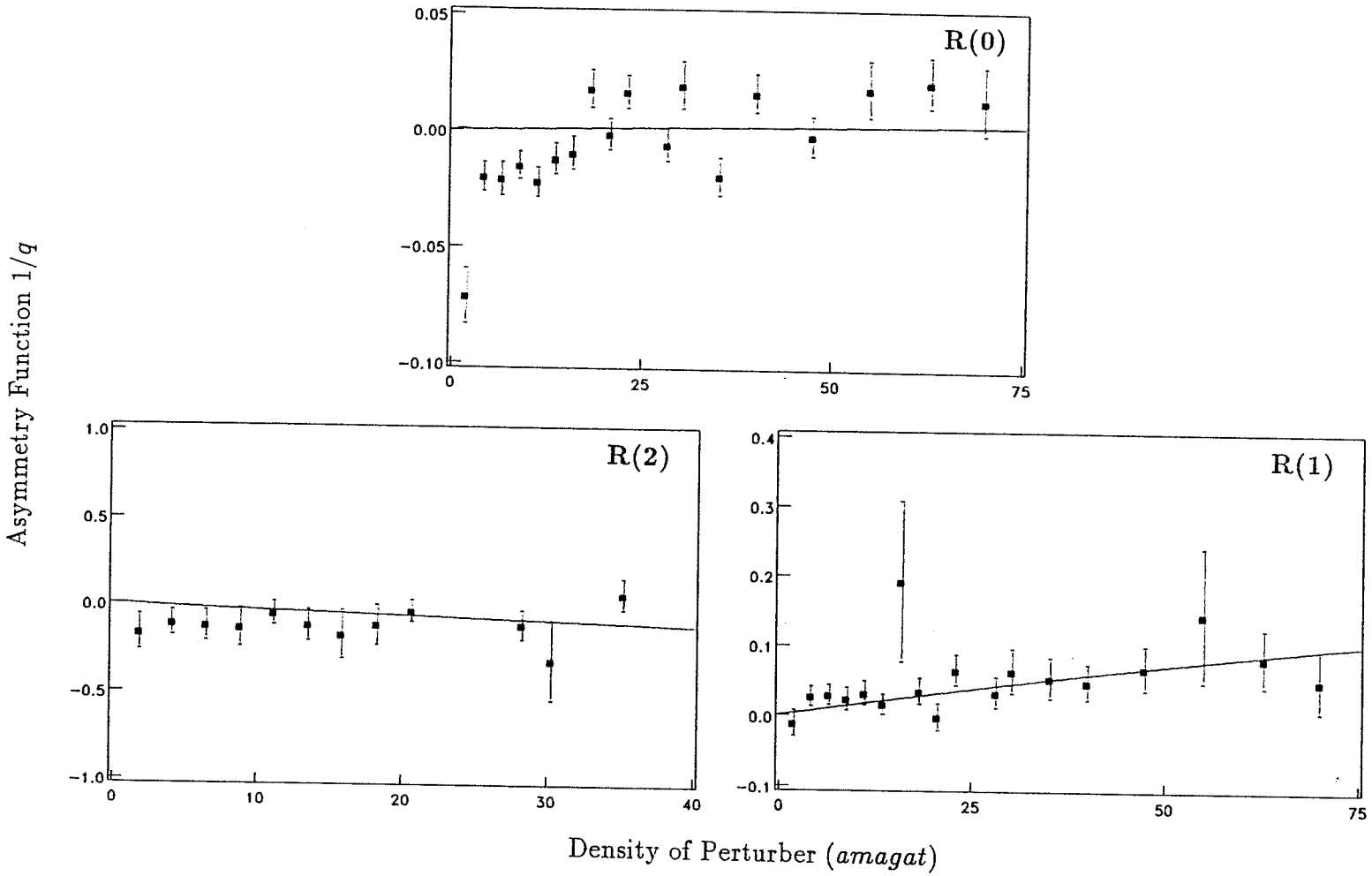

Figure 4.12: $1/q$ for R(0), R(1) and R(2) of $HD - Ne$ at 77 K as a function of density. Points are experimental. The solid line is the fitted curve.

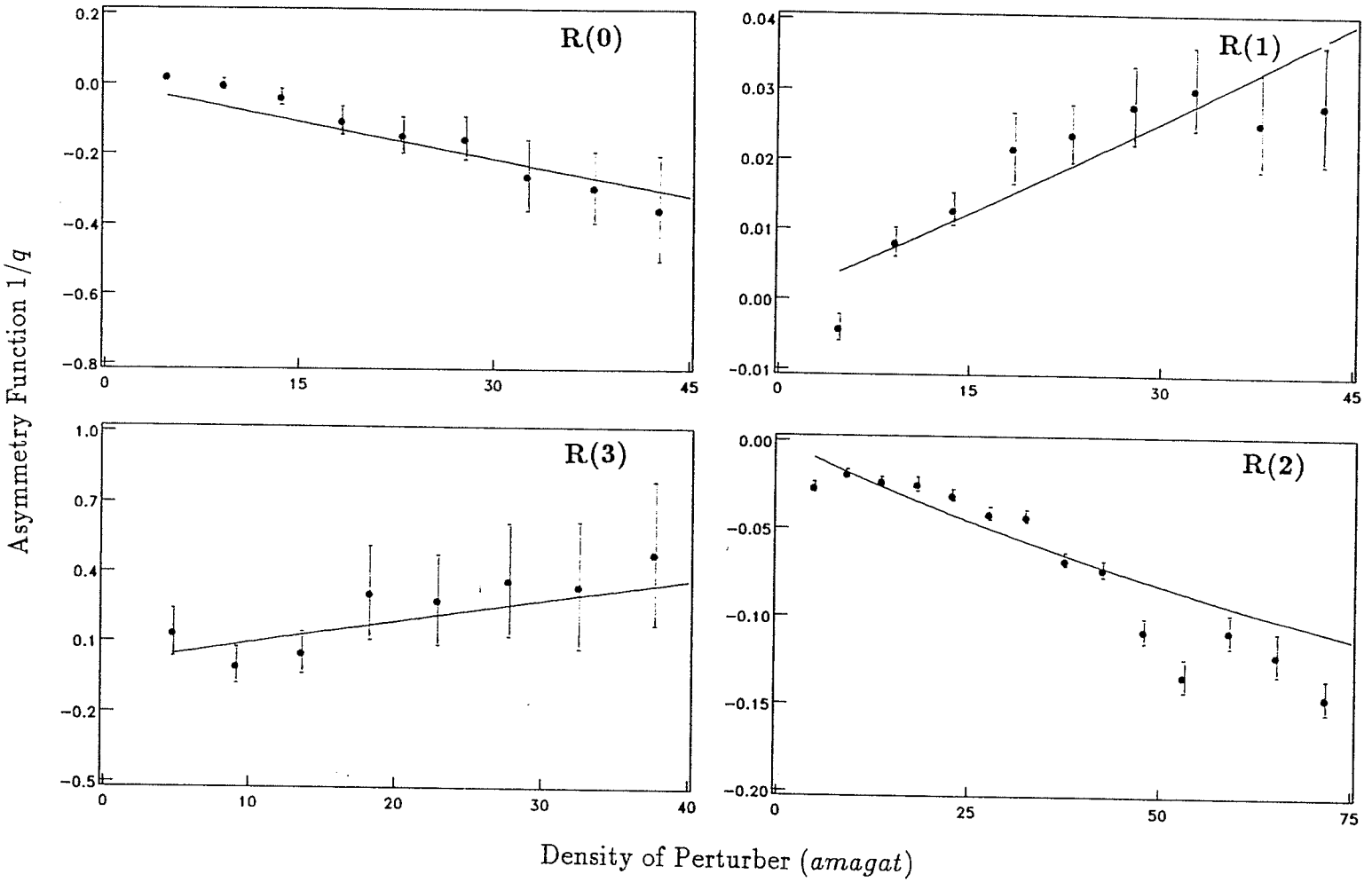

Figure 4.13: $1/q$ for R(0), R(1), R(2) and R(3) of $HD-Ar$ at 195 K as a function of density. Points are experimental. The solid line is the fitted curve.

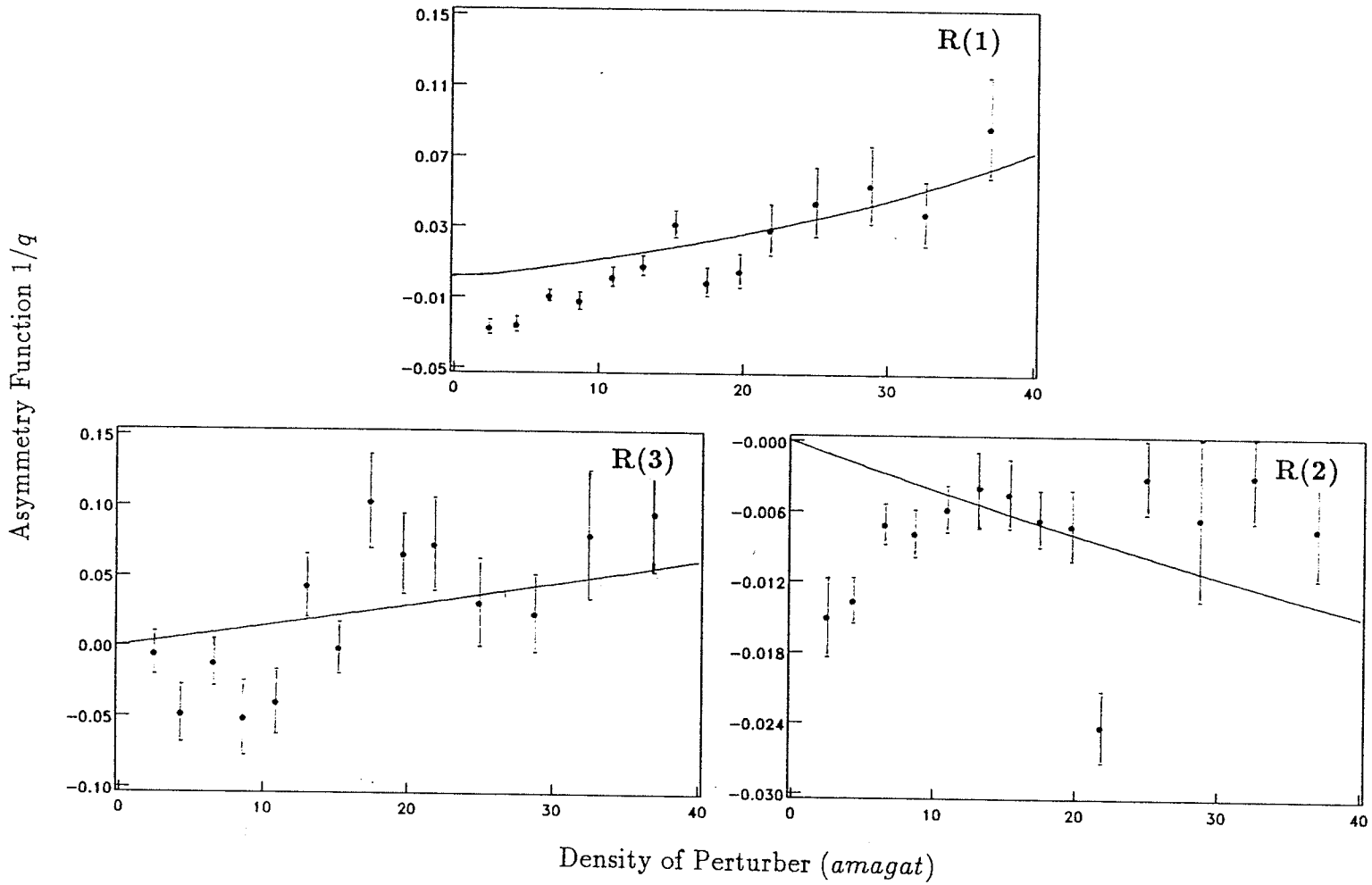

Figure 4.14: $1/q$ for R(1), R(2) and R(3) of $HD - N_2$ at 296 K as a function of density. Points are experimental. The solid line is the fitted curve.

Part Three

Line shape parameters

of

HD–HD and HD–X.

Table 4.9: The FWHM broadening coefficients B_0 (10^{-2} cm^{-1} $amagat^{-1}$). The uncertainty appears in parentheses.

Sample	T (K)	R(0)	R(1)	R(2)	R(3)
$HD-HD$	77[a]	0.544(26)	0.879(6)	0.822(32)	
	195[b]	1.80(1)	1.610(9)	1.508(4)	1.23(2)
	296[c]	3.32(16)	2.53(1)	2.20(1)	1.81(3)
$HD-H_2$	77[a]	0.577(35)	0.785(11)	0.610(87)	
	195[b]	1.788(16)	1.525(16)	1.555(13)	1.303(66)
	296[b]		2.273(55)	1.885(36)	2.309(67)
$HD-He$	77[a]	0.293(12)	0.391(11)	0.234(40)	
	195[a]	1.05(12)	1.01(2)	0.81(1)	0.75(11)
	296[c]		2.13(6)	1.35(4)	1.17(9)
$HD-Ne$	77[a]	0.474(14)	0.665(13)	0.366(79)	
	195[b]	1.608(27)	1.217(13)	1.040(2)	0.954(49)
	296[c]		1.68(3)	1.50(2)	0.68(6)
$HD-Ar$	195[b]	2.879(57)	2.079(42)	1.730(21)	1.27(15)
	296[c]		2.96(4)	2.19(2)	1.35(5)
$HD-Kr$	195[b]	3.053(33)	2.375(63)	2.194(73)	1.821(87)
	296[b]		2.681(32)	1.972(37)	1.091(74)
$HD-N_2$	195[b]	4.100(40)	2.791(51)	1.972(11)	1.67(11)
	296[b]		2.70(13)	2.844(31)	1.36(9)

a: 1987 experiment.

b: 1990 experiment.

c: 1986 experiment, *c. f.* Reference[63].

Table 4.10: The frequency-shift coefficients S_0 (10^{-3} cm^{-1} $amagat^{-1}$). "+" and "−" refer to *blue* and *red* shift respectively. The uncertainty appears in parentheses.

Sample	T (K)	R(0)	R(1)	R(2)	R(3)
$HD-HD$	77[a]	+0.305(67)	+0.074(18)	−0.24(10)	
	195[b]	+1.07(4)	+1.21(4)	+0.61(4)	−0.31(8)
	296[c]	+3.5(5)	+0.6(1)	+0.6(1)	−0.4(1)
$HD-H_2$	77[a]	+0.31(5)	+0.37(3)	−3.15(31)	
	195[b]	+1.02(26)	+1.15(5)	+0.64(8)	−2.4(7)
	296[b]		+1.51(25)	+0.29(13)	−3.01(44)
$HD-He$	77[a]	+0.58(4)	+0.65(3)	−1.11(22)	
	195[a]	+0.98(13)	+2.15(12)	+1.22(8)	−0.45(58)
	296[c]		+2.4(2)	+2.8(1)	+1.8(3)
$HD-Ne$	77[a]	+1.01(6)	+1.13(5)	−0.86(32)	
	195[b]	+0.98(13)	+1.76(4)	+0.32(4)	+0.87(28)
	296[c]		+4.4(1)	+2.4(1)	+0.3(2)
$HD-Ar$	195[b]	+4.78(47)	+2.51(7)	+0.51(8)	−5.8(3)
	296[b]		+8.3(3)	+1.3(1)	−1.1(2)
$HD-Kr$	195[b]	+1.6(1)	+3.28(2)	−3.0(17)	−5.4(5)
	296[b]		+3.52(23)	−0.515(54)	−2.03(16)
$HD-N_2$	195[b]	+2.08(57)	+3.54(10)	+0.17(11)	−3.11(47)
	296[b]		+5.28(16)	+0.713(99)	−2.65(33)

a: 1987 experiment.

b:1990 experiment.

c: 1986 experiment, *c. f.* Reference[63].

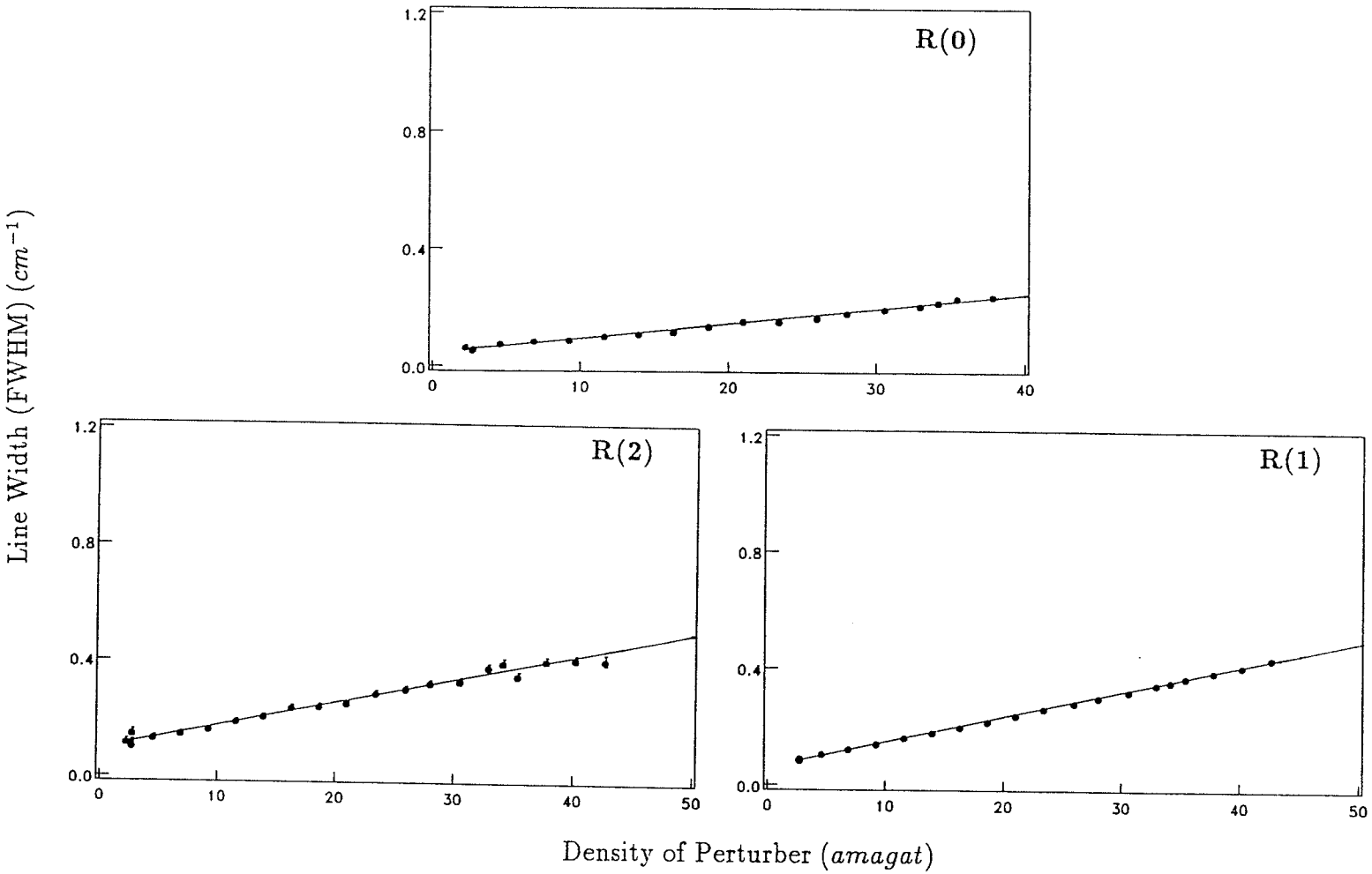

Figure 4.15: Linewidth, full width at half maximum (FWHM), for R(0), R(1) and R(2) of $HD - HD$ at 77 K as a function of density. Points are experimental. The solid line is the fitted curve.

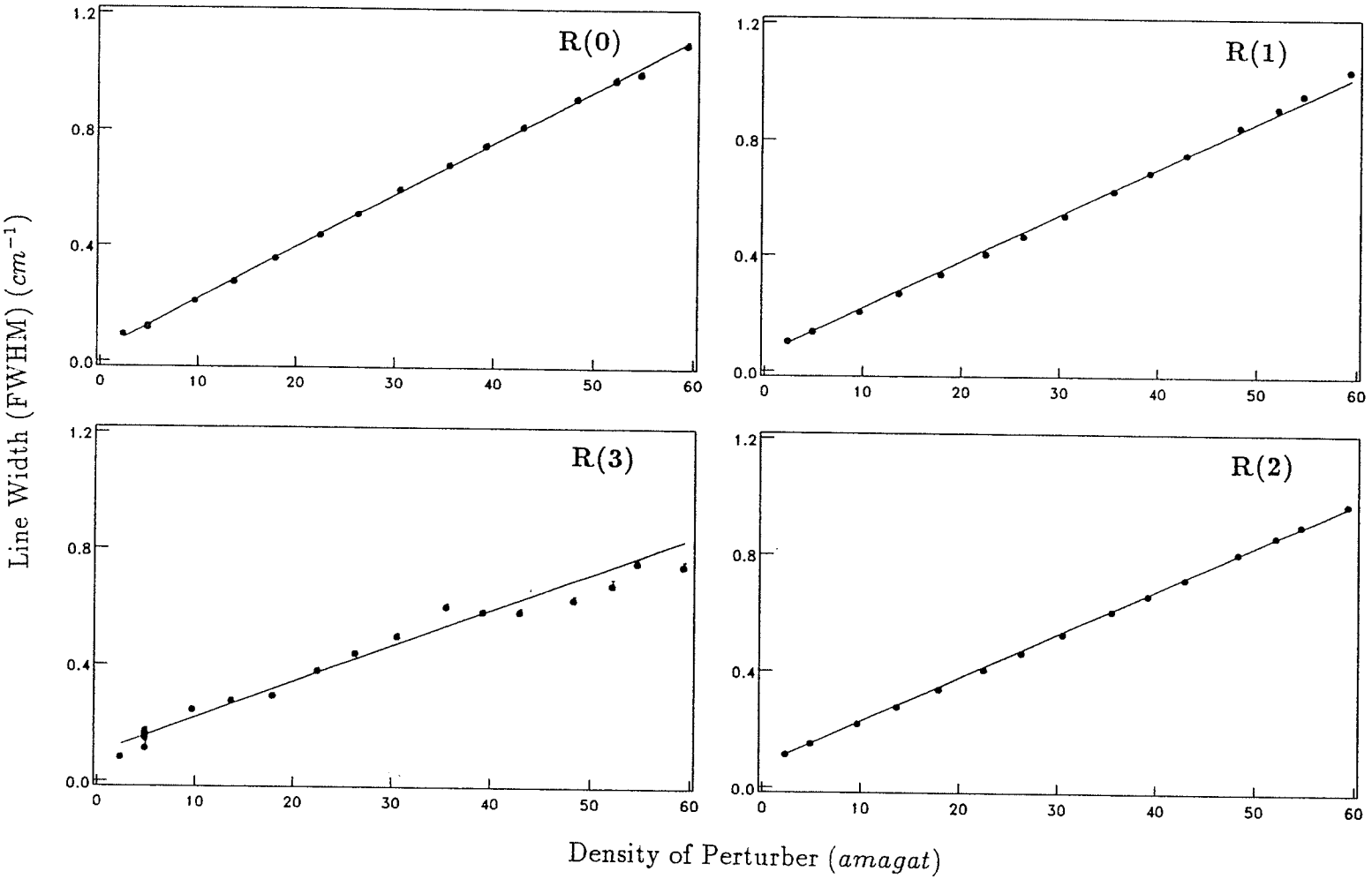

Figure 4.16: Linewidth, full width at half maximum (FWHM), for R(0), R(1), R(2) and R(3) of $HD - HD$ at 195 K as a function of density. Points are experimental. The solid line is the fitted curve.

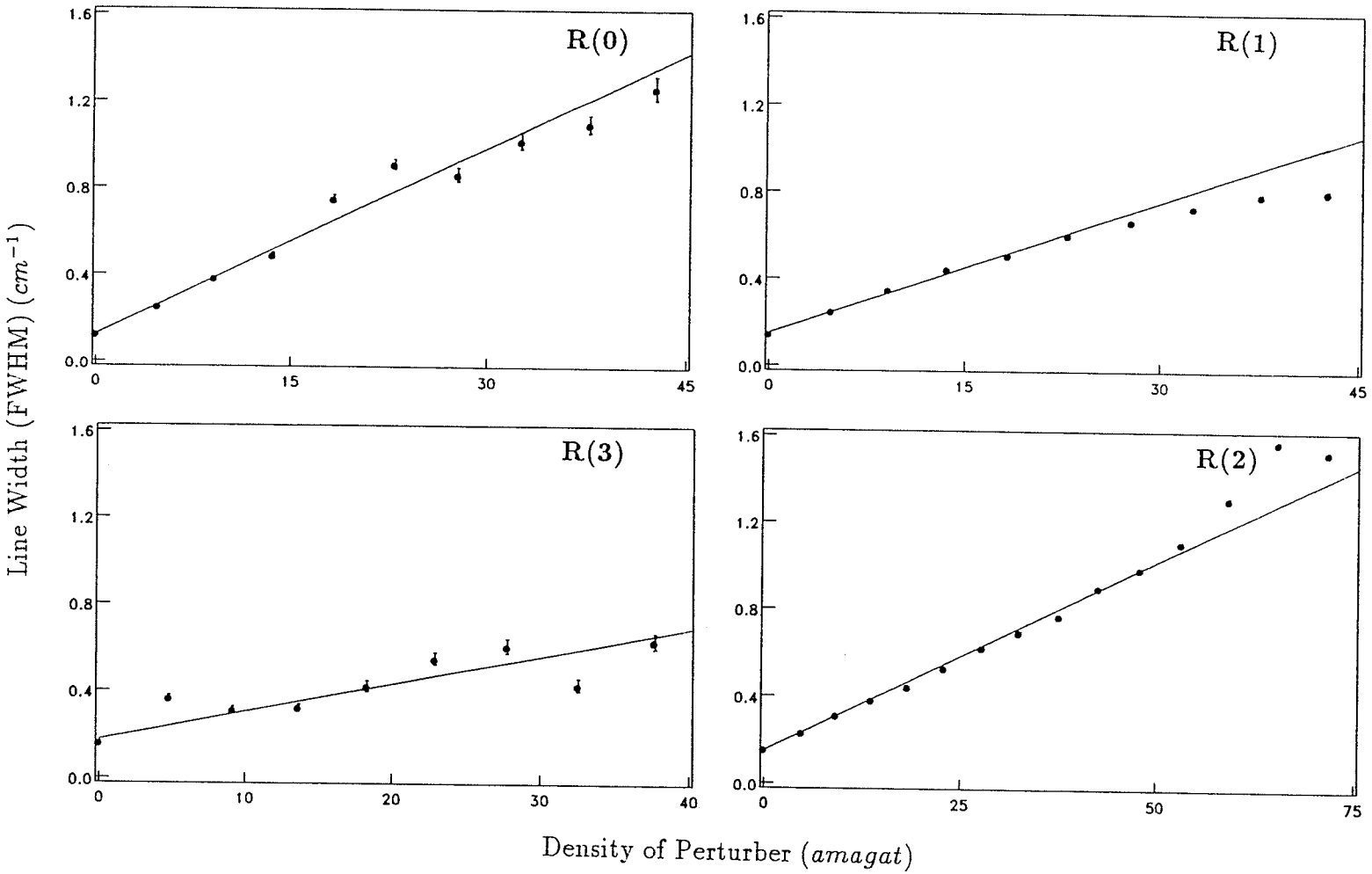

Figure 4.17: Linewidth, full width at half maximum (FWHM), for R(0), R(1), R(2) and R(3) of $HD - Ar$ at 195 K as a function of density. Points are experimental. The solid line is the fitted curve.

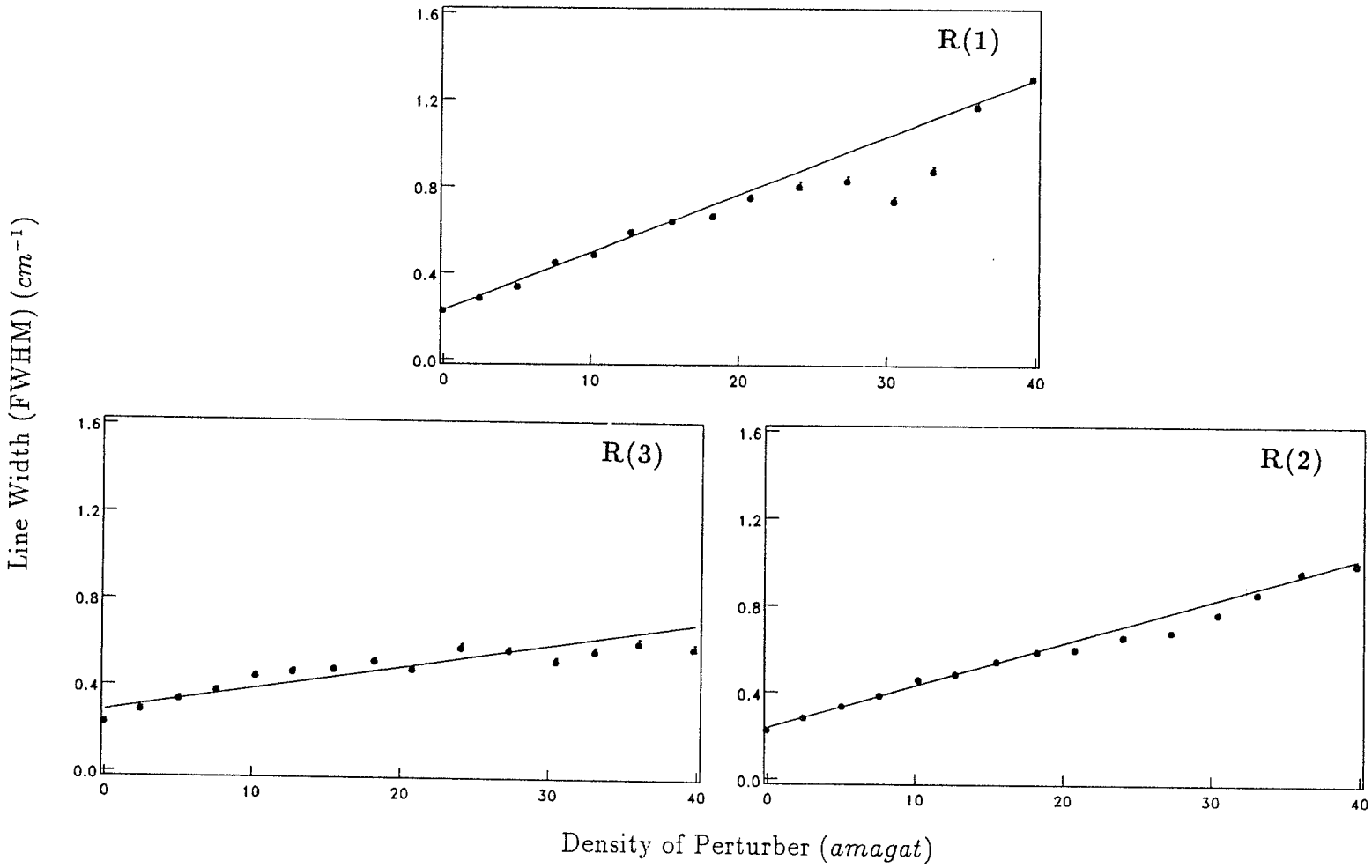

Figure 4.18: Linewidth, full width at half maximum (FWHM), for R(1), R(2) and R(3) of $HD - Kr$ at 296 K as a function of density. Points are experimental. The solid line is the fitted curve.

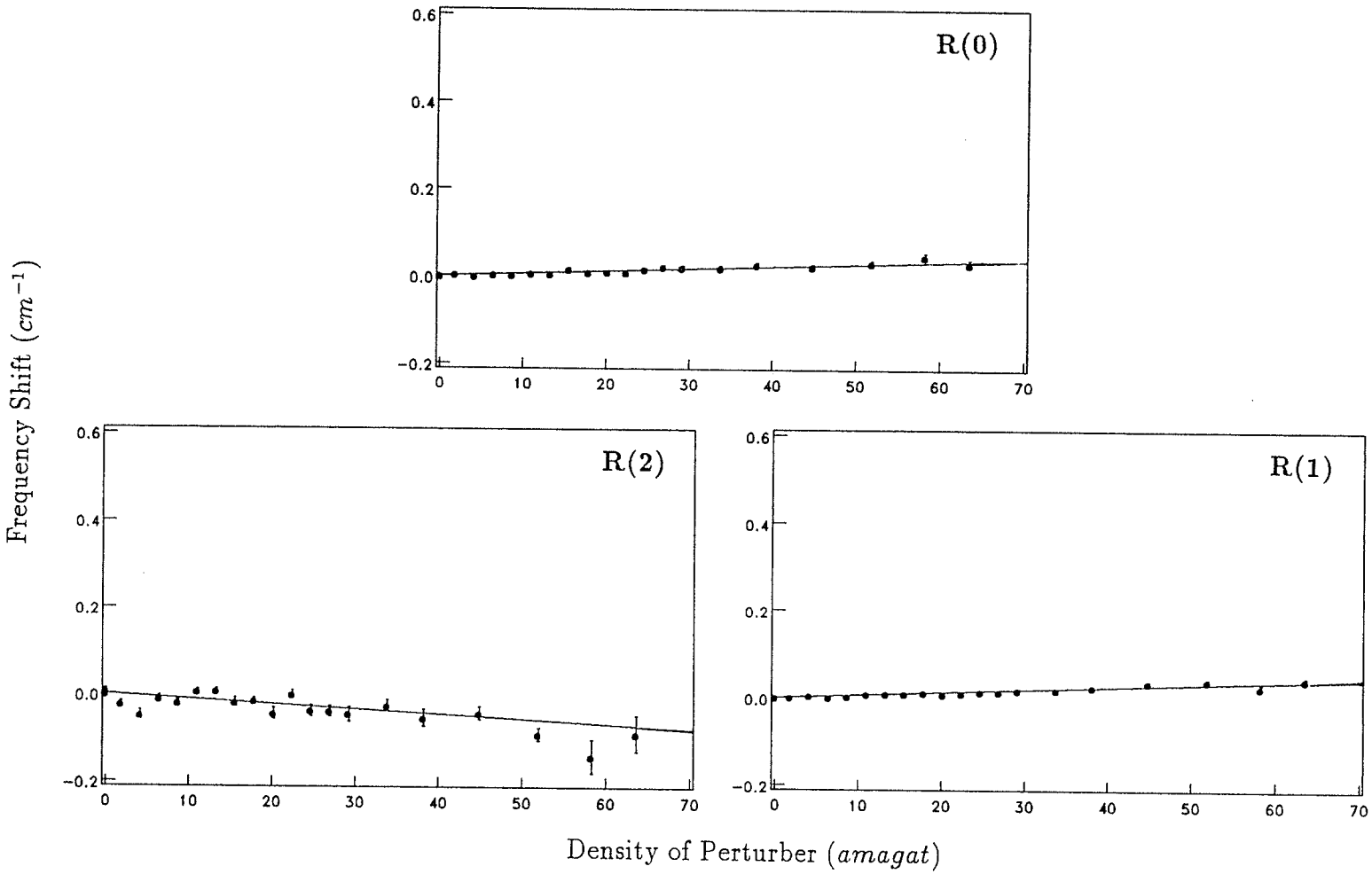

Figure 4.19: The frequency shift for R(0), R(1) and R(2) of $HD - He$ at 77 K as a function of density. Points are experimental. The solid line is the fitted curve.

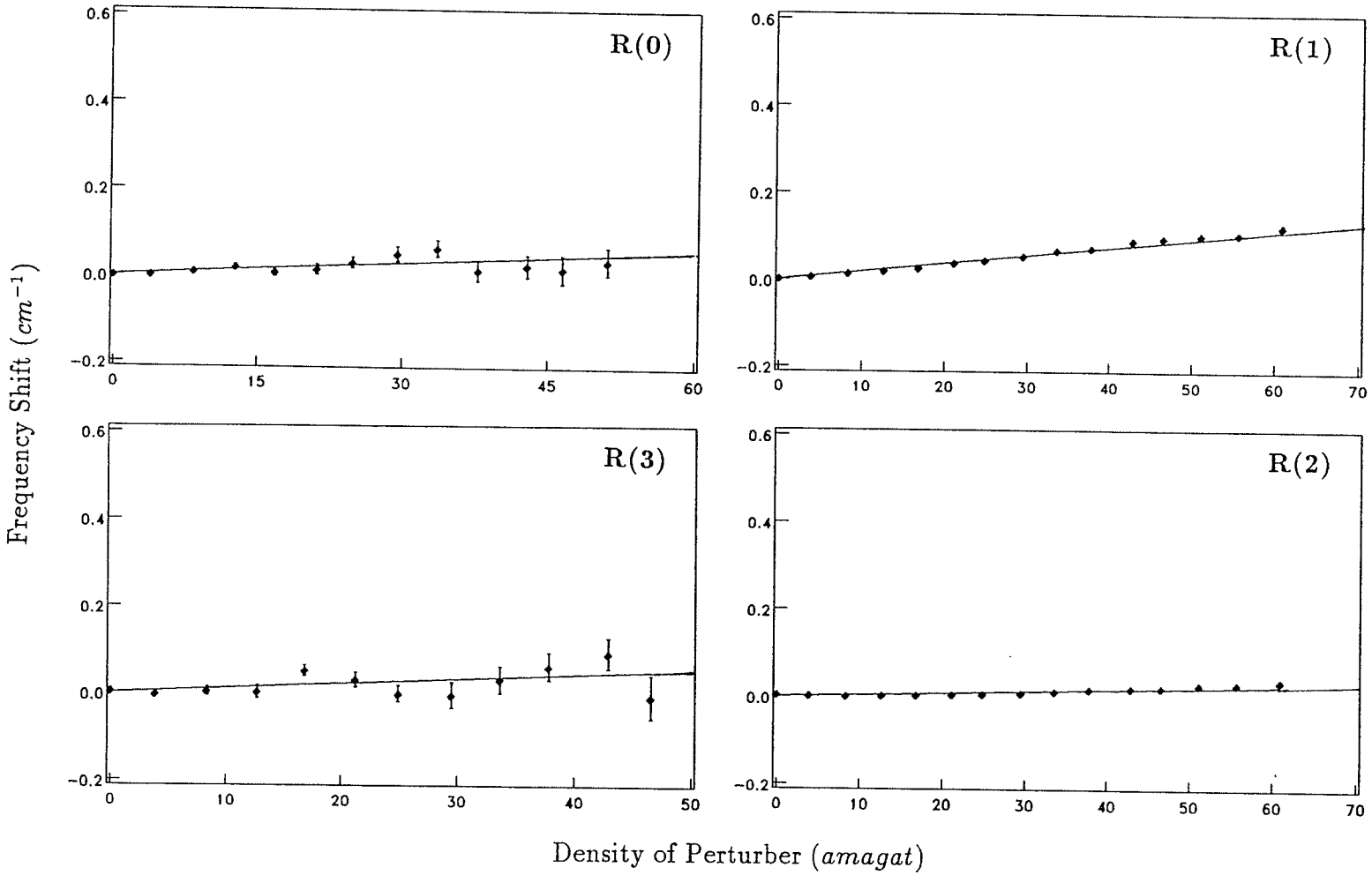

Figure 4.20: The frequency shift for R(0), R(1), R(2) and R(3) of $HD - Ne$ at 195 K as a function of density. Points are experimental. The solid line is the fitted curve.

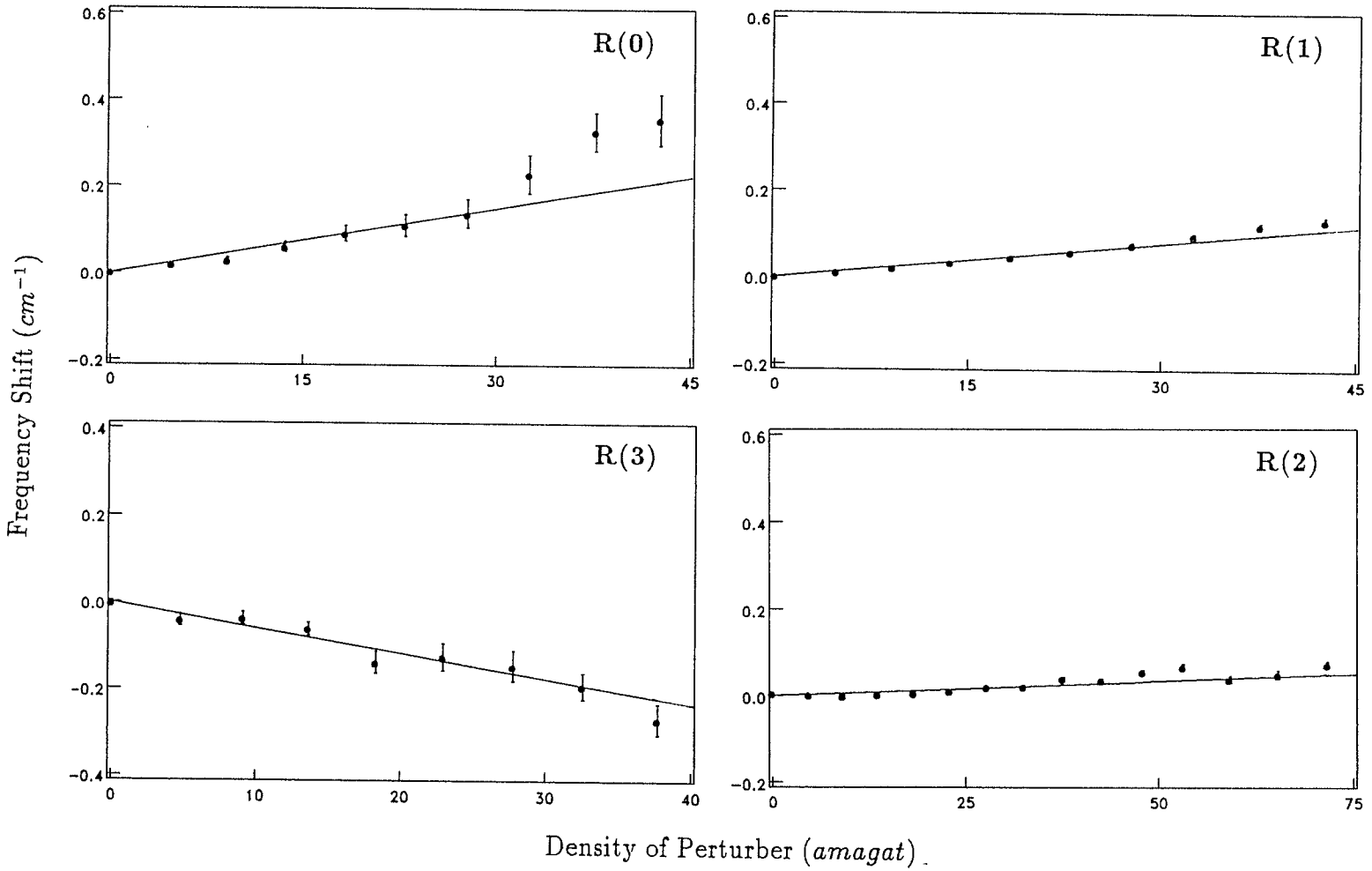

Figure 4.21: The frequency shift for R(0), R(1), R(2) and R(3) of $HD - Ar$ at 195 K as a function of density. Points are experimental. The solid line is the fitted curve.

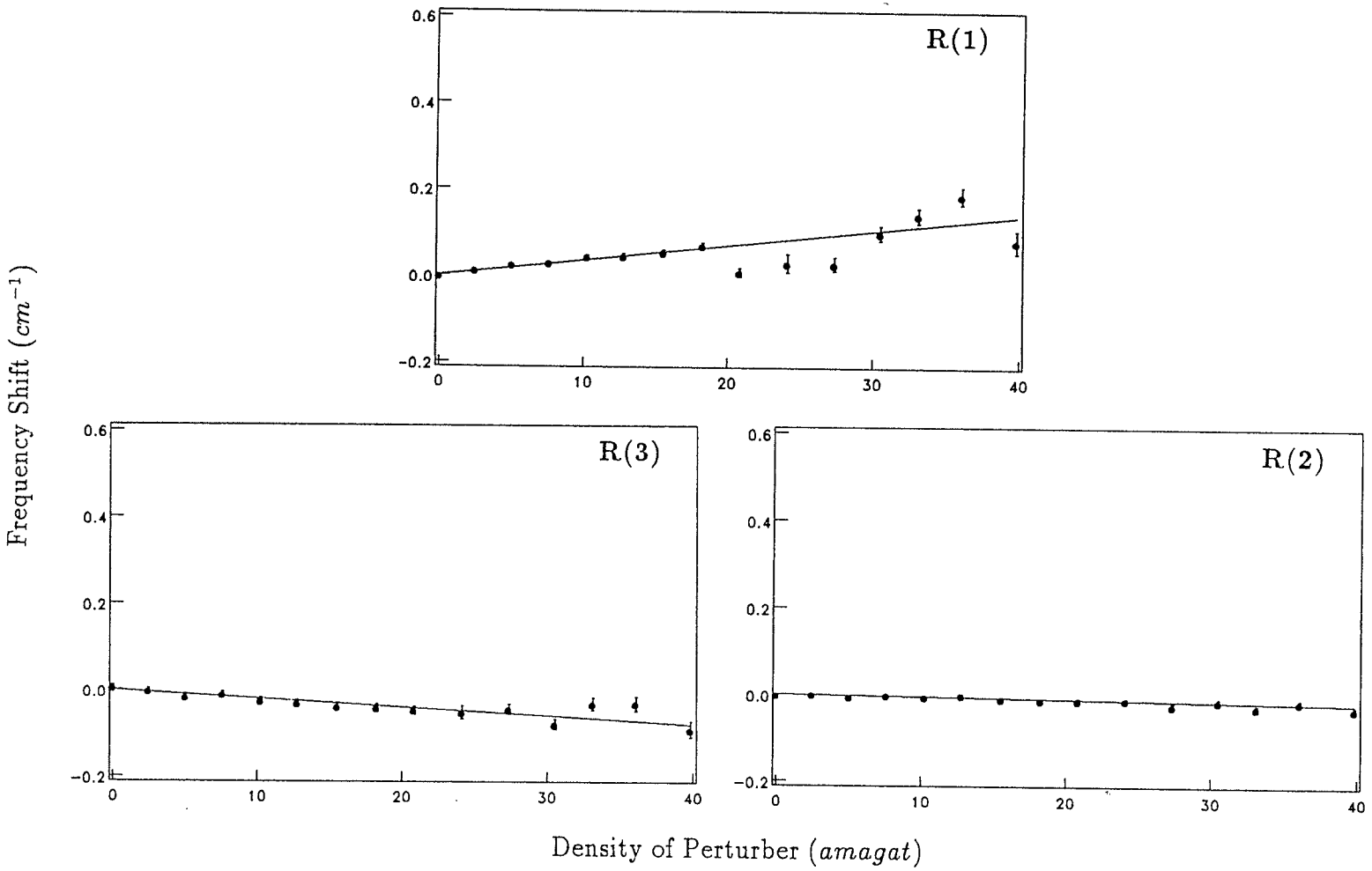

Figure 4.22: The frequency shift for R(1), R(2) and R(3) of $HD-Kr$ at 296 K as a function of density. Points are experimental. The solid line is the fitted curve.

Chapter 5

THEORETICAL CALCULATIONS

In order to compare our experimental results to the existing theory, we will now calculate the interference parameters a and Δa, based on the theory developed by Herman, Tipping and Poll, with refinements introduced by Tabisz and Nelson and Ma *et al.* [44][46][52][53], and with the line broadening following the semiclassical theory developed by Robert and Bonamy [105][106][107][108]. The details of the above calculations are the main topics of this chapter.

5.1 Calculations of the Interference parameters a and Δa

To calculate the interference parameter a, we take Equation 4.14 as a starting point;

$$\int \frac{\alpha(\omega)}{\omega \rho_A N_0} d\omega = \int \frac{\alpha^A(\omega)}{\omega \rho_A N_0} [1 + 2\rho N_0 \Delta' I + \rho^2 N_0^2 (\Delta'^2 - \Delta''^2) I^2] d\omega, \qquad (5.1)$$

with

$$\Delta = \Delta' + i\Delta'' \tag{5.2}$$

and [46]

$$\Delta = \frac{\ll if|P[R(t)]U_i(\tau_c)U_f^{\dagger}(\tau_c)|if \gg}{P(R)}, \tag{5.3}$$

where the notation is as the same as that used in chapters 2 and 4.

The phase shifts Δ' and Δ'' depend on the interacting species and the temperature and have not been theoretically evaluated [5]. However, in view of the unitarity property of the time-development operators $U_i(\tau_c)$ and $U_f^{\dagger}(\tau_c)$, which are diagonal, the absolute magnitude of either Δ' and Δ'' can never exceed unity [46]. Therefore in the so-called *gentle-encounter limit* defined by Herman, Tipping and Poll, the time-development operators remain real and essentially equal to unity [46]. The line shape at this limit is pressure-broadened Lorentzian [45]. From the expression for a given in the previous chapter, within the GE limit, a now becomes

$$a = 2N_0 I, \tag{5.4}$$

and Equation 5.1 becomes

$$\int \frac{\alpha(\omega)}{\omega\rho_A N_0} d\omega = \int \frac{\alpha^A(\omega)}{\omega\rho_A N_0} d\omega (1 + \rho a + \rho^2 \frac{a^2}{4}). \tag{5.5}$$

On the other hand, we have [44][53]

$$\int \frac{\alpha(\omega)}{\omega\rho_A N_0} d\omega = \int \frac{\alpha^A(\omega)}{\omega\rho_A N_0} d\omega + \int \frac{\alpha^{AI}(\omega)}{\omega\rho_A N_0} d\omega + \cdots, \tag{5.6}$$

where the superscript AI denotes the contribution to the integral intensity resulting from the interference between *allowed* and *induced* dipole, and dots refers to the higher order terms involving the intercollisional interference proportional to ρ^2. Comparing the above two equations, one finds,

$$a = \int \frac{\alpha^{AI}(\omega)}{\omega} d\omega / [\rho \int \frac{\alpha^{A}(\omega)}{\omega} d\omega]. \tag{5.7}$$

The integrated intensity of *allowed* – *induced* is given by [44][53]

$$\begin{aligned} \int \frac{\alpha^{AI}(\omega)}{\omega} d\omega &= \frac{8\pi^2}{3\hbar c} N_0^2 \rho_A \rho (J+1) P(J) \langle J|\mu^A|J'\rangle \\ &\quad \times \int_0^\infty \mu^I_{jj'} g(V) dV. \end{aligned} \tag{5.8}$$

Recalling the expression for the *allowed* intensity,

$$\int \frac{\alpha^{A}(\omega)}{\omega} d\omega = \frac{4\pi^2}{3\hbar c} N_0 \rho_A (J+1) P(J) \langle J|\mu^A|J'\rangle^2 \tag{5.9}$$

and substituting these two equations into Equation 5.7, we have,

$$a = \frac{2N_0 \int_0^\infty \mu^I_{jj'}(R) g(V) dV}{\langle J|\mu^A|J'\rangle} \tag{5.10}$$

or

$$a = \frac{2N_0 \int_0^{2\pi} \int_0^{\pi} \int_0^\infty \mu^I_{jj'}(R) g(R) R^2 \sin\theta d\varphi d\theta dR}{\langle J|\mu^A|J'\rangle}. \tag{5.11}$$

In Equation 5.11, $\mu^I_{jj'}(R)$ is the induced dipole component with the same symmetry as the allowed dipole component and $g(R)$ is the pair correlation function.

In classical statistical mechanics, it is expressed to the zeroth order as [52][123]

$$g(R) = \exp\left[-\beta V(R)\right], \tag{5.12}$$

where $\beta = (kT)^{-1}$, $V(R)$ is the intermolecular pair potential and R is the intermolecular separation.

There are a number of semiempirical calculations available for the $H_2 - H_2$ and $H_2 - X$ intermolecular potential but not for the $HD - HD$ or $HD - X$ system. Considering the difference between the HD and H_2 molecules, as was described in chapter 2, we calculated the intermolecular potential for HD to perturber molecule by carrying out a coordinate transformation. To the first order approximation,

$$\begin{aligned} V_{HD-X}(R) &= [1 + \vec{d} \cdot \nabla_R] V_{H_2-X}(R) \\ &= V_{H_2-X}(R) + (r_e/6) V'_{H_2-X}(R) \cos\theta, \end{aligned} \tag{5.13}$$

where r_e is the equilibrium internuclear separation of HD, θ is the angle between the internuclear axis of HD (from H to D) and the intermolecular distance R (from the centre of the mass of HD to that of perturber molecule). $V_{H_2-X}(R)$ is the potential for $H_2 - H_2$ or $H_2 - X$ (Norman *et al.*) [110] and $V'_{H_2-X}(R)$ is the first derivative of $V_{H_2-X}(R)$ with respect to R.

Applying Equations 5.12 and 5.13 to the integral in Equation 5.11, and carrying out the integral over φ and θ, one obtains the following expression for a,

$$a = \frac{8\pi N_0}{\langle J|\mu^A|J'\rangle} \int_0^\infty \mu^I_{jj'} \exp\left[-V_{H_2-X}(R)\beta\right]$$

$$\times\{\frac{\sinh[V'_{H_2-X}(R)\beta r_e/6]}{V'_{H_2-X}\beta r_e/6}\}R^2dR. \tag{5.14}$$

As was described in chapter 2, the allowed dipole component has the symmetry of $A_1(100;r)$. Therefore, only if $\mu^I_{jj'}(R)$ has the same symmetry can it contribute to the intracollisional interference. Namely, $\mu^I_{jj'}$ in Equation 5.14 must have the symmetry of $A_1(100;r_1,r_2,R)$;

$$\mu^I_{jj'}(R) = \langle J|A_1(100;r_1,r_2,R)|J'\rangle, \tag{5.15}$$

where r_1 and r_2 denote the internuclear distances of molecule 1 and 2, and R is the intermolecular distance between the centres of mass.

Similarly, as in the calculation of the intermolecular potential, the coordinate transformation is applied to the case where only H_2 data are available.

From the general form, as was introduced in chapter 2, the relationship between the induced dipole component for HD with a perturber atom and that of H_2 with a perturber atom is given by

$$\begin{aligned}
&A^{HD-X}_{\lambda}(l\lambda_2 L+\gamma;r_1,r_2,R)\\
&= (r_e/6)[O^L_\gamma A^{H_2-X}_\Lambda(\lambda_1\lambda_2 L;r_1,r_2,R)](-1)^{L+\lambda-1}\\
&\quad\times[(2\lambda_1+1)(2\Lambda+1)(2L+1)(2\lambda+1)]^{\frac{1}{2}}C(1\lambda_1 l;00)\\
&\quad\times C(1lL+\gamma;00)W(1l\Lambda\lambda_2;\lambda_1\lambda)W(L+\gamma L\lambda\Lambda;11)
\end{aligned} \tag{5.16}$$

with

$$O_{\gamma}^{L} = \begin{cases} d/dR - L/R & \gamma = +1 \\ d/dR + (L+1)/R & \gamma = -1. \end{cases} \tag{5.17}$$

Taking $\lambda = 1$, $l = 1$, $\lambda_2 = 0$ and $L + \gamma = 0$ yields $A_1^{HD-X}(100; R)$ on the left hand of Equation 5.16, and applying the further restrictions on Λ, l, λ_1, λ_2, L and γ, as were mentioned in chapter 2, one finds that only the following two combinations are allowed for these parameters

$$\begin{cases} \lambda_1 = 0 \\ \lambda_2 = 0 \\ \Lambda = 0 \\ L = 1 \\ \gamma = -1 \end{cases} \tag{5.18}$$

and

$$\begin{cases} \lambda_1 = 2 \\ \lambda_2 = 0 \\ \Lambda = 2 \\ L = 1 \\ \gamma = -1 \end{cases} \tag{5.19}$$

Substituting the above two sets of parameters into the right hand side of Equation 5.16, one finally obtains the expression for $A_1^{HD-X}(100; R)$ in terms of $A_{\lambda}^{H_2-X}(\lambda_1\lambda_2 L; R)$, namely,

$$A_1^{HD-X}(100; R) = (r_e/18)(\frac{d}{dR} + \frac{2}{R})[A_0^{H_2-X}(001; R) - \sqrt{2}A_2^{H_2-X}(201; R)]. \tag{5.20}$$

Assuming the J-dependence is neglible [69], combining Equation 5.15 with

Equation 5.20 yields the following expression for the induced dipole moment,

$$\mu^I(R) = (r_e/18)(\frac{d}{dR} + \frac{2}{R})[A_0^{H_2-X}(001;R) - \sqrt{2}A_2^{H_2-X}(201;R)]. \qquad (5.21)$$

Up to this point in the calculations of a, the collisional mixing of rotational levels, as described in chapter 2, has been ignored. To calculate this additional contribution to the intracollisional interference of $R(0)$, we apply the same potential and pair correlation function from the calculations of a. Making use of Equations 2.111, 2.112 and 5.7, one obtains the following expression for Δa,

$$\begin{aligned}\Delta a &= \frac{N_0}{\langle J|\mu^A|J'\rangle\sqrt{2}B_0}\int_0^{2\pi}\int_0^{\pi}\int_0^{\infty} A_2^{HD-X}(201;R)(r_e/6)V'_{H_2-X}\cos\theta \\ &\quad \times \exp\left[-\beta V_{H_2-X}(R) - (r_e/6)\beta V'_{H_2-X}(R)\cos\theta\right]\sin\theta R^2 d\varphi d\theta dR\ ,\end{aligned} \qquad (5.22)$$

or

$$\Delta a = \frac{2\pi N_0}{\langle J|\mu^A|J'\rangle\sqrt{2}B_0}\int_0^{\infty} A_2^{HD-X}(201;R)\exp\left[-\beta V_{H_2-X}(R)\right]I'R^2dR, \qquad (5.23)$$

with

$$I' = \int_0^{\pi}(r_e/6)V'_{H_2-X}(R)\cos\theta\exp\left[-(r_e/6)\beta V'_{H_2-X}(R)\cos\theta\right]\sin\theta d\theta. \qquad (5.24)$$

This is easily integrated by parts to give

$$I' = \frac{2[1-(r_e/6)\beta V'_{H_2-X}(R)]}{\beta[(r_e/6)\beta V'_{H_2-X}(R)]}\sinh\left[(r_e/6)\beta V'_{H_2-X}(R)\right]. \qquad (5.25)$$

Finally, Δa is expressed as

$$\Delta a = \frac{4\pi N_0}{\langle J|\mu^A|J'\rangle\sqrt{2}B_0\beta}\int_0^\infty A_2^{HD-X}(201;R)\exp\left[-\beta V_{H_2-X}(R)\right] \times\frac{[1-(r_e/6)\beta V'_{H_2-X}(R)]}{(r_e/6)\beta V'_{H_2-X}(R)}\sinh\left[(r_e/6)\beta V'_{H_2-X}(R)\right]R^2dR. \quad (5.26)$$

Because of the nature of the perturbation theory, the integral in Equation 5.26 can not be taken to small R and it must be cut off so that the first order wavefunction (*c.f.* Equation 2.110) remains accurate [52]. In accord with the theory of Herman *et al.*, it is assumed that the maximum amount of intensity that can be borrowed from a transition starting at level J is equal to the intensity in the transition in the absence of anisotropic interactions [109]. Namely, in the above integral, R should satisfy [52]

$$A_1^{HD-X}(100;R) \geq \frac{f(J)}{2\sqrt{2}B_0}(r_e/6)V'_{H_2-X}A_2^{HD-X}(201;R), \quad (5.27)$$

where

$$f(J) = \frac{1}{2J+3} \quad (5.28)$$

and

$$J = 0. \quad (5.29)$$

In the numerical evaluations of a and Δa, $r_e = 0.76318$ $\AA$ or 1.4422 a_0 [5]. Values of $A_\Lambda(\lambda_1\lambda_2 L;R)$ used are from the *ab initio* calculations of Borysow, Fromnhold and Meyer [69]. They calculated the induced dipole moment component of HD−X by using *ab initio* induced dipole data for H_2−X, through the

coordinate transformation correct to all orders. The accuracy of the calculated induced dipole data was stated within 2% at the experimentally significant separations ($2.1 - 4.3$ $\mathring{A}$). The analytical expression of $A_\Lambda(\lambda_1\lambda_2 L; R)$ for the systems of $HD - HD$, $HD - H_2$, $HD - He$ and $HD - Ar$ is given in the following form,

$$A_\Lambda(\lambda_1\lambda_2 L; R) = Ae^{B(R-R_0)+C(R-R_0)^2} + \frac{C_7}{R^7} + \frac{C_8}{R^8} \quad . \tag{5.30}$$

For $HD - Kr$, only the strength of the induced dipole $A_0^{H_2-Kr}(001; R)$ in the translational band of $H_2 - Kr$ has been semiempirically calculated by Poll and Hunt [73] assuming the form,

$$A_0^{H_2-Kr}(001; R) = Ae^{B(R-R_0)} \quad . \tag{5.31}$$

Therefore Equation 5.21 was only applied for $HD - Kr$.

The intermolecular potential used in the computations were different in each case. For $HD - HD$ and $HD - H_2$, a Hartree-Fock dispersion type potential was used [110],

$$V_{H_2-H_2}(R) = A\exp(-a_1R - a_2R^2) - (\frac{C_6}{R^6} + \frac{C_8}{R^8} + \frac{C_{10}}{R^{10}})D(R), \tag{5.32}$$

with

$$D(R) = \begin{cases} \exp[-(R_1/R-1)^2] & R < R_1 \\ 1 & R \geq R_1. \end{cases} \tag{5.33}$$

For $HD - He$, an *ab initio* potential was employed [111][112],

$$V_{H_2-He}(R) = A\exp(13.335 - a_1R - a_2R^2) - (\frac{C_6}{R^6} + \frac{C_8}{R^8} + \frac{C_{10}}{R^{10}})D(R), \quad (5.34)$$

with

$$D(R) = \begin{cases} 1 - \exp[-0.889(R - R_1)] & R > R_1 \\ 0 & R \leq R_1. \end{cases} \quad (5.35)$$

For $HD - Ar$ and $HD - Kr$, we used the Buckingham-Corner semiempirical potential given by [113][114].

$$V_{H_2-X}(R) = A\exp(-a_1R) - (\frac{C_6}{R^6} + \frac{C_8}{R^8})D(R) \quad , \quad (5.36)$$

with

$$D(R) = \begin{cases} \exp[-4(R_1/R - 1)^3] & R > R_1 \\ 1 & R \leq R_1. \end{cases} \quad (5.37)$$

The parameters of the induced dipole component are listed in Table 5.1, and the intermolecular potential parameters are collected in Table 5.2.

The numerical results for a and Δa at 77 K, 195 K and 296 K for the various systems (for which the necessary data for such calculation are available) are presented in Table 5.3. Also given are the calculations of $\Delta a'$ (see chapter 2) for $HD-HD$ made by Ma *et al.* [53], in which the near-resonance rotational-level mixing mechanism was considered for R(2) and R(3).

Table 5.1: Parameters of the induced dipole component used in the calculations of a and Δa

			$A_1(100;R)$		
Parameter	HD-HD[a]	HD-H_2[a]	HD-He[a]	HD-Ar[a]	H_2-Kr[b]
$R_0(a_0)$	+6.00	+6.00	+5.70	+6.00	+6.16
$A(10^{-3}ea_0)$	−0.094675	−0.087018	−0.35317	−0.62200	6.295
$B(a_0^{-1})$	−1.568660	−1.611988	−1.480215	−1.734827	−1.476
$C(a_0^{-2})$	−0.033502	−0.058241	−0.010277	−0.134086	0
$C_7(ea_0^8)$	+21.078145	+23.815393	+12.776708	+4.951582	0
$C_8(ea_0^9)$	−61.223719	−75.179287	0	0	0

			$A_2(201;R)$		
Parameter	HD-HD[a]	HD-H_2[a]	HD-He[a]	HD-Ar[a]	H_2-Kr[b]
$R_0(a_0)$	+6.00	+6.00	+5.70	+6.00	–
$A(10^{-3}ea_0)$	−0.32725	−0.34375	−0.36835	−1.5901	–
$B(a_0^{-1})$	−1.817194	−1.781377	−1.725920	−1.573635	–
$C(a_0^{-2})$	−0.091933	−0.075904	−0.042242	+0.028285	–
$C_7(ea_0^8)$	−46.526417	−27.868561	−5.663447	+1.718736	–
$C_8(ea_0^9)$	+11.918610	−3.649204	0	0	–

a: Reference [69].

b: Reference [73], the sign of A for $H_2 - Kr$ is unknown.

Table 5.2: Parameters of the intermolecular potential used in the calculations of a and Δa.

Parameter	$H_2 - H_2^{a}$	$H_2 - He^{b}$	$H_2 - Ar^{c}$	$H_2 - Kr^{c}$
$A(10^7 K)$	0.118	3.2×10^{-7}	4.108	3.732
$a_1(\mathring{A}^{-1})$	2.78	2.957	3.692	3.462
$a_2(\mathring{A}^{-2})$	0.08	0.183	0	0
$C_6(10^5 K\mathring{A}^6)$	0.84	0.309	1.963	2.794
$C_8(10^6 K\mathring{A}^8)$	0.417	0.109	1.474	2.728
$C_{10}(10^6 K\mathring{A}^{10})$	2.607	0.535	0	0
$R_1(\mathring{A})$	5.10	1.571	3.574	3.719

a: Reference [110].

b: References [111] and [112].

c: Reference [113].

Table 5.3: Calculated interference parameters a and Δa (10^{-3} $amagat^{-1}$).

Sample	T (K)	Parameter	R(0)	R(1)	R(2)	R(3)
$HD-HD$	77	a	+1.04	+1.04	+1.04	–
		Δa	+0.29	0	0	–
		$\Delta a'$	0	0	−3.4	–
		a_{theory}	+1.33	+1.04	−2.36	–
	195	a	+1.48	+1.48	+1.48	+1.48
		Δa	+0.64	0	0	0
		$\Delta a'$	0	0	−3.1	−0.2
		a_{theory}	+2.12	+1.48	−1.62	+1.28
	296	a	+1.86	+1.86	+1.86	+1.86
		Δa	+0.93	0	0	0
		$\Delta a'$	0	0	−3.2	−0.2
		a_{theory}	+2.79	+1.86	−1.34	+1.66
$HD-H_2$	77	a	+0.73	+0.73	+0.73	–
		Δa	+0.32	0	0	–
		a_{theory}	+1.05	+0.73	+0.73	–
	195	a	+1.17	+1.17	+1.17	+1.17
		Δa	+0.68	0	0	0
		a_{theory}	+1.85	+1.17	+1.17	1.17
	296	a	+1.52	+1.52	+1.52	+1.52
		Δa	+0.99	0	0	0
		a_{theory}	+2.51	+1.52	+1.52	+1.52

a: Equation 5.14.

Δa: Equation 5.26. The R_{cut} equals 3.880 $\AA$ and 3.742 $\AA$ for $HD-HD$ and $HD-H_2$ respectively.

$\Delta a'$: Reference [53].

a_{theory}: $a+\Delta a+\Delta a'$.

Table 5.4: Calculated interference parameters a and Δa (10^{-3} $amagat^{-1}$).

Sample	T (K)	Parameter	R(0)	R(1)	R(2)	R(3)
$HD-He$	77	a	+4.46	+4.46	+4.46	–
		Δa	+0.03	0	0	–
		a_{theory}	+4.49	+4.46	+4.46	–
	195	a	+6.18	+6.18	+6.18	+6.18
		Δa	+0.09	0	0	0
		a_{theory}	+6.27	+6.18	+6.18	+6.18
	296	a	+7.36	+7.36	+7.36	+7.36
		Δa	+0.13	0	0	0
		a_{theory}	+7.49	+7.36	+7.36	+7.36
$HD-Ar$	195	a	+8.83	+8.83	+8.83	+8.83
		Δa	+0.46	0	0	0
		a_{theory}	+9.29	+8.83	+8.83	+8.83
	296	a	+9.49	+9.49	+9.49	+9.49
		Δa	+0.68	0	0	0
		a_{theory}	+10.17	+9.49	+9.49	+9.49
$HD-Kr$	195	a	11.5	11.5	11.5	11.5
		a_{theory}	11.5	11.5	11.5	11.5
	296	a	11.66	11.66	11.66	11.66
		a_{theory}	11.66	11.66	11.66	11.66

a: Equation 5.14.

Δa: Equation 5.26. The R_{cut} for $HD-He$ and $HD-Ar$ are, respectively, 4.684 $\mathring{A}$ and 4.723 $\mathring{A}$.

a_{theory}: $a+\Delta a$. The sign for $HD-Kr$ is unknown.

5.2 Calculations of Line Broadening

The theory developed by Robert and Bonamy is semiclassical within the framework of the impact theory [105]. It has been applied with success in the calculations for Raman and infrared P and Q branches for linear molecules perturbed by atoms or linear molecules, such as CO−Ar and CO−CO [105][107][115]. The main features of the theory may be summarized as follows,

1. The geometry of the collision is described through so-called *equivalent* straight path, that is, a parabolic trajectory model determined by the isotropic part of the interaction potential which allows a satisfactory treatment to be made of the close collisions. This treatment is more appropriate than the usual one which is a straight line trajectory at constant velocity [105][116].

2. In the extension to diatom-diatom collisions, the anisotropic potential is expressed by an atom-atom model which takes both the long and short range contributions into account without any adjustable parameters [105][117][118].

3. The matrix elements of the relaxation operator are computed by means of the linked-cluster theroem, so that the treatment remains nonperturbative and no cut off procedure is needed [105][107].

The general expression for the half width at half intensity γ_H (HWHM) is given by [107]

$$\begin{aligned} \gamma_H &\equiv \frac{N_b}{2\pi c} < v\sigma >_{b,v,j} \\ &= \frac{N_b}{2\pi c} Re[\sum_{v_2,j_2} \rho_{v_2,j_2} \int_0^\infty v f(v) dv \int_0^\infty 2\pi b S(b,v) db], \end{aligned} \tag{5.38}$$

where N_b is the perturber density, v is the relative velocity, and b is the impact parameter. The subscript 2 of the quantum numbers denotes the perturber, and so ρ_{v_2,j_2} is the probability density that the perturber is in $|v_2 j_2\rangle$ state. $S(b,v)$, the collision efficiency function or the differential cross section function [119], is expressed through the linked-cluster theorem as a product of a *linked* term and of an exponential of the *connected* term [105],

$$S(b,v) = 1 - [1 - S_2^{(L)}]e^{-S_2}(\cos\Omega - i\sin\Omega), \tag{5.39}$$

with

$$\begin{aligned} S_2 &= S_{2,f2} + S_{2,i2} + S^{(c)}_{2,f2,i2}, & (5.40)\\ \Omega &= (S_{1,f2} + S'_{2,f2}) - (S_{1,i2} + S'_{2,i2}), & (5.41)\\ S_2^{(L)} &= \sum_{v'_2,j'_2} S_{2,f2,i2}(1 - \delta_{v'_2,v_2}\delta_{j'_2,j_2}), & (5.42) \end{aligned}$$

and

$$S^{(c)}_{2,f2,i2} = \sum_{v'_2,j'_2} S_{2,f'2,i'2}\delta_{v'_2,v_2}\delta_{j'_2,j_2}\ . \tag{5.43}$$

Here the subscripts 1 and 2 of S denote the first and second order contribution; i and f denote the initial and final state with vibrational and rotational quantum number vj and $v'j'$ respectively. The explicit expressions for $S(b,v)$ were calculated using an osculating parabolic trajectory [105]. In this model, the encounter

of the collision pair is described by

$$\vec{r}(t) \cong \vec{r}_c + \vec{v}_c t + \frac{\vec{F}_c t^2}{2m}, \tag{5.44}$$

where $\vec{v}_c$ is the relative velocity at the closest approach and $\vec{F}_c$ is defined by

$$\begin{aligned} \vec{F}_c &= -(\frac{\partial V_{ISO}}{\partial r})_{r=r_c}\frac{\vec{r}_c}{r_c} \\ &= -\frac{\partial}{\partial r}\{4\epsilon[(\frac{\sigma}{r})^{12} - (\frac{\sigma}{r})^6]\}_{r=r_c}\frac{\vec{r}_c}{r_c} \\ &= \frac{24\epsilon}{\sigma}[2(\frac{\sigma}{r_c})^{13} - (\frac{\sigma}{r_c})^7]\frac{\vec{r}_c}{r_c} \ . \end{aligned} \tag{5.45}$$

Here a *Lennard-Jones* (6-12) potential is taken as V_{ISO}. The apparent velocity v_c' is defined by

$$v_c'^2 = v_c^2 + \frac{\vec{F}_c \cdot \vec{r}_c}{m} \ . \tag{5.46}$$

With this expression, the $r(t)$ modulus is written as

$$r(t) = [r_c^2 + v_c'^2 t^2]^{1/2} \ . \tag{5.47}$$

From the equation for conservation of energy and angular momentum at $r = r_c$, one has

$$\frac{1}{2}mv^2 = \frac{1}{2}mv_c^2 + 4\epsilon[(\frac{\sigma}{r_c})^{12} - (\frac{\sigma}{r_c})^6] \tag{5.48}$$

and

$$bv = r_c v_c \ . \tag{5.49}$$

Combining above equations with Equation 5.45 and Equation 5.46, one obtains

$$b = r_c\{1 - \frac{8\epsilon}{mv^2}[(\frac{\sigma}{r_c})^{12} - (\frac{\sigma}{r_c})^6]\}^{1/2} \tag{5.50}$$

and

$$\frac{v_c}{v_c'} = \{\frac{1 - (8\epsilon/mv^2)[(\sigma/r_c)^{12} - (\sigma/r_c)^6]}{1 + (8\epsilon/mv^2)[5(\sigma/r_c)^{12} - 2(\sigma/r_c)^6]}\}^{1/2}. \tag{5.51}$$

Note that the above expressions, coming from the parabolic trajectory model, result in the function $S(b, v)$ being properly expressed in terms of b and v through r_c and v_c'; also the area element $2\pi b\ db$ is

$$2\pi b\ db = 2\pi\sigma\{\frac{r_c}{\sigma} - \frac{8\epsilon}{v^2}[2(\frac{\sigma}{r_c})^5 - 5(\frac{\sigma}{r_c})^{11}]\}\ dr_c\ . \tag{5.52}$$

Since r_c is well defined, the conventional requirement for the previous treatments of introducing a cut-off procedure in order to avoid a divergence for small values of the impact parameter b is dismissed.

The intermolecular potential used was an *atomic* site model which was considered the most suitable potential model for this type of calculations [105][115]. This model describes the molecular interaction as the superposition of *atom-atom* interactions in the collision pair

$$V = \sum_{i,j}(\frac{d_{ij}}{r_{1i,2j}^{12}} - \frac{e_{ij}}{r_{1i2j}^{6}}) + V_{\mu_1\mu_2} + V_{\mu_1 Q_2} + \cdots, \tag{5.53}$$

where the indices i and j refer to the i th atom of molecule 1 and the j th atom of molecule 2, $r_{1i,2j}$ is the distance between these two atoms, d_{ij} and e_{ij}

are the atomic pair energy parameters, and μ and Q are the permanent dipole and quadrupole moment, respectively, of the colliding molecules. On expansion of $r_{1i,2j}$ in the a series in the intermolecular distance r, the intermolecular potential may be expressed in the more convenient form [105]

$$V = 4\pi \sum_{l_1 l_2} \sum_{m} U_{l_1 l_2 m}(r) Y_{l_1,m}(\theta_1, \phi_1) Y_{l_2,-m}(\theta_2, \phi_2), \tag{5.54}$$

where θ and ϕ define the orientation of the two interacting molecules. The function $S(r_c, v_c')$ then is expressed as a sum of direct components coming from each term of the intermolecular potential and of crossed components between the terms of the same harmonic order [106]. The detailed expressions for $U_{l_1 l_2 m}(r)$ and $S(r_c, v_c')$ can be found in the appendix of Reference [105].

In the case of $HD - X$, for the pure rotational lines, the quantum numbers v_1, v_1' and v_2 v_2' are zero. In $HD - atom$ systems, there are no rotational levels of the perturber involved. Furthermore, even for those perturber molecules which involve rotational levels, the $S^{(L)}_{2,f2,i2}$ contribution, resulting from non-diagonality is negligible [107]. If we neglect the imaginary part of the differential cross section, as is frequently adopted in line broadening calculations [107], we have a simplified form for Equation 5.38,

$$\gamma_H = \frac{N_b}{2\pi c} \bar{v} \sum_{j_2} \rho_{j_2} \int_0^\infty 2\pi b (1 - e^{\zeta_2(b,\bar{v})}) db, \tag{5.55}$$

where $\bar{v}$ is the mean velocity from Maxwell distribution and

$$\zeta_2(b, v) = S_{2,f2} + S_{2,i2} + S^{(c)}_{2,f2,i2}. \tag{5.56}$$

In the calculations of the intermolecular potential for $HD - HD$ or $HD - X$, only atom-atom contributions are of importance. The pair energy parameters d_{ij} and e_{ij} and the *Lennard-Jones* parameters for the collision pair were evaluated through the usual combination rules [81][120],

$$\epsilon_{12} = (\epsilon_1 \epsilon_2)^{1/2}, \tag{5.57}$$

$$\sigma_{12} = (\sigma_1 + \sigma_2)/2, \tag{5.58}$$

$$e_{12} = (e_1 e_2)^{1/2}, \tag{5.59}$$

$$d_{12} = e_{12}(\sigma_{12})^6, \tag{5.60}$$

where e_i was obtained from the atomic $Lennard - Jones$ parameters ϵ_i and σ_i by [105]

$$e_i = \epsilon_i \sigma_i^6, \tag{5.61}$$

$$d_i = e_i \sigma_i^6 \ . \tag{5.62}$$

The computation program used was the code of Bonamy originally for CO-Ar, with modification to suit our cases. The important parameters used in the calculations are listed in Table 5.5 and the results of HWHM from numerical calculations are presented in Table 5.6 together with the experimental HWHM broadening coefficients ($B_{0H} = \frac{1}{2} B_0$).

Table 5.5: Parameters used in the line broadening calculations

Sample	σ_{12} $(\mathring{A})$	ϵ_{12}/k (K)	e_{ij} $(10^{-12} erg \mathring{A}^6)$	d_{ij} $(10^{-8} erg \mathring{A}^{12})$	B_{01} (cm^{-1})	B_{02} (cm^{-1})
$HD - HD$[a]	2.96	36.4	3.37	0.225	44.66	44.66
$HD - H_2$	2.96	36.4	3.37	0.225	44.66	44.66
$HD - He$[b]	2.75	19.27	1.14	0.05	44.66	0.0
$HD - Ne$[b]	2.87	33.7	2.70	0.15	44.66	0.0
$HD - Ar$[b]	3.27	66.09	9.64	1.03	44.66	0.0
$HD - Kr$[b]	3.28	79.0	12.2	1.5	44.66	0.0
$HD - N_2$[b]	3.30	57.66	10.3	1.38	44.66	2.0

a: deduced from L-J potential parameters taken from Reference [108].

b: deduced from L-J potential parameters from the average value of Reference [121].

Table 5.6: Calculated and experimental values of HWHM broadening coefficients B_{0H} $(10^{-2} cm^{-1} amagat^{-1})$.

Sample	T	R(0)		R(1)		R(2)		R(3)	
	(K)	Exp.	Cal.	Exp.	Cal.	Exp.	Cal.	Exp.	Cal.
$HD-HD$	77	0.27	0.85	0.44	0.58	0.41	0.29		
	195	0.90	2.1	0.81	1.6	0.75	1.2	0.62	0.7
	296	1.7	3.1	1.3	2.5	1.1	1.9	0.90	1.4
$HD-H_2$	77	0.29	0.82	0.40	0.55	0.32	0.29		
	195	0.90	2.0	0.76	1.6	0.78	1.2	0.65	0.7
	296			1.1	2.5	0.95	1.9	1.0	1.4
$HD-He$	77	0.15	0.61	0.20	0.41	0.12	0.19		
	195	0.52	1.7	0.51	1.3	0.41	0.91	0.38	0.55
	296			1.1	2.0	0.63	1.6	0.59	1.1
$HD-Ne$	77	0.24	0.80	0.33	0.51	0.18	0.21		
	195	0.80	1.8	0.61	1.4	0.52	0.88	0.48	0.47
	296			0.84	2.1	0.75	1.5	0.34	.98
$HD-Ar$	195	1.4	1.6	1.0	1.1	0.86	0.64	0.63	0.29
	296			1.5	1.8	1.1	1.2	0.68	0.67
$HD-Kr$	195	1.5	2.1	1.2	1.5	1.1	0.87	0.91	0.39
	296			1.3	2.4	0.99	1.5	0.54	0.84
$HD-N_2$	195	2.1	2.6	1.4	1.9	0.99	1.1	0.84	0.51
	296			1.4	2.8	1.4	1.9	0.68	1.1

Chapter 6

DISCUSSION

In order to reach the appropriate conclusions regarding the temperature dependence of the collisional interference in the pure rotational spectrum of HD, we will compare our experimental measurements with the published experimental results and with theoretical calculations.

In this chapter, we will first discuss the relative quality of the spectra and the accuracy of the data in our experiment. Then we will discuss the allowed dipole moment matrix element, the line shape parameters, and finally the interference parameters, within the context of the original theory.

6.1 The Relative Quality of the Spectra and the Accuracy of the Data

Before the comparisons are made, the relative quality of the spectra at different temperatures and the accuracy of the data should be assessed and then assimilated into the discussion.

As was discussed in chapter 3, the quality of the infrared absorption spectra depends on the S/N ratio, which is affected by many factors. If the optical

alignment is in the optimum condition and the water vapour along the light path is reduced to the minimum, then from the instrumental point of view, the S/N ratio is mainly affected by the radiation efficiency of the infrared source, the efficiency of the beam splitter, the transmittance of the window and of the filter, and the spectral response of the detector. The spectral lines of HD measured in the experiment are located at about $89cm^{-1}$, for $R(0)$, $178cm^{-1}$, for $R(1)$, $265cm^{-1}$, for $R(2)$ and $351cm^{-1}$, for $R(3)$. From the radiation curve of the globar source, as shown in Figure 3.3, there is roughly an order of magnitude difference in the radiation efficiency among these locations, with the weakest radiation near the $R(0)$. On the high frequency side, because of the filter of the bolometer, the spectrum is effectively cut off at $360cm^{-1}$, resulting in a sharp decrease in the spectral region of $R(3)$. The transmittance spectrum of the empty cell at 296 K, as illustrated in Figure 6.1, shows the net result of those instrumental factors.

On the other hand, the relative strength of the absorption lines is greatly affected by the thermal distribution of the population in the rotational energy levels of the sample molecules. This can be seen clearly in the calculated values of $C(J)$ listed in Table 4.3. Roughly, at 77 K, $R(0)$ is the strongest line and $R(2)$ is the weakest; at 195 K, $R(1)$ is the strongest, next is $R(0)$ and the weakest is $R(3)$; at 296 K, the strength of $R(1)$ and $R(2)$ are close while $R(0)$ is the weakest. In all cases, $R(3)$ is the most difficult to measure accurately. Due to the abundance of the water noise at low frequency, the quality of $R(0)$ is usually lower than $R(1)$ and $R(2)$ at 195 K and 296 K, and even at 77 K lower than $R(1)$. In summary, the spectral quality in terms of J dependence decreases as follows: $R(1)$, $R(0)$, $R(2)$ at 77 K; $R(2)$, $R(1)$, $R(0)$, $R(3)$ at 195 K; $R(2)$, $R(1)$,

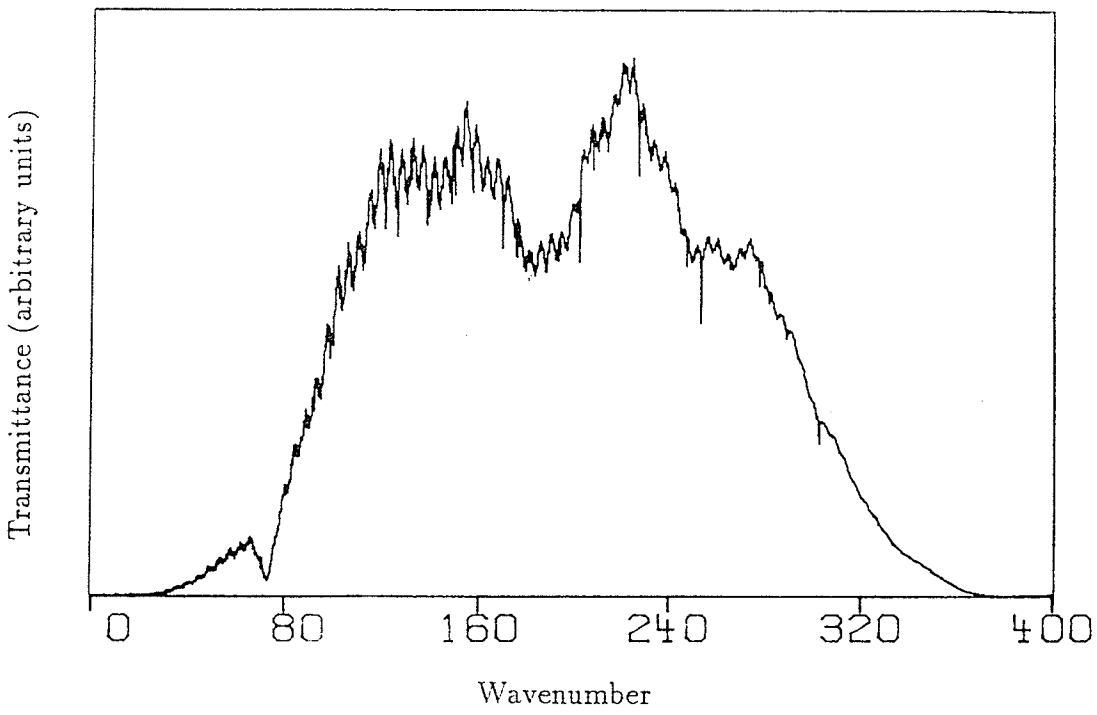

Figure 6.1: The transmittance spectrum of the empty cell at 296 K.

$R(3)$ at 296 K.

In addition, there is a spread in the experimental determinations, especially for the measurements of the integrated intensity of the spectra. Figure 4.6 shows clear evidence of such spread. At the same temperature (195 K), and the same density (3.9 *amagat*), the spread of the measured integrated absorption coefficients of HD is about $\pm 4.5\%$ for $R(0)$, $\pm 3.0\%$ for $R(1)$, $\pm 1.5\%$ for $R(2)$ and $\pm 4.7\%$ for $R(3)$. For $HD - HD$ at 77 K, the same spread is approximatly $\pm 7\%$ for R(0), $\pm 6\%$ for R(1) and $\pm 7.3\%$ for R(2). The fluctuations in the measurements of line width are slightly less but of the same order, but they are much less for the frequency shift measurements. If this type of uncertainty is due to the narrow spectra affected by the random noise, then the smaller spread is expected

at the higher densities of $HD - HD$, and to be slightly different at different temperatures. In the $HD - X$ systems, on the other hand, when the perturber density increases, the S/N ratio decreases, resulting in relatively lower quality of the spectra and larger uncertainties compared to those for $HD - HD$.

6.2 The Allowed Dipole Moment Matrix Elements

The experimental results for the allowed dipole moment matrix elements presented in Table 4.4 are the average values from the $HD - HD$ spectra at different temperatures and different experiments. With the existing theory, for example from Equation 4.14, the allowed dipole moment matrix elements can be obtained also from the $HD - X$ systems, although the statistical error may be larger for the reason mentioned in the previous section. Using Equation 4.14 and 4.15, and the *theory fitting* results, we deduced the allowed dipole matrix elements from the $HD - X$ spectra at different temperatures. The results from all systems are collected in Table 6.1.

The dipole moments in Table 6.1 are generally reasonably consistent except for $HD - He$ at 195 K, in which case we failed to remove effectively the hidden water noise, causing the intensity measurements for R(0) and R(3) to be far from accurate. Table 6.1 also reflects the fluctuations among the different experiments at different temperatures and among the different experiments at the same temperature. There is not sufficient evidence for a systematic trend with temperature at a given J. Therefore it is justified to perform a weighted average over the all measurements for a given J. It is obvious that the results from $HD - HD$ play an

Table 6.1: The magnitude of the matrix elements of the allowed dipole moment transitions of HD ($10^{-4} debye$) deduced from $HD - HD$ and $HD - X$ systems. The uncertainty appears in parentheses.

System	Temperature (K)	$\langle J\|\mu^A\|J+1\rangle$			
		$J=0$	$J=1$	$J=2$	$J=3$
$HD - HD$	77[a]	7.19(3)	7.68(4)	7.79(6)	
	195[a]	8.03(12)	8.01(4)	8.12(6)	7.84(23)
	195[b]	8.75(4)	8.09(3)	8.15(2)	8.62(15)
	296[c]	8.83(28)	7.94(2)	7.88(3)	8.43(10)
$HD - H_2$	77[a]	7.30(15)	7.93(11)	9.17(29)	
	195[b]	8.76(49)	8.32(5)	8.29(5)	8.39(15)
	296[b]		8.18(6)	8.05(6)	8.84(12)
$HD - He$	77[a]	7.35(12)	7.83(5)	8.79(13)	
	195[a]	12.2(34)	8.78(7)	8.76(7)	11.1(30)
$HD - Ne$	77[a]	7.95(9)	8.77(13)	7.44(12)	
	195[b]	8.61(10)	8.33(5)	8.25(3)	
$HD - Ar$	195[a]	7.78(8)	7.93(3)	8.18(5)	8.07(30)
	195[b]	8.73(5)	8.08(5)	7.97(7)	8.19(16)
$HD - Kr$	195[b]	8.72(4)	8.47(11)	7.96(12)	8.43(11)
	296[b]		8.11(7)	8.09(5)	9.22(13)
$HD - N_2$	195[b]	8.93(12)	8.29(9)	8.49(8)	7.91(34)
	296[b]		8.31(7)	8.12(5)	8.73(19)

a: 1987 experiment. b: 1990 experiment.

c: 1986 experiment, *c.f.* Reference [63].

important role in the averaging process because of their small errors. The dipole moments so averaged are presented in Table 6.2, together with the average results from only $HD - HD$, the experimental results of other workers and the theoretical calculations. For the average dipole moment, three standard deviations are taken as the uncertainty appearing in parentheses. Thus the average value with its uncertainty is at the 99% confidence level. Because of the reasons discussed above, we believe that the average dipole moments from both the $HD - HD$ and $HD - X$ systems are more reliable than the average values from $HD - HD$ alone. We will, therefore, take the former as the experimental result of the allowed dipole moments of this laboratory for comparison and discussion.

Our results in Table 6.2 agree very well with McKellar for the value of R(0), R(1) and R(2), and with Essenwenger for the value of R(3). For R(3), the coefficient of $C(J)$ at room temperature is about 1/3 smaller than $C(J)$ for R(1) and R(2); therefore, the determination of the dipole moment for R(3) is 1.7 times more sensitive to the integrated intensity compared the cases of R(1) and R(2). The measurement of Essenwenger was made at low pressure; therefore, the zero density intercept should be reliable. The dipole moments of Trefler *et al.* are significantly lower compared to the other experimental results. The reasons are believed due to the low resolution instruments used by Trefler *et al.* ($0.4cm^{-1}$), and to the fact that the results of the dipole moment were not determined from the zero density intercept [22].

Our dipole moments also agree quite well with the theoretical calculations listed in Table 6.2 in general, and are in favour of Wolniewicz's calculation in particular. Figure 6.2 shows the experimental results plotted with the theoretical calculations. Although the calculation of Ford and Brown is close to the experimental values, the J-dependence is different. We should point out that the J-dependence in our experimental result is not predicted by any of Wolniewicz, Ford and Brown, or Thorson *et al.* Within the 99% confidence error bars, the J-dependence predicted by Wolniewicz is possible, namely that the magnitude of the allowed dipole moment increases with increasing of J, while the the opposite direction in J dependence seems to be ruled out. If the J dependence can be represented by [124]

$$\mu^A = \mu_0^A + \delta(J+1)^2, \tag{6.1}$$

our experimental results yield

$$\mu^A = [8.015 + 0.016(J+1)^2] \times 10^{-4} D, \tag{6.2}$$

as illustrated by the dotted line in Figure 6.2. Neglecting the J dependence, one obtains an average dipole moment, $(8.11 \pm 0.14) \times 10^{-4} D$, 3% low with respect to the averaged value of the theoretical calculations.

It is interesting to note that although the magnitudes of the dipole moments obtained by Trefler *et al.* are far lower than ours, the J dependence is similar.

Table 6.2: The allowed dipole moment transitions of HD ($10^{-4} debye$). Uncertainty appearing in parentheses for *present work* is three standard deviations.

Reference	$\langle J\|\mu^A\|J+1\rangle$			
	$J=0$	$J=1$	$J=2$	$J=3$
	Experiment			
Present work[a]	**8.10(15)**	**8.04(12)**	**8.13(12)**	**8.55(42)**
Present work[b]	7.77(12)	7.95(12)	8.05(12)	8.41(40)
Trefler et al.[c]	5.42	5.52	6.18	6.41
Essenwenger and Gush[d]				8.47(9)
McKellar[e]		7.5(4)	7.8(4)	7.4(4)
McKellar et al.[f]	8.18(26)	7.9(4)		
	Calculations			
Wolniewicz[g]	8.36	8.38	8.39	8.41
Ford and Browne[h]	8.31	8.30	8.28	8.26
Thorson et al.[i]	8.463	8.455	8.440	8.420
Bishop and Cheung[j]	8.65			

a: averaged over $HD-HD$ and $HD-X$ spectra.

b: averaged over $HD-HD$ spectrum only.

c: Reference [22]. d: Reference [47].

e: Reference [56]. f: Reference [50].

g: Reference [38]. h: Reference [39].

i: Reference [42]. j: Reference [40].

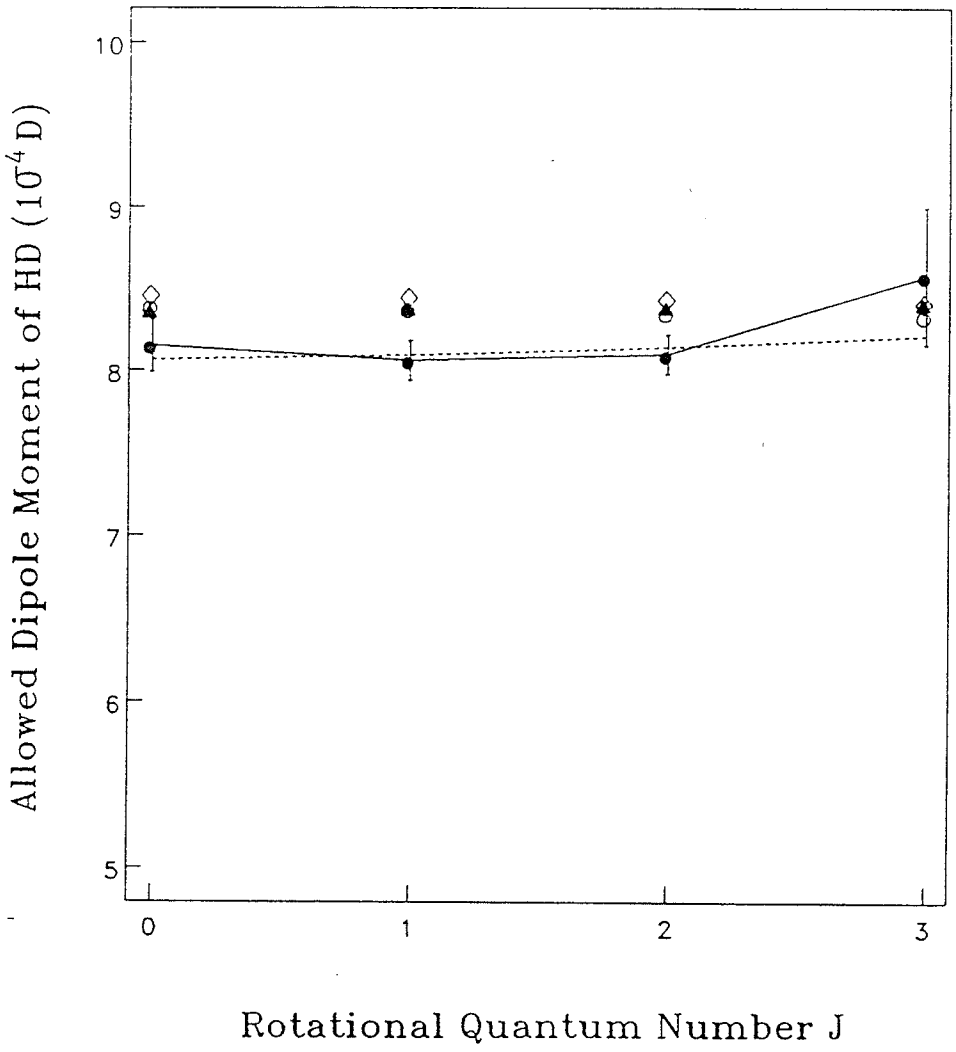

Figure 6.2: Comparision of our experimental results with theoretical calculations. The dotted line represents Equation 6.2.

•: experimental.

o: Reference [39].

◇: Reference [42].

▲: Reference [38].

6.3 Line Shape Parameters

6.3.1 Broadening Coefficient

There is a general tendency in the experimental FWHM broadening coefficients, as shown in Table 4.9. That is, generally, B_0 decreases with increasing J for all temperatures and systems (except for R(0) at 77 K), and increases with increasing temperature at all J for all systems (except for R(3) at 296 K for several systems). The reason behind the tendency is the fact that, as J increases, the energy gap between the rotational energy level E(J) and E(J+1) increases, thereby reducing the efficiency of inelastic transitions between adjacent levels, giving rise to longer coherence times, and hence resulting in the decreasing of the line shape cross section and consequently the broadening coefficient. On the other hand, generally, when the temperature increases, the relative velocity of the molecules increases, thereby increasing the frequency of collision between absorber and perturber molecules, resulting in the increase of the broadening coefficient. The impact theory suggests a simple power law describing the temperature dependence of the line width [4][107]:

$$\gamma_{0H}(T) = \gamma_{0H}(T_{ref})(T/T_{ref})^N, \tag{6.3}$$

where γ_{0H} is the HWHM, T is the temperature and T_{ref} is the reference temperature. If this is true, the broadening coefficient should obey the same rule,

$$B_0(T) = B_0(T_{ref})(T/T_{ref})^N. \tag{6.4}$$

Table 6.3: N deduced from experimental broadening coefficients. Uncertainty appears in parentheses.

System	T (K)	N			
		$R(0)$	$R(1)$	$R(2)$	$R(3)$
		$T_{ref} = 77\ K$			
$HD - HD$	195	1.31(6)	0.65(1)	0.68(4)	–
	296	1.34(7)	0.78(4)	0.74(1)	–
$HD - H_2$	195		0.71(8)	0.96(10)	–
	296		0.78(2)	0.82(7)	–
$HD - He$	195		1.02(5)	1.31(13)	–
	296		1.26(4)	1.29(9)	–
$HD - Ne$	195		0.66(3)	1.12(22)	–
	296		0.69(3)	1.05(17)	–

The exponent N deduced from the experimental broadening coefficients in Table 4.9 are presented in Table 6.3.

The exponents in Table 6.4 for all systems are, in general, reasonably consistent within their uncertainties at different temperatures for a given R(J) and system. This fact may provide evidence of the validity of the simple power law to describe the temperature dependence of line width to some degree. However, only three temperatures are involved and such a generalization may not be appropriate.

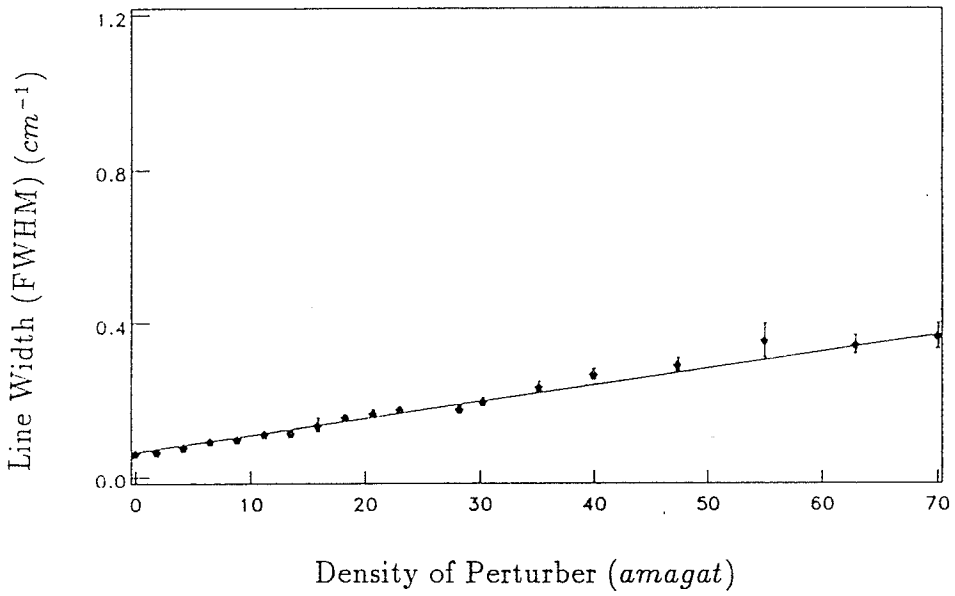

Figure 6.3: Line width ($10^{-2}cm^{-1}amagat^{-1}$) of R(0) for $HD - Ne$ at 77 K as a function of density. Points are experimental. The solid line is the fitted curve.

A comparison of our experimental broadening coefficient with published experimental results at low temperature is only available for R(0) and R(1) for $HD - HD$, and R(0) for Ne at 77 K. These results are collected in Table 6.4 together with the B_{0H} for $HD - HD$ at 296 K (for the convenience, we use B_{0H} instead of B_0 in the following discussion). There is generally a good agreement among various laboratories. The results of McKellar *et al.* at 77 K are systematically about 11% larger than ours. Nevertheless the ratio of the broadening coefficients, R(0) and R(1) for $HD - HD$ at 77 K and of R(0) for $HD - Ne$ and for $HD - HD$, are very similar (0.619 and 0.871 from our results versus 0.604 and 0.885 from McKellar's results). This fact indicates that there is a systematic difference in the determination of broadening coefficient between the two laboratories. The reliability of our experimental results may be assessed in Figures 4.15 and 6.3.

Table 6.4: Comparison of HWHM experimental broadening coefficient B_{0H} ($10^{-2}cm^{-1}amagat^{-1}$). Uncertainty appears in parentheses.

Reference	system	T (K)	B_{0H} $R(0)$	$R(1)$	$R(2)$	$R(3)$
Present work	$HD-HD$	77	0.272(13)	0.440(3)		
	$HD-Ne$	77	0.237(7)			
1986 *experiment*[a]	$HD-HD$	296		1.265(5)	1.10(1)	0.905(15)
McKellar et al.[b]	$HD-HD$	77	0.305(10)	0.505(15)		
	$HD-Ne$	77	0.270(5)			
Essenwenger and Gush[c]	$HD-HD$	296				0.915(5)
McKellar[d]	$HD-HD$	296		1.22(1)	1.13(1)	0.995(10)

a: Reference [63].

b: Reference [50].

c: Reference [51].

d: Reference [56].

The theoretical calculation using a simplified model within a semiclassical theory developed by Bonamy and Robert, as described in chapter 5, consistently agrees with the general tendency of the J-dependence and temperature dependence of the experimental results, as illustrated in Figure 6.4 to 6.6. However, quantitatively, this calculation overestimates B_{0H} at 296 K for most systems and also overestimates low J lines for most cases. Relatively, the calculated results agree better for R(2) and R(3), and for the cases where HD is perturbed by large molecules. The source of the discrepancy is probably due to the classical trajectory approximation which may not be proper for light molecules such as HD. Morever, the decoupling between translation and rotation for the molecule HD is questionable [125]. In addition, in this simplified model, the higher order terms of the angular dependent potential, as well as the static electric contributions are neglected, while the line width is sensitive to short-range anisotropic interactions [115]. Finally, as is well known, the atom-atom potential model is incorrect at long range. This inadiquacy will affect the calculation, particularly at low temperatures.

There is an exception to the general tendency of the J-dependence in that the broadening coefficient for R(0) at 77 K for $HD - HD$, $HD - H_2$, $HD - He$ and $HD - Ne$ are all clearly lower than that for R(1) for the same systems. This can not be attributed to the experimental uncertainty because of the good quality of the R(0) spectra at 77 K and the large difference between the broadening coefficients for R(0) and R(1). However the observed anomalous behaviour is confirmed by a quantum mechanical calculation by J. Schaefer and L. Monchick [126]. They calculated the pressure broadening line shape cross section for $HD - H_2$

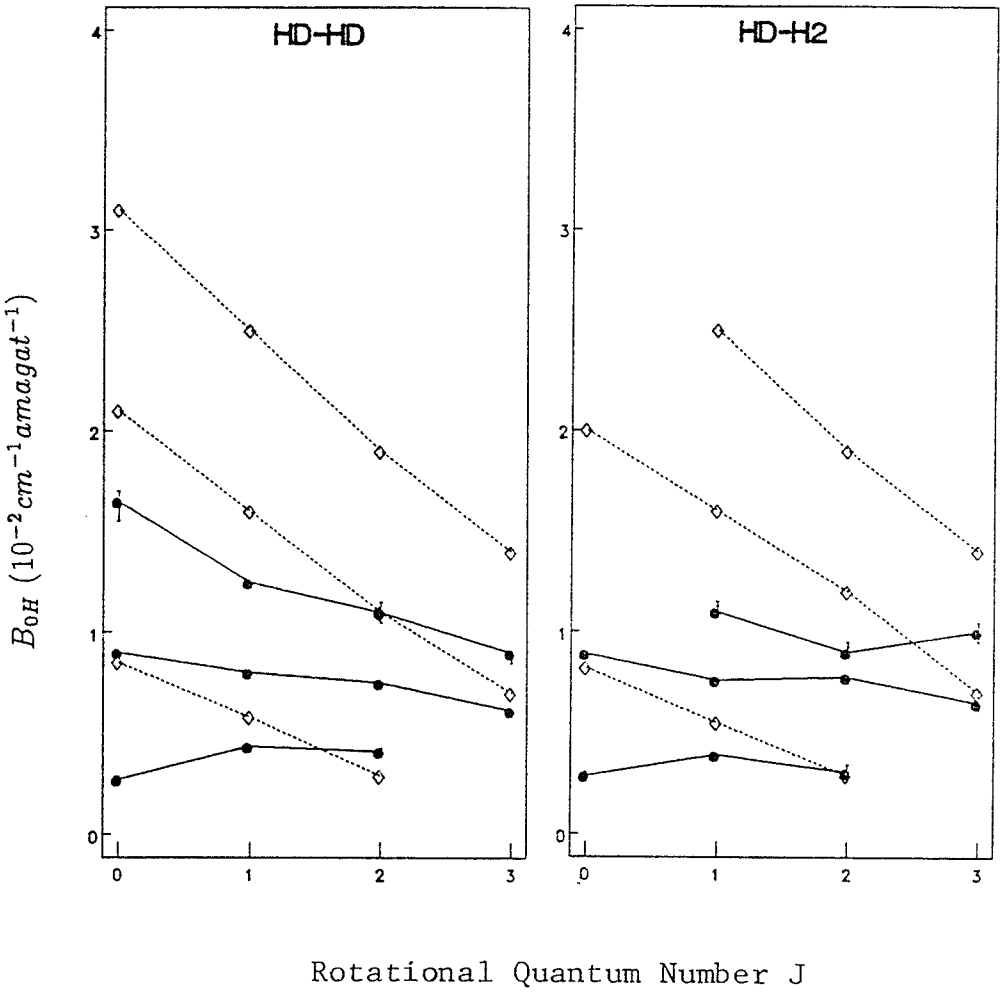

Figure 6.4: The HWHM broadening coefficient B_{0H} vs. quantum number J for $HD-HD$ and $HD-H_2$. Straight line segments are drawn to connect the points.

•: experimental.

◇: semiclassical calculation.

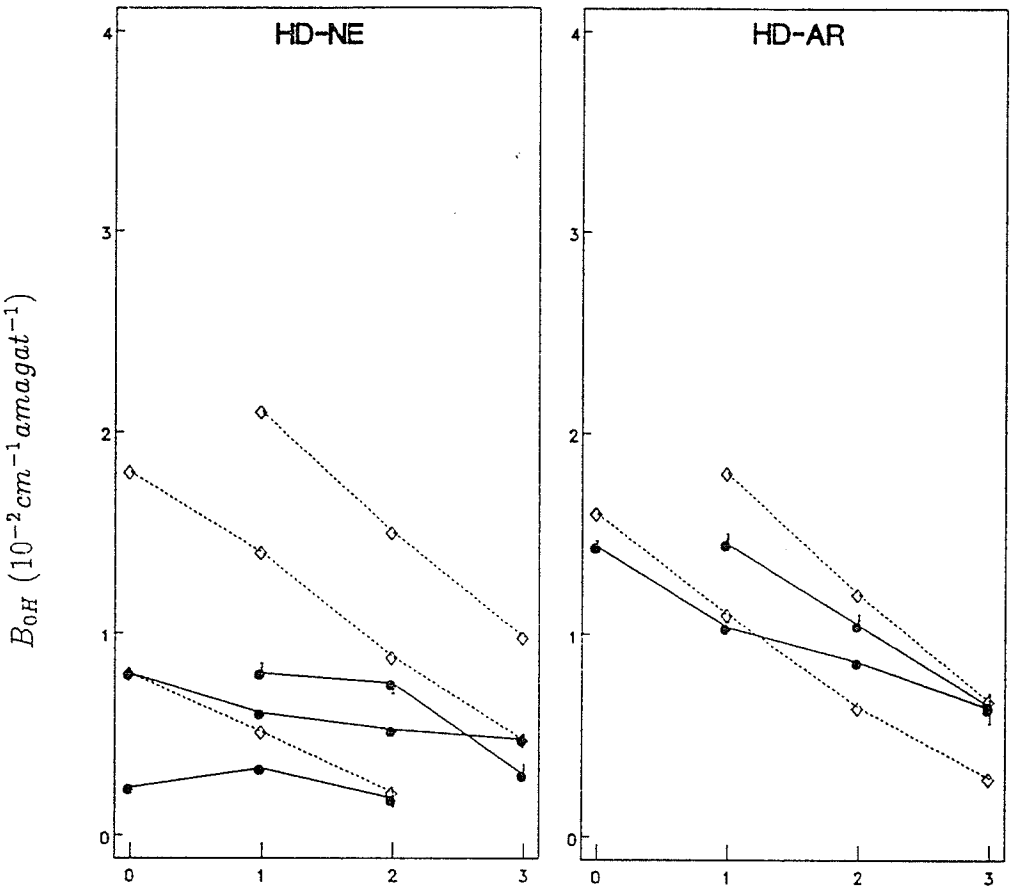

Figure 6.5: The HWHM broadening coefficient B_{0H} vs. quantum number J for $HD - Ne$ and $HD - Ar$. Straight line segments are drawn to connect the points.

•: experimental.

◇: semiclassical calculation.

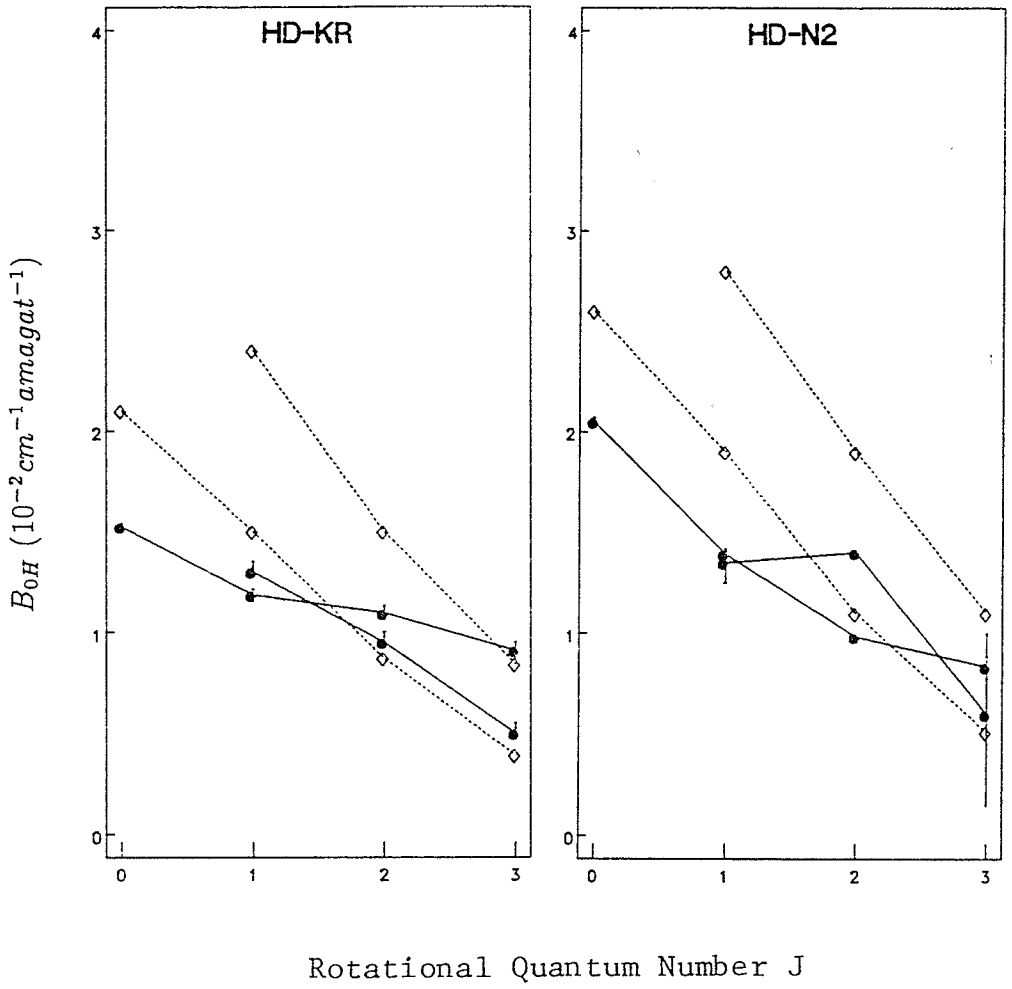

Figure 6.6: The HWHM broadening coefficient B_{0H} vs. quantum number J for $HD - Kr$ and $HD - N_2$. Straight line segments are drawn to connect the points.

●: experimental.

◇: semiclassical calculation.

and $HD - He$ with the Ben-Reuven-Fano-Baranger formalism using the explicit formula of Ben-Renven in which the rotational angular momentum of the bath molecule is first coupled to the orbital angular momentum of the collision and the resultant is then coupled to the rotational angular momentum of the radiating molecule [126]. The potential used in their calculation was a six-term Legendre polynomial expansion grid. Their calculation is in excellent agreement with our experimental results. Whether this type of calculation gives consistent results for R(2) and R(3), as well as for other systems remains unknown. The HWHM deduced from their calculated line shape cross section and the corresponding experimental HWHM broadening coefficient B_{0H} are collected in Table 6.5 and plotted in Figure 6.7.

Table 6.5: comparison of experimental and theoretical HWHM broadening coefficients B_{0H} ($10^{-2} cm^{-1} amagat^{-1}$) for R(0) and R(1) for $HD - H_2$ and $HD - He$. Uncertainty appears in parentheses.

Reference	system	T (K)	B_0 R(0)	B_0 R(1)
		Experiment		
Present work	$HD - H_2$	77	0.28(2)	
		195	0.89(2)	
	$HD - He$	77	0.15(1)	0.20(1)
		195	0.53(6)	0.51(1)
1986 *experiment*[a]		296		1.07(3)
		Calculation		
Schaefer and Monchick[b]	$HD - H_2$	77	0.35	
		195	0.89	
	$HD - He$	77	0.17	0.22
		195	0.64	0.62
		296		1.05

a: Reference [63].

b: Reference [126].

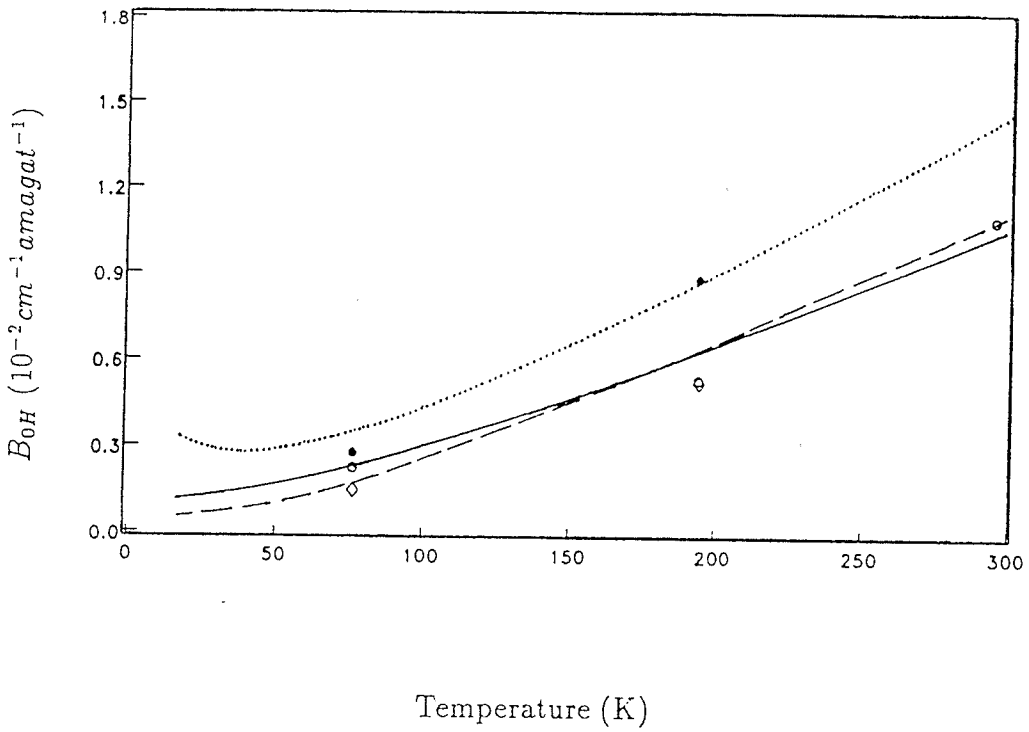

Figure 6.7: The HWHM broadening coefficient B_{0H} $(10^{-2}cm^{-1}amagat^{-1})$ for $HD - H_2$ and $HD - He$ as a function of temperature.

•: R(0), $HD - H_2$, experimantal.

◇: R(0), $HD - He$, experimental.

○: R(1), $HD - He$, experimntal.

Dotted line: R(0), $HD - H_2$, deduced from Reference [126].

Dashed line: R(0), $HD - He$, deduced from Reference [126].

Solid line: R(1), $HD - He$, deduced from Reference [126].

6.3.2 Absolute Frequency and Frequency Shift Coefficient

Now we turn to the absolute frequencies of the four pure rotational lines of HD and the frequency shift coefficients for $HD - HD$ and $HD - X$ systems. As illustrated in Table 4.5, the absolute frequency measured in this laboratory is quite consistent in the 1990, 1987 and 1986 experiments. The average values, with the existing experimental measurements of other workers, are collected in Table 6.6. From the frequency determinations, new rotational constants for HD may be deduced following [101]

$$E(J) = BJ(J+1) - D[J(J+1)]^2 + H[J(J+1)]^3 \ .$$

These are presented in Table 6.7 along with published rotational constants for comparison.

Our absolute frequency determinations are in good agreement with the experimental results of other workers, and in excellent agreement with the frequencies calculated from the published rotational constants. However, the measurements of McKellar *et al.* and of McKellar are consistently lower than ours. Note that their results are also lower than the calculated frequencies if any set of the rotational constants in Table 6.7 is used.

As for the broadening coefficient, the frequency shift coefficient in Table 4.10 shows a general tendency in J-dependence and temperature dependence. Specifically, S_0 goes from positive (blue shift) to negative(red shift) for all systems at all temperatures with increasing J, and S_0 increases with increasing temperature at a given J for most cases. A comparison of various experimental frequency shift

Table 6.6: Comparison of experimental absolute frequencies ω_0^0 (cm^{-1}) of the pure rotational lines of HD. Uncertainty appears in parentheses.

Reference	ω_0^0			
	$R(0)$	$R(1)$	$R(2)$	$R(3)$
Present work	**89.21(1)**	**177.84(1)**	**265.24(1)**	**350.86(1)**
McKellar et al.[a]	89.226(3)			
Essenwenger and Gush[b]				350.852(2)
McKellar[c]		177.828(2)	265.207(2)	350.844(2)

a: Reference [50].

b: Reference [51].

c: Reference [56].

Table 6.7: Rotational constants (cm^{-1}) of HD deduced from experimental absolute frequencies of the pure rotational lines of HD. Uncertainty appears in parentheses.

Reference	B	D	H
Present work	**44.6626(14)**	**0.02554(21)**	**0.0000165(73)**
Essenwenger and Gush[a]	44.6614(21)	0.02558(6)	0.0000174(5)
Rich et al.[b]	44.6656(17)	0.02583(29)	0.000030(19)
McKellar et al.[c]	44.6665(15)	0.02586(12)	0.0000217(25)

a: Reference [51].

b: Reference [102].

c: Reference [103].

coefficients at low temperature can be made only for R(0) and R(1) for $HD-HD$ and $HD-Ne$ at 77 K (Table 6.8). Although these two laboratories agree quite well for the frequency shift for $HD-Ne$ at 77 K, a significant disagreement appears on S_0 for R(0) and R(1) for $HD-HD$ at 77 K. We notice that S_0 is sensitive to the quality of the spectra as well as to the technique of profile fitting. Namely the different experiments with different S/N ratios or the same experiment with different profile fitting procedures will result in different frequency shifts. Tests have been made for $HD-HD$ at 77 K in two other independent experiments in this laboratory. When the Fano line shape profile was applied, the frequency shifts for R(0) and R(1) for the first experiment were 0.318(52) and 0.055(26) respectively, in units $10^{-3}cm^{-1}amagat^{-1}$. For the second experi-

Table 6.8: Comparison of experimental frequency shift coefficients S_0 ($10^{-3}cm^{-1}amagat^{-1}$) for $HD-HD$ and $HD-Ne$ at low temperature. Uncertainty appears in parentheses.

Reference	system	T (K)	S_0	
			$R(0)$	$R(1)$
Present work	$HD-HD$	77	0.305(67)	0.074(18)
	$HD-Ne$	77	1.01(6)	
McKellar et al.[a]	$HD-HD$	77	0.09(3)	0.9(3)
	$HD-Ne$	77	1.08	

a: Reference [50]

ment, the corresponding values were, respectively, 0.595(101) and 0.157(109), in the same units. A different answer was given when the Lorentzian profile was applied, for example, the corresponding values for the first experiment became 0.464(83) and 0.024(66) in the same units. However,the magnitude of S_0 for R(1) never exceeded S_0 for R(0) for $HD-HD$ at 77 K, regardless of the experiment and the fitting procedure. This is an exception in contradistinction to $HD-H_2$, $HD-He$ and $HD-Ne$ at 77 K, where S_0 for R(1) is always greater than that for R(0).

A comparison with theoretical calculation of Schaefer and Monchick is shown in Table 6.9. The values of S_0 for R(0) for $HD-H_2$, and for R(0) and

R(1) for $HD - He$ agree very well for our experimental result and the theoretical calculations. They are plotted in Figure 6.8. This result suggests that our frequency shift cofficients are generally accurate.

6.4 Interference Parameters

6.4.1 Interference Parameter a

The interference parameter a is defined to be positive for the constructive interference between allowed dipole moment and collision- induced dipole moment, and negative for the destructive interference. Experimentally, a is determined by the slope and the intercept of the curve of integrated absorption coefficient versus perturber density, as described in chapter 4. This determination is quite sensitive to the fluctuation of the measured integrated intensity as discussed in the early section of this chapter. The magnitude of a is usually of the order $10^{-3} amagat^{-1}$, a fairly small quantity. As a result, the determination of a from different experiments, or from the same experiment with different ranges of perturber density will possibly give very different answers. Because of the above reasons, the agreement among various experiments in different density ranges, or the agreement between the theory and experiment may not be considered to the same accuracy as with other parameters. In all comparisons, the quality of the spectra, the number of data points and the density range should be kept in mind. The number of data points and the density range for different rotational lines and different samples at different temperatures used for the determination of a in this study are summarized in Table 6.10.

There were two fitting procedures used, as described in chapter 4, to obtain

Table 6.9: Comparison of experimental and theoretical frequency shift coefficients ($10^{-3} cm^{-1} amagat^{-1}$) for R(0) and R(1) for $HD - H_2$ and $HD - He$. Uncertainty appears in parentheses.

Reference	System	T (K)	S_0 R(0)	S_0 R(1)
		Experiment		
Present work	$HD - H_2$	77	0.31(5)	
		195	1.02(26)	
	$HD - He$	77	0.58(4)	0.65(31)
		195	0.98(53)	2.15(12)
1986 *experiment*[a]		296		2.4(2)
		Calculation		
Schaefer and Monchick[b]	$HD - H_2$	77	0.46	
		195	1.03	
	$HD - He$	77	0.73	1.03
		195	1.28	2.06
		296		2.50

a: Reference [63].

b: Reference [126].

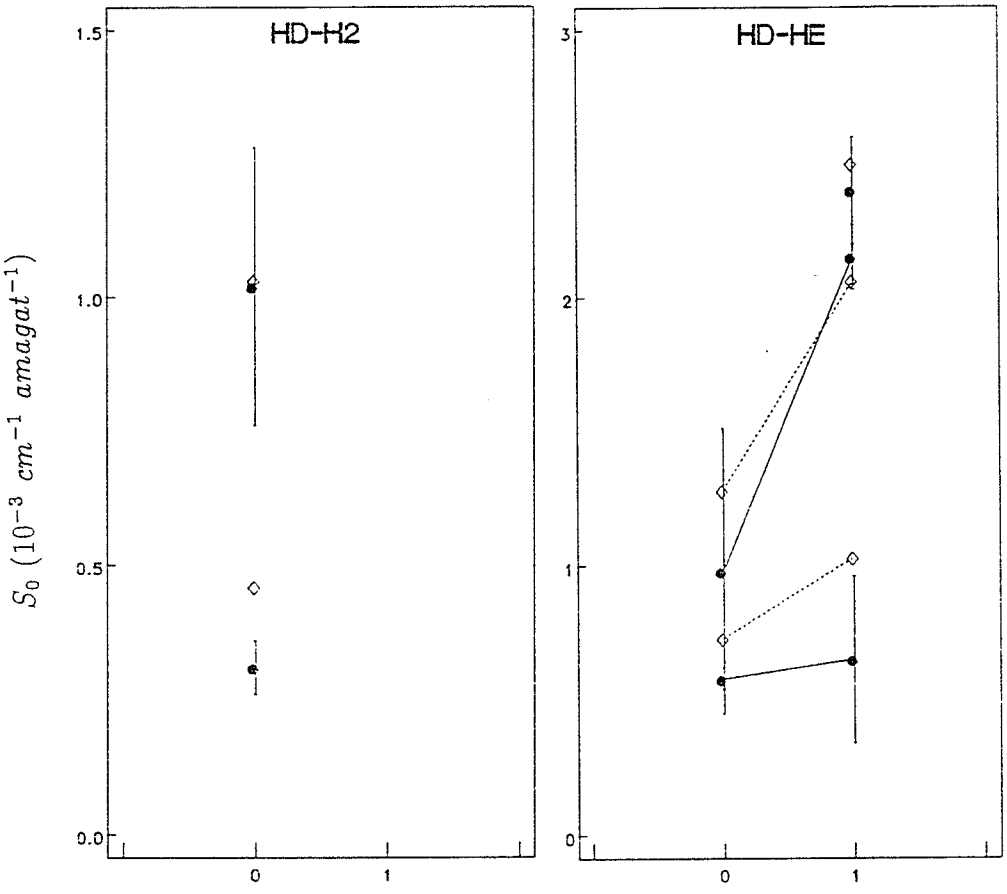

Figure 6.8: Comparision of experimental and theoretical frequency shifts S_0 for R(0) and R(1) for $HD - H_2$ and $HD - He$

•: experimental.

◇: calculation of Reference [126].

Table 6.10: The number of data points N and the hightest perturber density ρ_{max} (amagat) used in the determination of a.

Sample	T (K)	N				ρ_{max}			
		R(0)	R(1)	R(2)	R(3)	R(0)	R(1)	R(2)	R(3)
$HD-HD$	77[a]	41	41	41	41	81	81	81	81
	195[b]	15	15	15	15	60	60	60	60
	296[c]	32	32	32	32	68	68	68	68
$HD-H_2$	77[a]	16	16	14	–	40	40	35	–
	195[b]	5	15	15	6	17	60	60	22
	296[b]	–	16	17	14	–	37	39	32
$HD-He$	77[a]	20	20	20	–	64	64	64	–
	195[a]	12	12	12	12	44	44	44	44
	296[c]	–	10	10	10	–	57	57	57
$HD-Ne$	77[a]	18	18	12	–	69	69	35	–
	195[b]	13	14	14	12	51	56	56	47
	296[c]	–	12	12	12	–	62	62	62
$HD-Ar$	195[a]	10	10	15	9	43	43	72	38
	296[c]	–	8	9	17	–	40	48	53
$HD-Kr$	195[b]	11	16	17	8	23	36	40	18
	296[b]	–	15	15	15	–	40	40	40
$HD-N_2$	195[b]	11	17	17	12	15	40	40	18
	296[b]	–	15	15	15	–	37	37	37

a: 1987 experiment.

b: 1990 experiment.

c: 1986 experiment, c.f. Reference [63]

the interference parameter a. The free fitting, although correct in principle, is in practice too sensitive to the data points of curvature. Thus the spread or fluctuation in the absorption coefficient can lead the free fitting to an essentially unreliable result. Unless the measurements of integrated absorption coefficients span a wide density range, the free fitting procedure cannot accurately determine the coefficient of the ρ^2 term. Figure 6.9 shows the typical examples. The theory fitting on the other hand, mostly gives reasonable results. Thus we will essentially use the theory fitting result for discussion.

The experimental interference parameters a at low temperature from other workers are compared with our experimental determinations in Table 6.11.

Table 6.11: The comparison of experimental interference parameter a (10^{-3} $amagat^{-1}$) at low temperature. Uncertainty appears in parentheses.

Reference	system	T (K)	a $R(0)$	a $R(1)$
Present work	$HD-HD$	77	+3.1(4)	+2.2(2)
	$HD-Ne$	77	+5.8(15)	
McKellar et al.[a]	$HD-HD$	77	+0.6(4)[b]	+0.6(10)[b]
	$HD-Ne$	77	+3.4(2)[c]	

a: Reference [50].

b: ρ_{max} is 84.4 amagat.

c: ρ_{max} is 123 amagat.

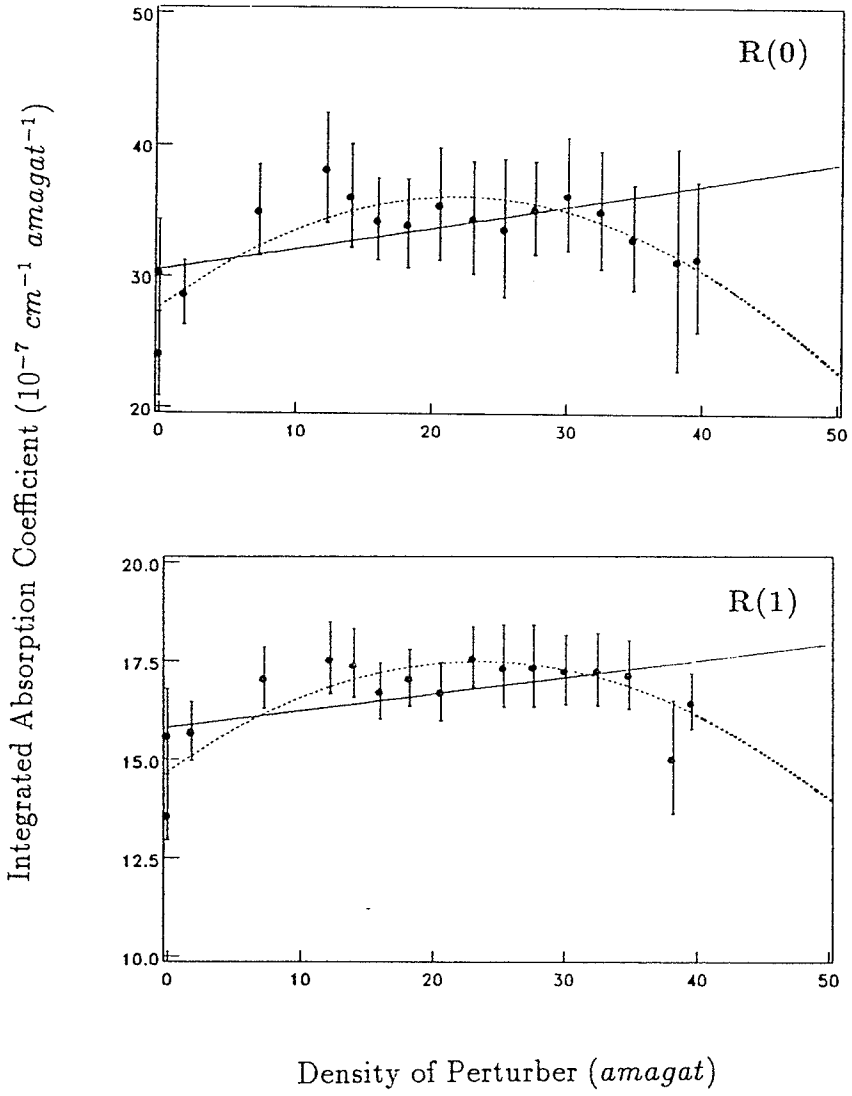

Figure 6.9: Integrated absorption coefficient for R(0) and R(1) for $HD - H_2$ at 77 K as a function of density. The dotted line is the free fitted curve and the solid line is the theory fitted curve.

Table 6.12: comparison of experimental integrated absorption coefficient (10^{-6} cm^{-1} $amagat^{-1}$) at 77 K for $HD - HD$. The data are deduced from Table 6.11. ρ is in amagat. Uncertainty appears in parentheses.

Reference	Integrated Absorption Coefficient			
	R(0)		R(1)	
	$\rho = 0$	$\rho = 80$	$\rho = 0$	$\rho = 80$
Present work	2.97(2)	3.71(12)	1.48(2)	1.74(4)
McKellar et al.[a]	3.84(26)	4.03(15)	1.56(16)	1.64(30)

a: Reference [50].

For $HD - HD$ at 77 K, the results of McKellar *et al.* are much lower than ours. Remember that their corresponding zero density intercepts are higher than ours (c.f. Equation 4.15 and Tables 4.3 and 6.2). If we convert the corresponding data to the integrated absorption coefficient by using Equation 4.15, Tables 4.3 and 6.2, we obtain the integrated absorption coefficient at zero and at about 80 amagat density; these are listed in Table 6.12.

The small statistical error quoted in our results arises because of the large number of data points (41). The actual uncertainty may be larger, as was discussed in section 6.1. Keeping this in mind when comparing the converted integrated absorption coefficient in Table 6.12, we see that the determination of the integrated absorption coefficient in these two laboratories agrees reasonably well.

The difference in their slopes is probably due to the fluctuation of the integrated absorption coefficient at low densities, as discussed in the previous section. For $HD - HD$, the interference parameters a are positive, indicating a constructive interference between allowed and induced dipole moment. It is interesting to note that the constructive interference is also observed in the condensed phases of HD for R(0) [60][61][127]. For $HD - Ne$, there is 40 amagat density range difference between the two laboratories while the agreement on experimental a is reasonably good. As can be seen in Tables 4.6 and 4.7, the general trends in the interference parameter a from our experimental results may be summarized as follows:

1. The interference parameter a changes sign for all J from 77 K to 296 K for $HD - HD$.

2. For $HD - atom$ and for a given temperature, a is positive for all J and all systems at 77 K; at 195 K, in general, a is positive for R(0), R(2) and R(3), but negative for R(1) for all systems; at 296 K, usually, a is positive for R(2) and R(3) while negative for R(1).

3. For a given J, a is always positive for R(0) for all temperatures and all systems in general; for R(1), a changes sign frequently for all systems; for R(2) and R(3) there is less frequent sign change in a.

4. For a given system, the sign change of a occurs at low J for small perturber such as He, Ne and so on, but at high J for large perturbers such as Kr and N_2.

5. Generally the small perturbers give mostly constructive interference while large perturbers give mostly destructive interference for all J and at all temperatures.

The above general trends may not be explained consistently by a simple picture. The mechanism involved in the interference for individual rotational lines, especially for R(0) and R(1), seems much more complicated.

Comparing the experimental interference parameter a (Tables 4.6 and 4.7) with a_{theory} calculated (Table 5.4) according to the theory developed by Herman, Tipping and Poll, we find that about 57% agree well on the magnitude only; 63% agree on the sign ($HD-Kr$ not included) only; 34% agree reasonably well on both sign and the magnitude ($HD-Kr$ not included), as can be seen in Table 6.13 where the ratio of a/a_{theory}, i. e. Δ', are listed. The better agreement between experiment and theory is found for R(2) and R(3) for $HD-atom$ systems.

If this result is taken as a demonstration of the validity of the theory, we can then use it to estimate the induced dipole moment for $HD-Ne$ and $HD-N_2$ from the experimental interference parameter a. It is assumed that the induced dipole moment for $HD-Ne$ and $HD-N_2$ are dominated by the isotropic overlap component, which is normally true [69], and has the form [73]

$$\mu^I(R) = Ae^{B(R-R_0)}, \tag{6.5}$$

where R is the intermolecular distance and A, B and R_0 are parameters to be determined. Making use of Equation 5.14, we have the following integral equation,

$$\begin{aligned} 1.23657a &= A\int_0^\infty \exp\left[B(R-R_0) - V_{H_2-X}(R)\beta\right] \\ &\quad \times\{\frac{\sinh\left[V'_{H_2-X}(R)\beta r_e/6\right]}{V'_{H_2-X}\beta r_e/6}\}R^2dR. \end{aligned} \tag{6.6}$$

Here a is the interference parameter and the other symbols are the same as in chapter 5. From the experimental results, there are three integral equations for $HD-Ne$ corresponding to three temperatures, and two for $HD-N_2$. The potentials used in the calculation were the same Lennard-Jones (6-12) potentials used in the calculation of line width in chapter 5. The IMSL (International Mathematical and Statistical Library) routines DCADRE (for numerical integration of a function using cautious adaptive Romberg extrapolation) and DMLIN (for numerical integration of a function of several variables with a hyper-rectangle method) were employed in a FORTRAN program for the fitting procedure. For the integral equations, the solution is not unique. It is known that the value of $(BR_0)^{-1}$ for H_2-He is about 0.11 [128][129]. We adapt the same assumption, i. e. $(BR_0)^{-1} \sim 0.11$ for $HD-Ne$ and $HD-N_2$, as used by Poll and Hunt [73]. The estimated values of A, B and R_0 for $HD-Ne$ and $HD-N_2$ together with the estimated values for H_2-Ar and H_2-Kr by Poll and Hunt [73] are presented in Table 6.14 and are plotted in Figure 6.8. The accuracy of the estimated value depends on the accuracy of the interference parameter a and the potential model, and thus is hard to determine. From the point of view that the induced dipole moment is roughly proportional to the polarizability of perturber molecule [63], the above estimated values are of the right order. The possibility of the deduction of such information provides another justification of further experimental and theoretical study of the interference parameter a.

Table 6.13: The ratio of a/a_{theory} The uncertainty appears in parentheses.

		a/a_{theory}			
System	T (K)	R(0)	R(1)	R(2)	R(3)
$HD-HD$	77	+2.3(3)	+2.1(2)	+1.5(3)	
	195	−1.3(1)	−0.3(1)	−0.1(1)	−9.8(5)
	296	−1.2(9)	−0.7(1)	−0.8(1)	+1.6(5)
$HD-H_2$	77	+5.1(14)	+3.0(19)	+1.1(40)	
	195	+1.1(7)	−2.3(4)	+0.1(3)	−5.3(35)
	296		−4.6(7)	+5.0(5)	−2.9(12)
$HD-He$	77	+1.3(4)	+1.4(2)	+1.0(3)	
	195	−1.8(6)	−0.1(1)	+0.4(1)	+0.6(5)
	296		+0.8(1)	+0.5(1)	+1.3(3)
$HD-Ar$	195	+0.1(1)	−0.4(1)	+1.1(7)	+0.3(4)
	296		+0.2(1)	+0.6(1)	+1.0(1)
$HD-Kr$[a]	195	0.3(1)	1.6(2)	1.0(2)	1.2(8)
	296		1.6(1)	0.7(1)	0.6(1)

a: the sign of induced moment is unknown.

Table 6.14: Estimated parameters A($10^{-4}D$), B($\mathring{A}^{-1}$) and R_0 ($\mathring{A}$) of induced dipole moment.

Syatem	A	B	R_0
$HD-Ne$	−6.5	−3.03	2.99
$HD-N_2$	−12.8	−2.89	3.15
H_2-Ar[a]	10.0	−2.86	3.17
H_2-Kr[a]	16.0	−2.79	3.26

a: Reference [73], the sign of A is unknown.

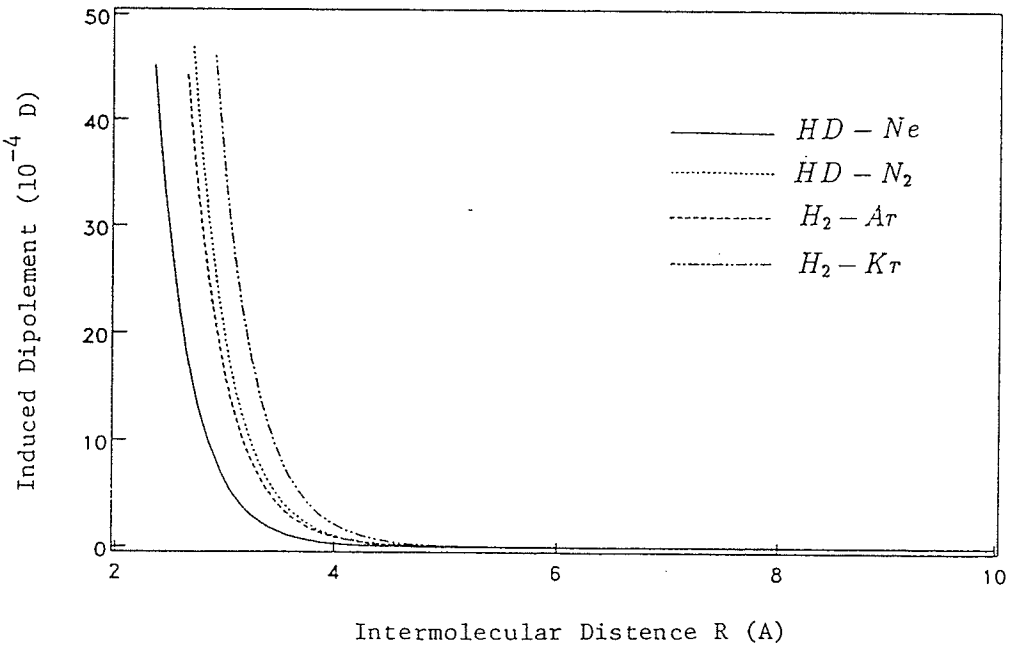

Figure 6.10: The estimated magnitude of the induced dipole moment for $HD-Ne$, $HD-N_2$, H_2-Ar and H_2-Kr as a function of intermolecular distance R.

6.4.2 Interference Parameter $N_0\Delta''I$

The experimental $N_0\Delta''I$ and the published experimental determination at low temperature of other workers are collected in Table 6.15. Unlike the vibration-rotational band of $HD-HD$ [24][25][26][27], the asymmetry of the pure rotational line profile is found to be very small. The difficulties in the base-line correction due to the broad collision-induced background make the determination of such a small asymmetry even more difficult. Consequently the results for $N_0\Delta''I$ may be even less reliable than that of a. However the agreement on both the sign and the magnitude between the two laboratories, as shown in Table 6.15 is fairly good except for R(1) for $HD-HD$ at 77 K. Comparing the experimental interference parameters carefully, one finds that in quite a few cases, even with the uncertainties, the magnitude of $N_0\Delta''I$ is larger than that of $a/2$. For example, $HD-H_2$ [R(2)] at 195 K, $HD-He$ [R(2)] at 77 K, $HD-Ne$ [R(0) and R(1)] at 195 K and $HD-Ar$ [R(0) and R(3)] at 195 K, etc. This result also occured in the 1986 experimental results [63] in $HD-HD$ [R(1) and R(2)] and $HD-Ne$ [R(1)] at 296 K. It also appeared in McKellar's experimental results [56] in $HD-HD$ [R(1), R(2) and R(3); 0.0213 vs. 0.00073, 0.0345 vs. 0.00099 and 0.00214 vs. 0.00122 for $N_0\Delta''I$ and a respectively] at 296 K. From the theory of Herman Tipping and Poll, as expressed in Equations 2.107, 2.89 and 2.105, the ρ^2 term arises purely from the intercollisional interference or the *scalar* interference which should be always positive [45][62]. Thus the magnitude of $N_0\Delta'I = a/2$ should be always larger than that of $N_0\Delta''I$, if the theory adequately represents the experimental results. The existence of the contradiction is possibly due to the difficulties in the determination of small asymmetry factor, but also may possibly be due to

difficulties with the theory itself.

Table 6.15: The comparison of experimental interference parameter $N_0\Delta''I$ (10^{-4} $amagat^{-1}$) at low temperature. Uncertainty appears in parentheses.

Reference	system	T (K)	$R(0)$	$R(1)$
Present work	$HD-HD$	77	−2.0(8)	−0.7(7)
	$HD-Ne$	77	+15.3(3)	
McKellar et al.[a]	$HD-HD$	77	−1.8(2)	−5.6(8)
	$HD-Ne$	77	+16.5(3)	

a: Reference [50].

6.5 Further Discussion on the Theory

As has been discussed so far, the data analysis guided by the theory developed by Herman, Tipping and Poll gives the correct allowed dipole moment matrix elements for the pure rotational band of HD. The theoretical calculation of the interference effects for the pure rotational band of $HD-HD$ and $HD-X$ are generally consistent with the experimental determinations with respect to order of magnitude, but quantitatively, relatively good agreement is achieved only for R(2) and R(3) for $HD-atom$ systems. There is an obvious J dependence in

the interference effects from the experimental results which is not predicted by the theory. Furthermore a change in sign of the interference parameter a with temperature at constant J for $HD-HD$ and $HD-X$ is evident in the experiment but not predicted by the theory. From the theory, the temperature enters the calculation of a through the pair distribution function by which, as shown in Figure 6.11, the average dipole moment has a small temperature dependence. The refinements due to rotational-level mixing and near-resonance rotational-level mixing improve the agreement between theory and experiment to some degree but still give results not consistent with experiment both with respect to sign and magnitude. The discrepancies may be due to the phase factor Δ', but ratio of a/a_{theory} shows 1/3 of the corresponding Δ' including their uncertainties are larger than unity. The method of introduction of Δ into the theory requires, however, that the absolute magnitude of either Δ' or Δ'' never exceed unity [46]. These facts may indicate that the mechanism in the interference effects in the pure rotational band for gaseous $HD-HD$ and for the low J lines of $HD-X$, are more complicated than the description in the pioneering theory of Herman, Tipping and Poll.

As was mentioned in chapter 1, there is a new theory recently develo-ped by Gao, Tabisz, Trippenbach and Cooper. In this new theory, the system considered is a single neutral radiator contained within a gas of N neutral foreign perturbers and immersed in a radiation field. The radiator has a series of low-lying, closely spaced energy levels while the perturbers have widely spaced levels. Electric-dipole allowed transitions are assumed possible between levels in both the radiator and perturbers. Thus it applies to $HD-inert\ gas$ systems. The absorption and

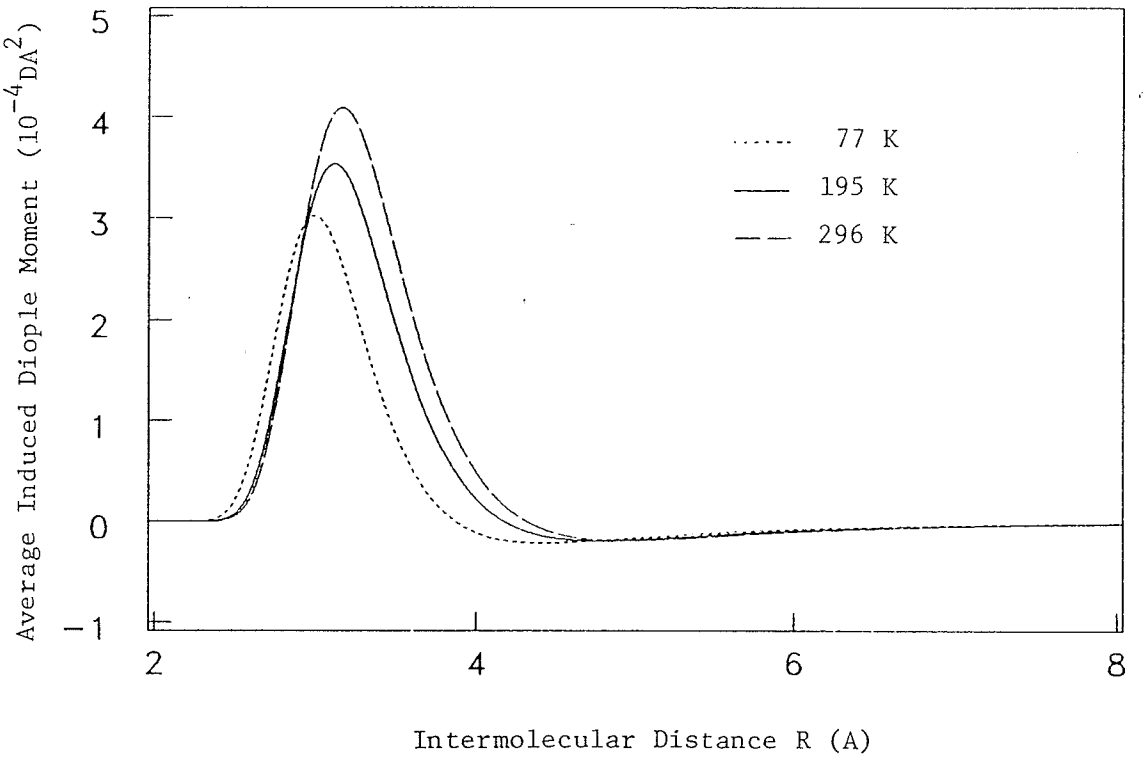

Figure 6.11: The averaged induced dipole moment of $HD - HD$ at 77 K, 195 K and 296 K as a function of intermolecular distance R.

stimulated emission events and the induced cluster dipole moments transition are considered. Both elastic and inelastic collisions and the transitions among the radiator states occuring through such collisions are permitted. This may be the most important difference from the theory of Herman, Tipping and Poll in which only non-J- and non-m-changing collisions are considered. The absorption coefficient from the new theory contains four terms which contribute significantly to the sharp spectral feature,

$$
\begin{aligned}
&\alpha(\omega) \\
&= \frac{4\pi\omega}{3\hbar c} n_R (1 - e^{-\hbar\omega/kT}) Re\{(\Delta + i\gamma)^{-1} i |\langle J_e||\hat{\mu}_R||J_g\rangle|^2 \frac{1}{2J_g+1} \sum_{J_g J_g}^{B} \\
&\quad + (\Delta + i\gamma)^{-1} i n_p \langle J_e||\hat{\mu}_R||J_g\rangle^{*} [\sum_{\Omega} G \\
&\quad \times \ll J_e m_e, J_g m_g | U^I(\infty, 0) [\hat{\mu}^I(0)]_{q_c} U^I(0, -\infty) | J_i m_i, J_i m_i \gg_{av}] \times \frac{1}{2J_i+1} \sum_{J_i J_i}^{B} \\
&\quad + (\Delta + i\gamma)^{-1} i n_p \langle J_e||\hat{\mu}_R||J_g\rangle [\sum_{\Omega} G \\
&\quad \times \ll J_\alpha m_\alpha, J_\alpha m_\alpha | [\hat{\mu}^I(0)]^{*}_{q_c} U^I(0, -\infty) | J_e m_e, J_g m_g \gg_{av}] \times \frac{1}{2J_g+1} \sum_{J_g J_g}^{B} \\
&\quad + (\Delta + i\gamma)^{-1} i n_p^2 [\sum_{\Omega} G \\
&\quad \times \ll J_\alpha m_\alpha, J_\alpha m_\alpha | [\hat{\mu}^I(0)]^{*}_{q_c} U^I(0, -\infty) | J_e m_e, J_g m_g \gg_{av}] \\
&\quad \times [\sum_{\Omega} G \ll J_e m_e, J_g m_g | U^I(\infty, 0) [\hat{\mu}^I(0)]_{q_c} U^I(0, -\infty) | J_i m_i, J_i m_i \gg_{av}] \\
&\quad \times \frac{1}{2J_i+1} \sum_{J_i J_i}^{B} \}, \qquad (6.7)
\end{aligned}
$$

with

$$\Omega = J_i, q_c, m_e, m_g, m_i$$

and

$$G = (-)^{J_e - m_e} \begin{pmatrix} J_e & 1 & J_g \\ -m_e & q_c & m_g \end{pmatrix}. \tag{6.8}$$

Here Δ is the detuning (ω-ω_{eg}); n_R and n_p is the number density of the radiator and perturber respectively, $\hat{\mu}_R$ is the dipole moment operator of the radiator and $\hat{\mu}^I$ is the induced dipole moment operator; $U^I(t,t')$ is the one perturber collisional propagator, the superscript I denotes the interaction picture, and the subscript q_c and av, respectively, denote the spherical component and the average over velocity, impact parameter and the time of closest approach. The subscripts g and e on the quantum numbers J and m denote the *intial* state and *final* state, while i and α refer to an *intermediate* state. The rest of the notations have their usual meaning in the literature.

Similar to the original theory discussed in chapter 2, the absorption coefficient contains an allowed-allowed term (the first term), allowed-induced terms (the second and third terms) and effect of successive collisions, i.e. the intercollisional interference term (the fourth term). The matrix elements in the last three terms can be further written as

$$\begin{aligned} &\ll J_e m_e, J_g m_g | U^I(\infty, 0) [\hat{\mu}^I(0)]_{q_c} U^I(0, -\infty) | J_i m_i, J_i m_i \gg \\ &= \sum_{JM} e^{-i(\omega_{eg} - \omega_{32}) t_0} \ll J_e m_e, J_g m_g | U^I(\infty, t_0) | J_3 m_3, J_1 m_1 \gg \\ &\quad \times \langle J_3 m_3 | [\hat{\mu}^I(t_0)]_{q_c} | J_2 m_2 \rangle \ll J_2 m_2, J_1 m_1 | U^I(t_0, -\infty) | J_i m_i, J_i m_i \gg, \end{aligned}$$

(6.9)

with

$$J = J_1, J_2, J_3 \quad and \quad M = m_1, m_2, m_3,$$

and

$$\begin{aligned} &\ll J_\alpha m_\alpha, J_\alpha m_\alpha | [\hat{\mu}^I(0)]^\times_{q_c} U^I(0, -\infty) | J_e m_e, J_g m_g \gg \\ &= \sum_{J_1 m_1} e^{-i(\omega_{eg} - \omega_{1\alpha})t_0} \langle J_1 m_1 | [\hat{\mu}^I(t_0)]_{q_c} | J_\alpha m_\alpha \rangle^\times \\ &\quad \times \ll J_1 m_1, J_\alpha m_\alpha | U^I(t_0, -\infty) | J_e m_e, J_g m_g \gg, \end{aligned} \tag{6.10}$$

where t_0 represents the time between the radiative event and the time of closest approach. This time is of the order of duration of a collision, i.e. $t_0 \sim \tau_d$.

Now, taking $U^I(t, t')$ to be diagonal in J, letting

$$\mu_R = \langle J_e || \hat{\mu}_R || J_g \rangle \tag{6.11}$$

and

$$\mu_I = \sum_{q_c m_e m_g} G \int_{-\infty}^{\infty} dt_0 e^{-i\omega_{eg} t_0} \langle J_e m_e | \hat{U}^I(\infty, t_0) [\mu^I(t_0)]_{q_c} \hat{U}^{I\dagger}(\infty, t_0) | J_g m_g \rangle_{av}, \tag{6.12}$$

where $\hat{U}^I$ is the *Hilbert* space evolution operator, and writing

$$\mu_I = |\mu_I| e^{i\delta} = |\mu_I| (\Delta' + i\Delta''), \tag{6.13}$$

and

$$\gamma = \gamma' + i\gamma'', \tag{6.14}$$

one obtains a simplified form of absorption coefficient as follows:

$$\begin{aligned}\frac{\alpha(\omega)}{\omega} &= n_R(\frac{4\pi}{3\hbar c})(1-e^{-\hbar\omega/kT})\{\frac{\gamma'}{(\gamma')^2+(\Delta-\gamma'')^2} \\ &\times[\mu_R^2+2n_p\Delta'\mu_R|\mu_I|+n_p^2(\Delta'^2-\Delta''^2)\mu_I^2] \\ &-\frac{2(\Delta-\gamma'')}{(\gamma')^2+(\Delta-\gamma'')^2}[\Delta''n_p\mu_R|\mu_I|+\Delta'\Delta''n_p^2|\mu_I|^2]\}\frac{1}{2J_g+1}\sum_{J_gJ_g}^{B}.\end{aligned} \tag{6.15}$$

This is the same form of Equation 2.106 except that the Δ' and Δ'' are not the same as in Equation 2.106, since here the m-changing collisions are permitted.

In this manner, the theory developed by Herman, Tipping and Poll as discussed in chapter 2 is seen to be a special case in which the propagator is diagonal in both m and J [46][64], that is, in which only pure elastic collisions are permitted.

In general case, the propagator is not diagonal in m and J. It can be proved that the leading term in the expansion of the propagator with respect to time t beyond the diagonal term is of the same form as the first-order time-independent perturbation theory result used by Tabisz and Nelson to describe rotational-level mixing [52][64]. However the new theory goes further because the full propagator is used and the inelastic transitions can occur at times during the collision; thereby the mechanism is different from the previous work. It actually provides that, in the general case where both elastic and inelastic collisions are permitted, there will be an additional contribution to the second term of Equation 6.15, so that the

phase factor will become an *effective phase factor* which will not be constrained to remain between $+1$ and -1. As was discussed in the last section, this is what the experimental results have made evident.

The new theory, at least in its frame work, gives a better description for the pure rotational band for gaseous HD, although its full justification requires, however, detailed calculation and comparison with the experimental results. Such detailed calculations are not available at the time of the writing of this thesis.

Chapter 7

CONCLUSIONS

Characterization of the density and temperature dependence of spectral line shape parameters and absorption coefficient is reasonably complete based on the experiments at 77 K, 195 K and 296 K. After the detailed discussion in chapter 6, we reach the following conclusions:

1. The allowed dipole moment of HD for the first four transitions of the pure rotational band as determined from $HD - HD$ and $HD - X$ systems at different temperatures and is found to be 8.10(15) for R(0), 8.04(12) for R(1), 8.05(12) for R(2) and 8.41(40) for R(3), in units 10^{-4} debye (the quoted errors are three standard deviations). The J dependence in the allowed dipole moment of HD is not the same as predicted by the theory. Within the 99% confident error bar, the J dependence predicted by Wolniewicz is possible. The averaged *ab initio* calculations agree well with, but are about 3% larger than, the current experimental determinations.

2. The absolute frequency for the four pure rotational lines as determined from the averaged measurements at different temperatures are found to be 89.2(1) for R(0), 177.84(1) for R(1), 265.24(1) for R(2) and 350.86(1) for R(3), in the units

cm^{-1}. They are in very good agreement with the published rotational constants of HD.

3. The line broadening coefficient for the pure rotational band for $HD-HD$ and $HD-X$ were determined at different temperatures. Calculations based on a simplified model within semiclassical theory agree in the general trends and order of the magnitude with the experimental determinations, and temperature dependence. Better agreement is found for R(2)and R(3), and for HD perturbed with large atoms. Quantum mechanical calculations for R(0) and R(1) for $HD-H_2$ and $HD-He$ [126] are found to be in very good agreement with the experimental result, for both the line broadening coefficient and frequency shift. It suggests, as expected, that for the small molecule collision pair such as $HD-HD$, $HD-H_2$, $HD-He$ and perhaps $HD-Ne$, the quantum mechanical calculation is more suitable.

4. The integrated absorption coefficient, or the interference effect, for the pure rotational band of gaseous HD in $HD-HD$ and $HD-X$ systems generally agree in order of magnitude with the prediction of the theory developed by Herman, Tipping and Poll. Better agreement is found for R(2) and R(3) for $HD-atom$. Based on this fact, the induced dipole moment for $HD-Ne$ and $HD-N_2$ was estimated from the experimental interference parameter a for R(2) according to the theory, and to be found $\mu^I_{HD-Ne}(R) = -6.5\times10^{-4}e^{-3.03(R-2.99)}$ debye and $\mu^I_{HD-N_2}(R) = -11.3\times10^{-4}e^{-2.89(R-3.15)}$ debye respectively, where R is in units $\AA$. However the experimental results show that the interference effect has a more complicated behaviour than predicted by the above theory. The J dependence and the temperature dependence of the interference parameter a,

particularly its change in sign for $HD - HD$ and $HD - X$, can not be explained by the above theory.

5. A new theory developed by Gao, Tabisz, Trippenbach and Cooper [64] contains the earlier efforts as special cases and gives more general description in its theoretical frame work. Its full justification awaits for the detailed calculations and comparison with the experimental results.

Appendix A

Control Program for Data Collection

This MACRO program is used to control the data collection of NICOLET system in the experiment. The raw data are recorded in the hard disk for data analysis. The meaning of the statements in the program can be found in Reference [93].

```
TEM=4
NPR
PMD
OMD
Automatic data collection 400 scans.
PMD
OMD
Type PFN for data collection:
PFN
RPF
```

NSS=200

NSD=200

SFN=2

OFN=2

OMD

Type scratch file number [>= 5]:

DFN

SPF

OMD

Type the name for permanent file [6 CHARACTERS.3 NUMBER]:

IFN

CLD

PMD

OMD

Scans collected:

PRN NSD

PMD

CLS

CAD

OMD

Scans collected:

PAD

PRN NSS

AFP

OMD

The experiment for

PRN DFN

OMD

is complete!

TEM=4

NPR

PMD

OMD

Press EXPT.0 to begin next data collection.

PMD

PMD

END

Appendix B

Macro Program for the Fourier Transform Process

This program is used for automatic Fourier transforming of a set of raw data files. **LP1, LP2** and **LP3** are subroutines. The statements in the program can be found in Reference [93].

TEM=4

NPR

OMD

Auto FT process: from interferogram to absorbance.

PMD

PMD

OMD

Type PFN for FT process:

PFN

RPF

BFN=3

OMD

Type background file name:

GDB

OMD

Type title for background file:

TIB

PRN BFN

STB

PMD

PMD

OMD

Now assign sample files to distination files.

PMD

PMD

OMD

How many sample files?

QIT

LP1

LP2

LP3

PMD

PMD

OMD

Automatic FT process is complete!

```
PMD
PMD
END

LP1

DFN=5
FOR III=1 TIL QIT
PMD
PMD
PRN DFN
OMD
Type sample file name:
GDD
OMD
Type title for the sample file:
TID
STD
DFN=DFN+1
NXT III
PMD
PMD
OMD
This set of sample files is complete!
PMD
```

PMD

END

LP2

OMD

Now FT starts.

PMD

PMD

PRN BFN

STB

FPB

OMD

Complete!

PMD

DFN=4

FOR III=1 TIL QIT

DFN=DFN+1

PRN DFN

STD

FPD

RAD

ABD

OMD

Complete!

PMD

NXT III

PMD

OMD

FT is complete in all sample files!

PMD

PMD

END

LP3

OMD

Now save the absorbance files.

PMD

PMD

PRN

BFN

STB

OMD

Input file name for background:

PDB

PMD

DFN=4

OMD

Input SIX-character file name:

IFN

```
EXT=001
FOR III=1 TIL QIT
DFN=DFN+1
PRN DFN
STD
AFP
EXT=EXT+1
PMD
NXT III
END
```

Appendix C

BASIC Program

This BASIC program is used to convert absorbance data to ASCII for transfer to another computer for further data analysis. This is the modified version of the code in Reference [63] to fit the new data system Nic-660.

```
100 REM This program is to convert data to ASCII and to
110 REM store them in the disk. MODE filename 7 before transfer.
120 DIM A(2), B(2),F(352)
130 DIM X(2000),Y(2000)
140 LET N=1
150 LET M=10
160 PRINT "Enter filename in process."
170 INPUT A$(0),A$(1)
180 CALL BDEFINE(10,A$)
190 CALL FREAD(10,F,352)
200 PRINT "Enter NEW filename to store data."
210 INPUT B$(0),B$(1)
220 LET M=M+1
```

```
230 CALL FALLOC(M,B$,352)
240 LET D$="EXP"
250 LET E$="NTP"
260 LET G$="SSP"
270 CALL FILSTA(F,D$,D1)
280 CALL FILSTA(F,E$,E1)
290 CALL FILSTA(F,G$,G1)
300 CALL FAINT(352,1)
310 CALL IAFLT(F,352)
320 LET W=F(234)-F(233)+1
330 LET L=W
340 CALL FREAD(10,Y,W)
350 CALL FAINT(W,1)
360 CALL IAFLT(Y,W)
370 LET E1=E1/2
380 LET T=2^(D1-19)
390 LET S=15798/G1/E1
400 LET W=L
410 FOR I=0 TO W-1
420 LET X(I)=S*(I+F(233))
430 LET Y(I)=T*Y(I)
440 PRINT#M: X(I);Y(I)
450 PRINT " ** ",A$(0);A$(1);
" >> ";B$(0);B$(1);"is done."
```

```
460 PRINT "Program is ended. Type RUN to continue."
470 END
```

Appendix D

SAS Program

This SAS program is used for fitting R(1) data file for $HD - Ne$ at 195 K. It first corrects the base line, then uses a Fano profile to fit the spectrum, as described in chapter 2. The diagrams are automatically plotted after base line correction and profile fitting, as shown in chapter 2.

```
//STEP1 EXEC SASV5
//SYSIN DD *
GOPTIONS DEVICE=XEROX HSIZE=3.5
 VSIZE=4.8 COLORS=(R,BL,G,B);
TITLE 'FITTING A FANO LINESHAPE
 TO HD-Ne AT FILE NEI103 ';
DATA FDAT;
INPUT X 1-7 Y 9-20;
CARDS;
++EMBED F=NEI103R GR=NEI;
DATA F2DAT;
INPUT X2 1-7 Y2 9-20;
```

```
CARDS;
++EMBED F=NEI103 GR=NEI;
DATA MATCH;
MERGE FDAT F2DAT;
Y=Y/X;
Y2=Y2/X2;
PROC NLIN METHOD=MARQUARDT EFORMAT
 CONVERGE=1E-9;
PARMS BK=2.638E-04 A=0.0
 D=9.6E-05 B=1.65 C=0.986;
BETA=6.2831825*(X-173.0)/C;
ALFA=B+BETA;
CALFA=1.570796+ALFA;
MODEL Y=A*X+BK+D*SIN(ALFA);
DER.A=X;
DER.BK=1;
DER.B=D*SIN(CALFA);
DER.C=D*SIN(CALFA)*(-BETA/C);
DER.D=SIN(ALFA);
BOUNDS 0.000002< D <0.00025;
BOUNDS 0.94< C <1.1;
BOUNDS -6.28<= B <=6.28;
OUTPUT OUT=DATI1
PREDICTED=YFIT RESIDUAL=RESTO PARMS=BK A D B C;
```

```
DATA DATI2;
MERGE MATCH DATI1;
Y2=(Y2-YFIT);
TITLE H=1.0 F=XSWISS   'B-L CORRECTION R(1) HD-Ne AT
   195 K';
PROC GPLOT DATA=DATI2;
 AXIS1 VALUE=(f=duplex h=1.5)
 LABEL=(F=TRIPLEX H=2 A=0 R=0
 'FREQUENCY IN WAVENUMBERS')
 ORDER=173.0 TO 183.0 BY 2.0
 MAJOR=(H=-2.0) MINOR=NONE;
 AXIS2 VALUE=(f=duplex h=1.5)
 MAJOR=(N=5 H=-2.0) MINOR=NONE
 LABEL=(F=TRIPLEX H=2 A=90 R=0
 'ABSORBANCE/FREQUENCY (cm)');
PLOT
 YFIT*X2=1
 Y2*X2=2
 /HAXIS=AXIS1
 VAXIS=AXIS2 FRAME
 OVERLAY;
SYMBOL1 I=SPLINE V=NONE C=R;
SYMBOL2 I=NONE V=J F=SPECIAL H=2 C=R;
FOOTNOTE1 J=L F=SIMPLEX
```

```
 'SIN BASELINE CORRECTION';
FOOTNOTE2 J=L F=SIMPLEX 'HD-Ne NEI103';
DATA DATII2;
MERGE DATI2;
PROC NLIN METHOD=MARQUARDT EFORMAT
 CONVERGE=1E-9;
PARMS D0=2.0482E-6 FWHM=0.3 MU=177.80
 HALE0=0.0 AK=0.0 BKG=0.0;
D1=(X2-MU);
DE=(0.5*FWHM)**2+D1**2;
MODEL Y2=D0/DE+HALE0*2*D1/DE+AK*X2+BKG;
DER.AK=X2;
DER.BKG=1;
DER.D0=1/DE;
DER.MU=(D0+HALE0*2*D1)*2*D1/DE**2-HALE0*2/DE;
DER.FWHM=-(FWHM)*(D0+HALE0*2*D1)/DE**2;
DER.HALE0=2*D1/DE;
OUTPUT OUT=DATI3
PREDICTED=YOK RESIDUAL=REST
 PARMS=D0 FWHM MU HALE0;
TITLE H=2 F=XSWISS 'R(1) LINE OF HD-Ne AT 195 K';
PROC GPLOT;
 AXIS1 VALUE=(f=duplex h=1.5)
 LABEL=(F=TRIPLEX H=2 A=0 R=0
```

```
 'FREQUENCY IN WAVENUMBERS')
 ORDER=173.0 TO 183.0 BY 2.0
 MAJOR=(H=-2.0) MINOR=NONE;
 AXIS2 VALUE=(f=duplex h=1.5)
 MAJOR=(N=5 H=-2.0) MINOR=NONE
 LABEL=(F=TRIPLEX H=2 A=90 R=0
 'ABSORBANCE/FREQUENCY (cm)');
PLOT
YOK*X2=1
Y2*X2=2
/HAXIS=AXIS1
VAXIS=AXIS2 FRAME
OVERLAY;
SYMBOL1 I=SPLINE V=NONE C=R;
SYMBOL2 I=NONE V=J F=SPECIAL H=2 C=R;
FOOTNOTE1 J=L F=SIMPLEX 'FANO+SIN(A) SFR1';
FOOTNOTE2 J=L F=SIMPLEX 'HD-Ne NEI103';
/*
//
```

Appendix E

FORTRAN Program

This FORTRAN program is used for the calculation of number density of HD-N_2 mixture at 195 K. Input P is pressure in torr and NFIL is the order number of the data file.

```
// EXEC WATFIV,SIZE=240K
//SYSIN DD *
$JOB WATFIV
      DIMENSION P(30),NFIL(30),PMIX(30),GI(30),GII(30),G1(30)
     DIMENSION G2(30),B(30),BI(30),DEN(30),DENI(30),PDEN(30)
    1 T=195.0
      BHD=10.79
      R=82.05
      BPERT=-37.48
      PHD=2715.0/760.0
      BINT=1.20
      DENHD=4.99211
      WRITE (6,400)
```

```
 5  DO 230 N=1,18
    READ,P(N),NFIL(N)
    PMIX(N)=P(N)/760.0
    GI(N)=PHD/PMIX(N)
    GII(N)=(PMIX(N)-PHD)/PMIX(N)
    B(N)=BHD*GI(N)*GI(N)+2.0*BINT*GI(N)*GII(N)+
   +BPERT*GII(N)*GII(N)
    DEN(N)=22414.0/(R*T/PMIX(N)+B(N))
10  DO 50 I=1,14
    G1(N)=DENHD/DEN(N)
    G2(N)=(DEN(N)-DENHD)/DEN(N)
    BI(N)=BHD*G1(N)*G1(N)+2.0*BINT*G1(N)*G2(N)+
   +BPERT*G2(N)*G2(N)
    DENI(N)=22414.0/(R*T/PMIX(N)+BI(N))
    IF (ABS(DENI(N)-DEN(N))-1E-8)60,60,40
40  DEN(N)=DENI(N)
    GOTO 50
50  CONTINUE
60  PDEN(N)=DENI(N)-DENHD
    WRITE (6,70)NFIL(N),P(N)
70  FORMAT (2X,'FILE:',I3,2X,'PRESSURE=',F9.2,' TORR')
150 WRITE (6,200) BI(N),G1(N),G2(N)
200 FORMAT (2X,'BMIX= ',F10.5,2X,'G1= ',F8.5,2X,'G2= ',F8.5)
210 WRITE (6,220) DENI(N)
```

```
 220  FORMAT (2X,'M.DENCITY= ',F10.5,' AMAGAT')
 221  WRITE (6,222) PDEN(N)
 222  FORMAT (2X,'P.DENSITY= ',F10.5,' AMAGAT')
 230  CONTINUE
 400   FORMAT (2X,'******* DENSITY OF HD-N2 AT 195 K
   *******')
 250  STOP
    END
$ENTRY
```

Bibliography

[1] G. C. Tabisz, L. Ulivi, P. Drakopoulos and Z. Lu, Spectral Line Shapes VI, edited by L. Frommhold and J. Keto, American Physical Society, New York, 421 (1990).

[2] W. Meyer, in *Phenoma Induced by Intermolecular Interactions*, edited by G. Birnbaum, Plenum, New York, 29 (1985).

[3] G. Alber and J. Cooper, Phys. Rev., A**33**, 3084 (1986).

[4] G. Birnbaum, Adv. Chem. Phys., **12**, 4870 (1967).

[5] L. Ulivi, Z. Lu and G. C. Tabisz, Phys. Rev., A**40**, 642 (1989).

[6] R. H. Tipping and J. D. Poll, in Molecular Spectroscopy: Modern Research, Vol. III, edited by K. N. Rao, Acadamic Press, New York, 421 (1985).

[7] G. Herzberg, Astrophys. J., **87**, 428 (1938).

[8] J. T. Trauger, F. L. Roesler, N. P. Carleton and W. A. Traub, Astrophys. J. Lett., **184**, L137 (1973).

[9] J. Geiss and H. Reeves, Astron. Astrophys., **18**, 126 (1972).

[10] L. Trafton, Astrophys. J., **222**, 740 (1978).

[11] G. Herzberg, Nature, **163**, 170 (1949).

[12] W. Jr. Macy and W. H. Smith, Astrophys. J., **273**, 222 (1978).

[13] L. Trafton and D. A. Ramsay, Icarus, **56**, 176 (1980).

[14] H. M. James and A. S. Coolidge, Astrophys. J., **87**, 438 (1938).

[15] G. C. Wick, Atti. Re. Acc. Lin., **21**, 708 (1935).

[16] G. Herzberg, Nature, **166**, 563 (1950).

[17] Wu, Ta-You, Can. J. Phys., **30**, 291 (1952).

[18] R. A. Durie and G. Herzberg, Can. J. Phys., **38**, 806 (1960).

[19] S. M. Blinder, J. Chem. Phys., **32**, 105 (1960).

[20] S. M. Blinder, J. Chem. Phys., **32**, 582 (1960).

[21] W. Kolos and L. Wolniewicz, J. Chem. Phys., **43**, 2429 (1965).

[22] M. Trefler and H. P. Gush, Phys. Rev. Lett., **20**, 703 (1968).

[23] G. Karl, Can. J. Phys., **46**, 1973 (1968).

[24] A. R. W. McKellar, Astrophys. J. Lett., **185**, L53 (1973).

[25] A. R. W. McKellar, Can. J. Phys., **51**, 389 (1973).

[26] A. R. W. McKellar, J. Chem. Phys., **52**, 1144 (1974).

[27] A. R. W. McKellar, Can. J. Phys., **61**, 4636 (1974).

[28] J. Bejar and H. P. Gush, Can. J. Phys., **52**, 1669 (1974).

[29] J. D. Poll and G. Karl, Can. J. Phys., **51**, 594 (1973).

[30] R. D. G. Prasad and S. P. Reddy, J. Chem. Phys., **62**, 3582 (1975).

[31] R. D. G. Prasad and S. P. Reddy, J. Chem. Phys., **65**, 83 (1976).

[32] R. D. G. Prasad and S. P. Reddy, J. Chem. Phys., **66**, 707 (1977).

[33] A. R. W. McKellar and T. Oka, Can. J. Phys., **56**, 1315 (1978).

[34] F. W. Dalby and J. Vigue, Phys. Rev. Lett., **43**, 1310 (1979).

[35] W. H. Smith and J. Gelfand, J. Quant. Spectros. Radiat. Transfer, **24**, 15 (1980).

[36] L. Wolniewicz and T. Kowalski, Chem. Phys. Lett., **18**, 55 (1973).

[37] L. Wolniewicz, Can. J. Phys., **53**, 1207 (1975).

[38] L. Wolniewicz, Can. J. Phys., **54**, 572 (1976).

[39] A. L. Ford and J. C. Browne, Phys. Rev., A**16**, 1992 (1977).

[40] D. Bishop and L. Cheung, Chem. Phys. Lett., **55**, 593 (1978).

[41] W. R. Thorson, J. H. Choi and S. K. Kundson, Phys. Rev. A**31**, 22 (1985).

[42] W. R. Thorson, J. H. Choi and S. K. Kundson, Phys. Rev. A**31**, 34 (1985).

[43] J. D. Poll, R. H. Tipping, R. D. G. Prasad and S. P. Reddy, Phys. Rev. Lett., **36**, 248 (1976).

[44] R. H. Tipping, J. D. Poll and A. R. W. McKellar, Can. J. Phys. **56**, 75, (1978).

[45] R. M. Herman, Phys. Rev. Lett., **42**, 1206 (1979).

[46] R. M. Herman, R. H. Tipping and J. D. Poll, Phys. Rev. A**20**, 2006 (1979).

[47] J. B. Nelson and G. C. Tabisz, Phys. Rev. Lett., **48**, 1393 (1982).

[48] J. B. Nelson and G. C. Tabisz, Phys. Rev., A**28**, 2157 (1983).

[49] N. H. Rich and A. R. W. McKellar, Can. J. Phys., **61**, 1648 (1983).

[50] A. R. W. McKellar. J. W. C. Johns, W. Majewski and N. H. Rich, Can. J. Phys., **62**, 1673 (1984).

[51] P. Essenwanger and H. P. Gush, Can. J. Phys., **62**, 1680 (1984).

[52] G. C. Tabisz and J. B. Nelson, Phys. Rev. A**31**, 1160 (1985).

[53] Q. Ma, R. H. Tipping snd J. D. Poll, Phys. Rev. A**38**, 6185 (1988).

[54] P. Drakopoulos and G. C. Tabisz, Phys. Rev., A**36**, 5556 (1987).

[55] P. Drakoloulos and G. C. Tabisz, Phys. Rev., A**36**, 5566 (1987).

[56] A. R. W. McKellar, Can. J. Phys., **64**, 227 (1986).

[57] A. Crane and H. P. Gush, Can. J. Phys., 44, 373 (1966).

[58] M. Trefler, A. M. Cappel and H. P. Gush, Can. J. Phys., **47**, 2115 (1969).

[59] R. H. Tipping and J. D. Poll, Phys. Rev., B**35**, 6699 (1987).

[60] A. R. W. McKellar and M. J. Clouter, Chem. Phys. Lett., **140**, 117 (1987).

[61] S. Y. Lee, S. Lee, J. Gains, R. H. Tipping and J. D. Poll, Phys. Rev. B**37**, 2357 (1988).

[62] J. D. Poll, in *Phenomena Induced by Intermolecular Interactions*, edited by G. Birnbaum, Plenum, New York, 677 (1985).

[63] P. Drakopoulos, Ph.D. Thesis, The University of Manitoba (1987).

[64] B. Gao, G. C. Tabisz, M. Trippenbach and J. Cooper, Phys. Rev. A, to be published (1991).

[65] J. Van Kranendonk, *Solid Hydrogen*, Plenum, New York, 2 (1983).

[66] K. Kolos and L. Woleniewicz, Rev. Modern. Phys., **35**, 473 (1963).

[67] K. Kolos, J. Mol. Struct. **19**, 93 (1973).

[68] A. D. Buckingham, Adv. Chem. Phys., **12**, 107 (1967).

[69] A. Borysow and L. Frommhold and W. Meyer, J. Chem. Phys., **88**, 4855 (1988).

[70] G. C. Maitland, M. Rigby and W. A. Wakeham, in *Intermolecular Forces*, Clarendon, Oxford, 47 (1981).

[71] M. E. Rose, *Elementary Theory of Angular Momentum*, Wiley, New York, 222 (1957).

[72] J. D. Poll and J. Van Kranendonk, Can. J. Phys., **39**, 189 (1961).

[73] J. D. Poll and J. L. Hunt, Can. J. Phys., **54**, 461 (1976).

[74] D. M. Brink and G. R. Satchler, *Angular Momentum*, second edition, Clarendon, Oxford, 34 (1968).

[75] J. Mathews and R. L. Walker, *Mathematical Methods of Physics*, W. A. Benjamin, New York (1964).

[76] W. Meyer and L. Frommhold, Phys. Rev., A**34**, 2771 (1986).

[77] W. Meyer and L. Frommhold, Phys. Rev., A**34**, 2936 (1986).

[78] P. W. Anderson, Phys. Rev. **76**, 647 (1949).

[79] W. R. Hindmarsh, in *Atoms, Molecules and Lasers*, IAEA, Vienna, 133 (1974).

[80] K. Burnett, Phys. Reports, **118**, 339 (1985).

[81] J. P. Looney, Ph.D Thesis, The Pennsylvania State University (1987).

[82] J. C. Lewis and J. Van Kranendonk, Can. J. Phys., **50**, 352 (1972).

[83] R. M. Herman, in *Spectral Line Shapes* IV, edited by J. Exton, Deepak, Hampton, 351 (1987).

[84] M. Baranger, Phys. Rev. **111**, 494 (1958).

[85] G. C. Tabisz, private communication (1991).

[86] User's Manual of Nic-7199 FT-IR System, Nicolet Analytical Instructments (1979).

[87] C. H. Perry, R. Geick and E. F. Young, Appl. Opt. **5**, 1171 (1966).

[88] E. Hecht and A. Zajac, *Optics* (Addison-Wesely Series in Physics), Addison-Wesley, 397 (1974).

[89] K. D. Moller and W. G. Rothschild, *Far-Infrared Spectroscopy*, Wiley-Interscience, J. Wiley & Sons., New York, 134 (1971).

[90] J. Conmes, Rev. Opt. **40**, 45 and 231 (1961).

[91] E. V. Loewenstein, Appl. Opt. **2**, 491 (1963).

[92] M. L. Forman, W. H. Steel and G. A. Vanasse, J. Opt. Soc. Am., **56**, 59 (1966).

[93] NICOS User's Manual, Nicolet Analytical Instruments (1986).

[94] R. K. Horne and G. Birnbam, Infrared Phys., **17**, 173 (1984).

[95] User's Manual, Infrared Laboratories, Inc., (1985).

[96] J. W. Cooley and J. W. Tukey, Math. Comput., **19**, 297 (1965).

[97] J. H. Dymond snd E. B. Smith, *The Virial Coefficients of Pure Gases and Mixtures*, Claredon, Oxford (1980).

[98] P. W. Atkins, in *Physical Chemistry*, Freeman, San Francisco, 771 (1978).

[99] A. K. Kudian and H. L. Welsh, Can J. Phys., **49**, 230 (1971).

[100] G. W. Robinson and J. O. Bery, Chem. J. Phys. **53**, 2068 (1975).

[101] G. Herzberg, *Molecular Spectra and Molecular Structure*, second edition, D. Van Nostrand, 109 (1950).

[102] N. H. Rich, J. W. C. Johns and A. R. W. McKellar, J. Mol. Spectros., **95**, 432 (1982).

[103] A. R. W. McKellar, W. Goetz and D. A. Ramsay, Astrophys. J. **207**, 663 (1976).

[104] J. W. C. Johns, J. Opt. Soc. Am., B**2**, 1340 (1985).

[105] D. Robert and J. Bonamy, J. Phys., **40**, 923 (1979).

[106] J. Bonamy and D. Robert, Internal Report, Lab. de Phys. Mol., Faculte des Science, 25030 Besancon Cedex, France (1979).

[107] J. Bonamy and D. Robert, J. Quant. Spectros. Radiat. Transfer, **31**, 23 (1984).

[108] J. Bonamy L. Bonamy and D.Robert, J. Chem. Phys. **67**, 4441 (1977).

[109] R. M. Herman, J. Chem. Phys. **52**, 2040 (1970).

[110] M. J. Norman, R. O. Watts and U. Buck, J. Chem. Phys., **81**, 3500 (1984).

[111] P. E. S. Wormer and G. Van Dijk, J. Chem. Phys. **70**, 5695 (1979).

[112] F. Mulder, A. Van der Avoird and P. E. S. Wormer, Mol. Phys. **37**, 159 (1979).

[113] J. P. Toennies, W. Welz and G. Wolf, J. Chem. Phys., **71**, 614 (1979).

[114] R. J. Leroy, J. Carley and J. E. Grabenstetter, Faraday Discuss. Chem. Soc. **62**, 169 (1977).

[115] N. Lacome and A. Levy, J. Mol. Spectros., **97**, 139 (1983).

[116] C. J. Taso and B. J. Curnutte, J. Quant. Spectrosc. Radiar. Transfer, **2**, 41 (1962).

[117] J. R. Sweet and W. A. Steele, J. Chem. Phys., **47**, 3022 (1967).

[118] T. B. Macrury, W. Steele and J. B. Berne, J. Chem. Phys., **64**, 1288 (1976).

[119] J. P. Looney and R. H. Herman, J. Quant. Spectros. Radiat. Transfer, **37**, 547 (1987).

[120] M. Oobatake and T. Ooi, Prog. Theor. Phys. **48**, 2132 (1972).

[121] J. O. Hirschfelder, C. F. Curtiss and R. B. Bird, *Molecular Theory of Gases and Liquids*, Wiley, New York (1954).

[122] C. Boulet and D. Robert, Chem. Phys. Lett., **60**, 162 (1978).

[123] J. D. Poll and M. S. Miller, J. Chem. Phys., **54**, 2673 (1971).

[124] P. R. Bunker, J. Mol. Spectros. **46**, 119 (1973).

[125] J. Bonamy, private communication (1991).

[126] J. Schaefer and L. Monchick, J. Chem. Phys. **87**, 171 (1987).

[127] M. J. Clouter and A. R. W. McKellar, Can. J. Phys., **65**, 1 (1987).

[128] L. Trafton, Astrophys. J., **179**, 971 (1973).

[129] J. D. Poll, J. L. Hunt and J. W. Mactaggart, Can. J. Phys., **53**, 954 (1975).